
DEEP LEARNING AND REMOTE SENSING FOR DETECTING TREE MORTALITY PATTERNS

Zur Erlangung des akademischen Grades eines
DOKTORS DER NATURWISSENSCHAFTEN
(Dr. rer. nat.)

von der KIT-Fakultät für
Bauingenieur-, Geo- und Umweltwissenschaften
des Karlsruher Instituts für Technologie (KIT)
genehmigte

DISSERTATION

von
Felix Schiefer
aus Erlangen

Karlsruhe 2024

Tag der mündlichen Prüfung: 25. Juli 2024
Referent: Prof. Dr. Sebastian Schmidlein
Korreferentin: Prof. Dr. Nadine Rühr

ACKNOWLEDGMENTS

In the countless hours of research, coding, writing, and doubt that have led to the completion of this doctoral thesis, I have been supported by numerous people. It is my pleasure to thank everyone who has accompanied me on this journey and made this work possible.

First and foremost, I would like to express my gratitude to Sebastian Schmidlein for providing me with the opportunity to write my doctoral thesis on such an engaging topic and for granting me the freedom to pursue my own path.

I wish to extend my gratitude to the entire doctoral committee for investing their valuable time, to Nadine Rühr for reviewing this thesis and to Stefan Hinz for chairing the committee.

My special thanks go to Teja Kattenborn, who is consistently paving new avenues and without whom this exciting project would not have been possible. His inexhaustible productivity and creativity, as well as his enthusiasm for this exciting topic, have repeatedly motivated me.

I would like to thank my collaborators Annett Frick, Randolph Klinke, Benjamin Stöckigt, Kathrin Wagner, Julian Frey, Katarzyna Zielewska-Büttner, Andreas Uhl, Peter Schall and Samuli Junttila, without whom I would never have created such a solid database, which was so crucial for conducting my studies.

Thanks also to the Graduate School for Climate and Environment GRACE and especially Andreas Schenk for the financial support for scientific conferences and summer schools.

Thank you my great colleagues at the group of vegetation science at the Institute of Geography and Geoecology who have accompanied me during my time as a doctoral student and many of whom have become good friends. Thank you, Jannika Schäfer, Pia Labenski, Johannes Senn, Anne Lewerentz, Michael Ewald, Elham Shafeian, Dikko Jeff Gafna, Christopher Schiller, Tamalika Chakraborty, Fabian Fassnacht, Jesse Kalwij, Yhasmin Mendes de Moura, Florian Hogewind, Reiner Gebhardt, Christophe Neff, Petra Zizmann, Rita Seith.

Finally, I am grateful for the endless support of my family. Thank you to my parents for letting me follow the path that brought me here. Thank you, Carolin, for your love and your support during my doctoral studies. Here's to the exciting time that lies ahead!

ABSTRACT

Vegetation plays a vital role for life on Earth and provides a range of essential ecosystem service. Forests, in particular, are crucial as they cover nearly one-third of the global land surface and play a central role in carbon storage and, hence, climate regulation. Global climate change and the associated shifts in climatic conditions, the increase in weather extremes (such as drought, heat, frost, and heavy precipitation), as well as the spread of pests and diseases, pose significant challenges to forests. Consequently, increased tree mortality has been observed globally in recent years. To better understand the underlying causes of tree mortality, the phenomenon must first be recorded in its nature and extent. Remote sensing has proven to be a suitable method for characterizing vegetation on large scales, and the amount of remote sensing data is steadily increasing. Specifically, the research satellites of ESA's Sentinel fleet offer a high temporal resolution to best capture the dynamics of vegetation. The spatial resolution of these satellite data (10 m) is above the size of individual trees, which, among other factors (e.g., geopositioning, geometry, timing, viewing perspective), hampers the link with ground reference data. The resulting lack of reference data is the main limitation for satellite-based remote sensing methods in detecting deadwood, and our understanding of the processes leading to tree mortality is therefore incomplete.

Uncrewed aerial vehicles (UAV) can bridge the gap between ground reference data and satellite data, as they provide high-resolution imagery suitable for detecting individual trees. Given the large quantity and diversity of remote sensing data, as well as the high spatial (UAV-data) and temporal (satellite image time series) resolutions, traditional remote sensing methods reach their limits, necessitating adapted methods. Deep learning techniques have already proven to be suitable in other disciplines, such as convolutional neural networks (CNN) for the interpretation of image data (e.g., classification, object detection) or long short-term memory (LSTM) models for processing sequential information (e.g., speech recognition).

This thesis aims to investigate the prerequisites and suitability of deep learning methods for remote sensing of deadwood—and vegetation in general. Central to this is the *upscaling* approach: first, standing deadwood is automatically segmented from UAV-based orthomosaics using CNNs. The identified deadwood then serves as reference data for LSTMs, which are based on satellite image time series (i.e., Sentinel-1 and Sentinel-2) and enable the large-scale detection of standing

deadwood at the landscape level. In three studies, with a geographical focus on mixed forests in Germany, the following research questions are addressed: **(1)** to which extent is deep learning suitable for the analysis of very high-resolution, UAV-based remote sensing data? **(2)** in what way is the concerted use of UAVs and deep learning capable to close the reference data gap on tree mortality? **(3)** to what extent is deep learning suitable for extracting temporal information from satellite image time series? and **(4)** what are the spatio-temporal patterns and environmental drivers of tree mortality in Germany?

The first study explores the potential of CNNs for the analysis of UAV-based, high-resolution (<2 cm), RGB orthomosaics. For this purpose, twelve tree species, standing deadwood, and forest floor were mapped in 51 study plots, each 1 ha in mixed forest stands. Using a U-net CNN-architecture, the influence of tile sizes, spatial resolution, and additional tree height information was tested. The accuracy of the CNN achieved an F1-score of 0.73. Smaller tile sizes accounted for underrepresented species in the dataset but increased inference time and resulted in edge effects. Tree height information barely improved the models, while a high spatial resolution was decisive for the identification of tree species.

The second study focuses on upscaling deadwood from the local level to the landscape level. Therefore, standing deadwood in 176 UAV-scenes from 2017–2021, covering 727 ha of forest, was automatically classified and segmented using a U-net. The resulting polygons were used as reference data for LSTMs, which predicted the proportion of standing deadwood per pixel across Germany from Sentinel time series. The CNN-based segmentation of standing deadwood was highly accurate (F1-score = 0.82, median of all study sites). The LSTMs achieved the best results when using all available bands from Sentinel-1 and Sentinel-2 and two vegetation indices (i.e., kNDVI, NDWI) (Pearson's correlation coefficient = 0.66). Validation with orthophotos revealed a spatially and temporally accurate detection of standing deadwood.

In the third study, the nationwide maps of standing deadwood are analysed to investigate the spatio-temporal patterns of tree mortality and its causes. From 2018–2021, a total of 978 ± 529 (kilohectares) kha of forest died, which is about double the amount of deadwood recorded in the forest condition survey and other remote sensing studies. The Harz region (47.2 kha, 30.2% of forested area) and Sueder Uplands (74.2 kha, 17.1%) were the most affected, with *Picea abies* and *Pinus sylvestris* being the most impacted species. Using random forest regression and a model-agnostic interpretation method (*accumulated local effects*, ALE), the key environmental drivers and their effects were identified and analysed. Atmospheric conditions (i.e., late frosts, climatic water balance, hot days, and vapour pressure deficit) were the most important predictors of tree mortality. Smaller and younger stands showed increased tree mortality at the landscape level, contrasting results from local studies. Monocultures were generally less affected by mortality unless pest insects were present.

The present thesis demonstrates that deep learning plays a key role in analysing the diverse and large amounts of remote sensing data (*big data*), as it can ideally evaluate spatial and temporal information without special preprocessing of input data. The flexible design of deep learning architectures allows for integrated analysis of different dimensions (i.e., spatial, temporal, spectral) and types (i.e., optical, radar, lidar) of remote sensing data. Deep learning enables detailed remote sensing detection of standing deadwood at the landscape level, thereby improving our understanding of the patterns and processes leading to tree mortality. The concerted use of UAVs and CNNs can bridge the reference data gap for satellite-based methods at the landscape level. Due to the data-intensive nature of deep learning, a collaborative effort by the scientific community is required to share and compile research data to address the challenges of climate change on vegetation globally.

KURZFASSUNG

Vegetation spielt eine wichtige Rolle für Leben auf der Erde und bietet eine Vielzahl an Ökosystemdienstleistungen. Dabei ist insbesondere Wald wichtig, da dieser knapp ein Drittel der globalen Landoberfläche bedeckt und eine zentrale Rolle bei der Speicherung von Kohlenstoff und damit bei der Regulierung des Klimas hat. Der globale Klimawandel und die damit verbundene Verschiebung der klimatischen Standortbedingungen, die Zunahme von Wetterextremen (wie Dürre, Hitze, Spätfrost und Starkniederschlag), sowie die dadurch begünstigte Ausbreitung von Schädlingen und Krankheiten stellen den Wald vor große Herausforderungen. In der Konsequenz konnte Baumsterblichkeit in den vergangenen Jahren auf globaler Ebene vermehrt beobachtet werden. Um die zugrundeliegenden Ursachen des Baumsterbens besser zu verstehen, muss das Phänomen zunächst in seiner Art und Ausbreitung erfasst werden. Dabei hat sich die Fernerkundung als geeignetes Mittel erwiesen, großflächig Vegetation zu charakterisieren, und die Menge an Fernerkundungsdaten nimmt stetig zu. Insbesondere die Forschungssatelliten von ESA's Sentinel Flotte bieten eine hohe zeitliche Auflösung, um die Dynamik der Vegetationsveränderung abzubilden. Die räumliche Auflösung dieser Satellitendaten (10 m) liegt oberhalb der Auflösungsgrenze von Einzelbäumen, was, neben weiteren Faktoren (z.B., Geopositionierung, Geometrie, Aufnahmezeitpunkt, Datenmenge, Perspektive), die Verknüpfung mit Bodenreferenzdaten erschwert. Der resultierende Mangel an Referenzdaten ist die Hauptlimitierung für satellitenbasierte Fernerkundungsmethoden bei der Erfassung von Totholz und unser Verständnis der Prozesse, die zu Baumsterben führen, ist dadurch unvollständig.

Die Brücke von Bodenreferenzdaten zu Satellitendaten können Drohnen (*uncrewed aerial vehicle*, UAV) schlagen, da sie räumlich hochaufgelöste Bilddaten liefern, die gut zur Erkennung von Einzelbäumen geeignet sind. Bei der großen Menge und Vielfalt an Fernerkundungsdaten sowie den hohen räumlichen (Drohnendaten) und zeitlichen (Satellitendatenzeitreihen) Auflösungen, stoßen traditionelle Fernerkundungsmethoden an ihre Grenzen, und es bedarf angepasster Methoden. Deep Learning Verfahren haben sich dabei in anderen Fachdisziplinen bereits als geeignet herausgestellt, etwa *convolutional neural networks* (CNN) bei der Interpretation von Bilddaten (z. B. Klassifikation, Objekterkennung) oder *long short-term memory* (LSTM) Modelle für die Verarbeitung sequenzieller Informationen (z. B. Spracherkennung).

Ziel der vorliegenden Arbeit ist es, die Voraussetzung und Eignung von Deep Learning Methoden bei der fernerkundlichen Erfassung von Totholz und von Vegetation im Allgemeinen wissenschaftlich zu untersuchen. Von zentraler Bedeutung ist dabei der *Upscaling*-Ansatz. Dazu wird zunächst stehendes Totholz aus drohnenbasierten Orthomosaiken mithilfe von CNNs automatisiert klassifiziert und segmentiert. Das erkannte Totholz dient anschließend als Referenzdaten für LSTMs, die auf Satellitendatenzeitreihen (Sentinel-1 und Sentinel-2) basieren, und die großflächige Erfassung von stehendem Totholz auf Landschaftsebene ermöglichen. In drei Teilstudien, mit geographischem Fokus auf Mischwäldern in Deutschland, wird untersucht: (1) inwiefern Deep Learning Methoden zur Auswertung sehr hochaufgelöster, drohnenbasierter Fernerkundungsdaten geeignet sind; (2) inwiefern Drohnen und Deep Learning die Referenzdatenlücke zur Baumsterblichkeit schließen können; (3) inwiefern Deep Learning Methoden geeignet sind, Informationen aus Satellitendatenzeitreihen zu extrahieren; und (4) was die räumlich-zeitlichen Muster von Baumsterben in Deutschland und dessen Ursachen sind.

In der ersten Studie wird das Potenzial von CNNs zur Auswertung von drohnenbasierten, hochaufgelösten (<2 cm), RGB-Orthomosaiken erörtert. Dazu werden zwölf Baumarten, stehendes Totholz und Waldboden in 51 Untersuchungsflächen á 1 ha in gemischten Waldbeständen kartiert. Mit einer U-net CNN-Architektur wird der Einfluss der Kachelgrößen, der räumlichen Auflösung und von zusätzlicher Baumhöheninformation getestet. Die Genauigkeit der CNNs lag bei $F1\text{-score} = 0,73$. Eine kleinere Kachelgröße berücksichtigt im Datensatz unterrepräsentierte Arten, erhöht jedoch die Inferenzzeit und produziert Randeffekte. Baumhöheninformation verbesserte die Modelle kaum, während eine hohe räumliche Auflösung essenziell war zur Erkennung von Baumarten.

Der Fokus in der zweiten Studie liegt auf dem Upscaling von Totholz von der lokalen Ebene auf die Landschaftsebene. Dazu wird stehendes Totholz in 176 Drohnenszenen aus den Jahren 2017–2021 über 727 ha Wald automatisiert mittels CNN segmentiert. Die resultierenden Polygone gehen als Referenzdaten in LSTMs ein, die aus Sentinel Zeitreihen den Anteil an stehendem Totholz je Pixel für ganz Deutschland schätzen. Die CNN-basierte Segmentierung von stehendem Totholz war sehr genau ($F1\text{-score} = 0,82$, Median aller Flächen). Bei den LSTMs führten alle verfügbaren Kanäle von Sentinel-1 und Sentinel-2 und zwei Vegetationsindizes (kNDVI, NDWI) zu den besten Modellen (Pearson's Korrelationskoeffizient = 0,66). Eine Validierung mit Orthophotos offenbarte eine räumlich und zeitlich akkurate Erfassung von stehendem Totholz.

Die deutschlandweiten Karten an stehendem Totholz werden in der dritten Studie analysiert, um räumlich-zeitliche Muster von Baumsterblichkeit und dessen Ursachen zu erforschen. Über die Jahre 2018–2021 starben insgesamt 978 ± 529 kha an Wald, was etwa dem Doppelten des erfassten Totholz in der Waldzustandserhebung und anderen Fernerkundungsstudien entspricht. Bei den Regionen

waren Harz (47,2 kha, 30,2% der bewaldeten Fläche) und Sauerland (74,2 kha, 17,1%) am stärksten betroffen, bei den Arten *Picea abies* und *Pinus sylvestris*. Mit einer random forest Regression und einer modellagnostischen Interpretationsmethode (*accumulated local effects*, ALE) werden die wichtigsten Umweltfaktoren sowie deren Auswirkungen identifiziert. Atmosphärischen Bedingungen (d. h., Spätfröste, klimatischer Wasserhaushalt, heiße Tage und Dampfdruckdefizit) waren die wichtigsten Prädiktoren für die Baumsterblichkeit. Kleinere und jüngere Bestände wiesen auf Landschaftsebene eine erhöhte Baumsterblichkeit auf, was die Ergebnisse von lokalen Studien kontrastiert. Monokulturen waren generell weniger von Mortalität betroffen, es sei denn, Schadinsekten waren vorhanden.

In der vorliegenden Arbeit zeigte sich, dass bei der Auswertung der vielfältigen und großen Mengen (*big data*) an Fernerkundungsdaten Deep Learning eine Schlüsselrolle zukommt, da es, ohne spezielle Vorprozessierung der Eingangsdaten, die räumliche und zeitliche Information ideal auswerten kann. Durch die flexible Gestaltung der Deep Learning Architekturen können die verschiedenen Dimensionen (räumlich, zeitlich, spektral) und Typen (optisch, radar, lidar) von Fernerkundungsdaten integriert analysiert werden. Deep Learning ermöglicht die detaillierte fernerkundliche Erfassung von Totholz auf Landschaftsebene und verbessert dadurch unser Verständnis der Muster und Prozesse von Baumsterblichkeit. Ein konzertierter Einsatz von Drohnen und CNNs ist in der Lage, die Referenzdatenlücke für satellitendatenbasierte Methoden auf Landschaftsebene zu schließen. Aufgrund des Datenhungers von Deep Learning, bedarf es einer gemeinschaftlichen Anstrengung der wissenschaftlichen Gemeinschaft Forschungsdaten zu teilen und zusammenzutragen, um die Herausforderungen des Klimawandels für die Vegetation auch auf globaler Ebene zu adressieren.

CONTENTS

ABSTRACT	v
KURZFASSUNG	ix
LIST OF PUBLICATIONS	xvii
LIST OF FIGURES	xix
LIST OF TABLES	xxi
ACRONYMS AND ABBREVIATIONS	xxiii
1 INTRODUCTION	1
1.1 Main motivation	2
1.2 Increasing tree mortality	3
1.3 Remote sensing of vegetation	4
1.3.1 Fundamentals of remote sensing of vegetation	4
1.3.2 Reference data requirements	6
1.3.3 UAV as intermediary: linking ground and satellite data ..	7
1.3.4 Remote sensing in the era of big data	7
1.4 Deep learning	8
1.4.1 Fundamentals of deep learning	9
1.4.2 Deep learning in remote sensing of vegetation	11
1.5 Research needs	12
2 MAPPING FOREST TREE SPECIES IN HIGH RESOLUTION UAV-BASED RGB-IMAGERY BY MEANS OF CONVOLUTIONAL NEURAL NETWORKS ..	17
2.1 Introduction	19
2.2 Material and Methods	20
2.2.1 Study area	20
2.2.2 Data acquisition	22
2.2.3 Reference data extraction	23

2.2.4	Data splitting	23
2.2.5	CNN-based tree species mapping	24
2.2.6	Accuracy assessment	25
2.3	Results	26
2.3.1	Model training	26
2.3.2	Model results	27
2.3.3	Prediction on independent scene	29
2.4	Discussion	29
2.4.1	Model performance	29
2.4.2	Tile size	31
2.4.3	Canopy height information	31
2.4.4	Spatial resolution	32
2.4.5	Model generalization	32
2.4.6	CNN architecture	34
2.4.7	Reference data	35
2.5	Conclusion	37
3	UAV-BASED REFERENCE DATA FOR THE PREDICTION OF FRACTIONAL COVER OF STANDING DEADWOOD FROM SENTINEL TIME SERIES	39
3.1	Introduction	41
3.2	Material and Methods	43
3.2.1	Study area and UAV data acquisition	43
3.2.2	CNN-based segmentation of standing deadwood at local level	44
3.2.3	Mapping deadwood cover fractions at landscape level using satellite time series	47
3.3	Results	50
3.3.1	CNN-based deadwood segmentation in UAV-orthomosaics (local level)	50
3.3.2	Mapping fractional cover of standing deadwood from Sentinel time series using LSTM (landscape level)	51
3.4	Discussion	55
3.4.1	UAV- and CNN-based deadwood segmentation as a reference data source	55
3.4.2	LSTM-based modelling of standing deadwood from satellite time series	57
3.5	Conclusion	61

4	LARGE-SCALE REMOTE SENSING REVEALS THAT TREE MORTALITY IN GERMANY APPEARS TO BE GREATER THAN PREVIOUSLY EXPECTED	63
4.1	Introduction	65
4.2	Material and methods	68
4.2.1	Tree mortality in Germany	68
4.2.2	Identifying drivers of tree mortality using random forest	69
4.3	Results	71
4.4	Discussion	77
4.4.1	Pattern of tree mortality in Germany	77
4.4.2	Atmospheric conditions as main driver of tree mortality	79
4.4.3	Mixed effect of forest composition and structure	80
4.5	Conclusion	83
5	SYNTHESIS	85
5.1	Advancing vegetation remote sensing with deep learning algorithms	86
5.1.1	Spatial pattern extraction using convolutional neural networks	86
5.1.2	Harnessing the temporal dimension with long short-term memory networks	88
5.2	Leveraging deep learning for comprehensive landscape-level analyses	89
5.2.1	Integrating multidimensional remote sensing data	90
5.2.2	Closing the reference data gap on tree mortality	91
5.3	Enhanced understanding of tree mortality by landscape-level analyses	92
5.4	Outlook	94
	APPENDIX	97
	REFERENCES	115

LIST OF PUBLICATIONS

PARTS OF THIS THESIS HAVE ALREADY BEEN PUBLISHED, SUBMITTED, OR PRESENTED . . .

. . . in scientific journals:

- Schiefer, F., Kattenborn, T., Frick, A., Frey, J., Schall, P., Koch, B., & Schmidtlein, S. (2020). Mapping forest tree species in high resolution UAV-based RGB-imagery by means of convolutional neural networks. *ISPRS Journal of Photogrammetry and Remote Sensing*, 170, 205–215. <https://doi.org/10/ghrrhs>
- Schiefer, F., Schmidtlein, S., Frick, A., Frey, J., Klinke, R., Zielewska-Büttner, K., Junttila, S., Uhl, A., & Kattenborn, T. (2023a). UAV-based reference data for the prediction of fractional cover of standing deadwood from Sentinel time series. *ISPRS Open Journal of Photogrammetry and Remote Sensing*, 8, 100034. <https://doi.org/10.1016/j.ophoto.2023.100034>
- Schiefer, F., Schmidtlein, S., Hartmann, H., Schnabel, F., & Kattenborn, T. (n.d.). Large-scale remote sensing reveals that tree mortality in Germany appears to be greater than previously expected. (*under review*) *Forestry: An International Journal of Forest Research*

. . . as data sets:

- Schiefer, F., Frey, J., & Kattenborn, T. (2022a). FORTRESS. <https://doi.org/https://doi.org/10.35097/538>
- Schiefer, F., Schmidtlein, S., Frick, A., Frey, J., Klinke, R., Zielewska-Büttner, K., Uhl, A., Junttila, S., & Kattenborn, T. (2023b). Data package v2: UAV-based reference data for the prediction of fractional cover of standing deadwood from Sentinel time series. <https://doi.org/10.5445/IR/1000158765>
- Schiefer, F., & Kattenborn, T. (2024). FORTRESSdead. <https://doi.org/10.35097/yARnkDzIcZIPSQhI>

. . . at scientific conferences (only own contributions):

- Schiefer, F., Kattenborn, T., Frick, A., Frey, J., Schall, P., Koch, B., & Schmidtlein, S. (2021). Mapping forest tree species in high resolution UAV-based

RGB-imagery by means of convolutional neural networks. *European Geosciences Union General Assembly (EGU 2021)*, Online, 19.04.2021 – 30.04.2021. <https://doi.org/10.5445/IR/1000167640>

- Schiefer, F., Frick, A., Frey, J., Koch, B., Zielewska-Büttner, K., Juntila, S., Schmidlein, S., & Kattenborn, T. (2022b). Predicting fractional cover of standing deadwood at landscape level based on long short-term memory networks and Sentinel time series. *Living Planet Symposium (2022)*, Bonn, Germany, 23.05.2022 – 27.05.2022. <https://doi.org/10.5445/IR/1000167639>

ADDITIONAL RELATED WORK HAS ALREADY BEEN PUBLISHED . . .

. . . in scientific journals:

- Kattenborn, T., Leitloff, J., Schiefer, F., & Hinz, S. (2021). Review on Convolutional Neural Networks (CNN) in vegetation remote sensing. *ISPRS Journal of Photogrammetry and Remote Sensing*, 173, 24–49. <https://doi.org/10/ghtrws>
- Kattenborn, T., Schiefer, F., Frey, J., Feilhauer, H., Mahecha, M. D., & Dormann, C. F. (2022). Spatially autocorrelated training and validation samples inflate performance assessment of convolutional neural networks. *ISPRS Open Journal of Photogrammetry and Remote Sensing*, 5, 100018. <https://doi.org/10.1016/j.ophoto.2022.100018>

LIST OF FIGURES

1.1	Overview of the upscaling approach presented in this thesis. . . .	14
2.1	Map of the two study areas, Southern Black Forest and Hainich NP in Germany.	21
2.2	Detailed overview of the occurring tree species and classes.	24
2.3	Adapted U-net CNN-architecture for the tree species segmentation (Ronneberger et al., 2015)	26
2.4	Validation loss during CNN model training	27
2.5	Predictions of a trained CNN on a 100 × 100 m plot	30
2.6	Selection of synthetic filter visualizations resembling patterns that would most stimulate the CNN	33
3.1	Schematic workflow of the upscaling approach	44
3.2	The six study regions: (1) Southern Black Forest, (2) Black Forest, (3) Dresden Heath, (4) Karlsruhe-Bretten, (5) Hainich National Park, and (6) Helsinki.	46
3.3	Structure of an LSTM unit	49
3.4	Illustration of the CNN model performance for the semantic segmentation of standing deadwood and distribution of F1-scores across study sites	50
3.5	Pearson’s r and total least squares regression slope of the LSTM models for different inputs of Sentinel-1 and Sentinel-2 band sets after cross-validation	52
3.6	Scatterplot of observed and LSTM-predicted fractional cover values of standing deadwood at landscape level	53
3.7	Sentinel-based LSTM-prediction map of fractional standing deadwood cover for the year 2020 in Saxon Switzerland National Park, Germany	54
3.8	Sentinel-2 colour infrared image and LSTM prediction maps of standing deadwood cover in an example region in Saxon Switzerland National Park for the years 2018–2021	55
4.1	Schematic overview of the presented upscaling approach in Schiefer et al. (2023a) extrapolating local observations of standing deadwood in UAV-imagery landscape-level predictions based on satellite image time series.	67

4.2	Correlation plot for the selected 21 environmental predictor variables and standing deadwood.	70
4.3	Temporal development of new standing deadwood from 2018 to 2021 for main tree species (<i>Abies</i> , <i>Fagus</i> , <i>Larix</i> , <i>Picea</i> , <i>Pinus</i> , <i>Pseudotsuga</i> , and <i>Quercus</i>) in Germany.	72
4.4	Accumulated standing deadwood from 2018–2021 for the major natural regions in Germany.	73
4.5	Variable permutation importance of the random forest models. . .	74
4.6	Accumulated local effect (ALE) plots for the 21 environmental predictor variables in descending order based on variable permutation importance.	76
A1	Scatterplot of observed and Random Forest-predicted fractional cover values of standing deadwood at landscape level	101
A2	Correlation plot for all environmental predictor variables and standing deadwood.	108

LIST OF TABLES

2.1	Tree species mapping model accuracies. Classes are sorted descending by their area-related share. For each class, the highest class-specific F1 score is highlighted in bold.	28
3.1	Summary of the regions, sites, and the corresponding UAV acquisitions.	45
4.1	Environmental predictor variables	69
A1	CNN model results using three different cost functions: (1) categorical cross-entropy (CCE), (2) weighted CCE with inversely proportional weights according to the area-related share of the species, and (3) squared weighted CCE with squared inversely proportional weights. All results are based on a CNN with 128×128 pixel RGB + nDSM input tiles at 2 cm spatial resolution.	97
A2	Site-specific F1-Scores for the study regions Southern Black Forest (SBF), Northern Black Forest (NBF), Dresden Heath (DDH), Karlsruhe-Bretten (KAB), Hainich National Park (HAI), and Helsinki (FIN)	98
A3	Summary statistics for the sites from the six study regions Southern Black Forest (SBF), Northern Black Forest (NBF), Dresden Heath (DDH), Karlsruhe-Bretten (KAB), Hainich National Park (HAI), and Helsinki (FIN)	102
A4	Environmental predictor variables.	107
A5	Standing deadwood for the seven dominant tree species in Germany over the years 2018–2021	109
A6	Accumulated standing deadwood during 2018–2021 for the major natural regions of Germany	111

ACRONYMS AND ABBREVIATIONS

ALE	Accumulated local effects
CARD	Copernicus analysis ready data
CARD-BS	Copernicus analysis ready data–terrain-corrected backscatter
CARD-COH6	Copernicus analysis ready data–interferometric coherence
CNN	Convolutional neural network
ConvLSTM	Convolutional long short-term memory network
DBH	Diameter at breast height
DIAS	Copernicus data and information access services
ESA	European Space Agency
GNSS	Global navigation satellite system
GRD	Ground range detected
GSD	Ground sampling distance
IW	Interferometric wide swath
kNDVI	Kernel normalized difference vegetation index
lidar	Light detection and ranging
LSTM	Long short-term memory network
MODIS	Moderate-resolution Imaging Spectroradiometer
NASA	National Aeronautics and Space Administration
nDSM	Normalized digital surface model
NDVI	Normalized difference vegetation index
NDWI	Normalized difference water index
NIR	Near infrared
NP	National park
OA	Overall accuracy
radar	Radio detection and ranging
ReLU	Rectifier linear unit
RGB	Red Green Blue

RNN	Recurrent neural network
RTM	Radiative transfer model
RTK	Real-time kinematic
SAR	Synthetic-aperture radar
SfM	Structure from motion
SIFT	Scale-invariant feature transform
SITS	Satellite image time series
SLC	Single-look complex
SWIR	Short wave infrared
TLS	Total least squares regression
UAV	Uncrewed aerial vehicle
VNIR	Visible near infrared

Chapter 1

1 INTRODUCTION

1.1 MAIN MOTIVATION

Vegetation plays a vital role for life on Earth. Forests, in particular, are crucial as they cover nearly one-third of the global land surface (FAO, 2020). Forests provide a range of essential ecosystem services: they provide habitats, food, medicine, and other raw materials. They regulate our climate through carbon sequestration, purify water and air, produce oxygen, and foster soil formation and protect it from erosion. Forests are also of great economic importance, and hold cultural, spiritual, and aesthetic value (FAO & UNEP, 2020). Global climate change poses a major threat to forest ecosystems, but the total impact is not yet foreseeable. It is therefore of great importance to monitor forests to assess the impacts and risks of global climate change. Remote sensing has proven to be a valuable tool to monitor the distribution and condition of forests (Fassnacht et al., 2023). In particular, satellite-based remote sensing provides the necessary spatial and temporal coverage to detect vegetation and its change on a global scale. However, the amount of data generated is correspondingly large, and is also supplemented by data from sensors mounted on aircraft and uncrewed aerial vehicles (UAV). Traditional remote sensing methods often reach their limits when it comes to interpreting and evaluating large and complex data sets. Deep learning has proven to be promising in other disciplines and offers efficient, automated and accurate methods, but its application in remote sensing is still underexposed. This dissertation, therefore, aims to discuss the advantages and disadvantages of existing deep learning methods in remote sensing of vegetation, to develop new approaches and to expand their practical applicability.

The following section (1.2) describes open questions regarding the patterns and drivers of tree mortality, as well as the current challenges in capturing and understanding these at landscape level. The subsequent section (1.3) provides the scientific-technical background of remote sensing of forests and vegetation in general, with a focus on reference data requirements, the key role of UAVs in linking field observations with satellite data, and the challenges in handling big data. Section 1.4 gives an overview of deep learning methods and their application in remote sensing. The research gaps identified are explained in section 1.5 and the research questions are formulated. The results of the original research are described in chapters 2, 3, and 4, and the three studies have already been published or currently have been submitted to international peer-reviewed journals. The results of the individual studies are comprehensively discussed in the final chapter (5). Moreover, the advantages and disadvantages of deep learning methods in remote sensing are examined, the concerted use of UAVs and deep learning to address the reference data gap in tree mortality is discussed, and perspectives are provided on what is necessary for the successful integration of deep learning in remote sensing.

1.2 INCREASING TREE MORTALITY

Climate change poses a major threat to forests, due to an associated rise in temperatures, the occurrence of episodic precipitation and droughts, or increased rising atmospheric vapour pressure deficit (Hartmann et al., 2022; McDowell et al., 2022; Schuldt et al., 2020). Under such conditions, trees get stressed and may eventually die due to carbon starvation, hydraulic failure, or ensuing pest infestations. Global change has also led to the emergence of 'hotter droughts' during which high temperatures coincide with low precipitation (Allen et al., 2015; Hammond et al., 2022), and consecutive (hotter) droughts have also become more frequent (Hari et al., 2020; Rakovec et al., 2022). In a climate increasingly characterized by extremes, stress factors can also manifest collectively as compound events, amplifying the effects of individual stressors (Zscheischler et al., 2018, 2020). Consequently, increased tree mortality has been observed extensively (Allen et al., 2010; Byer & Jin, 2017; Rakovec et al., 2022; Senf et al., 2018). Even if trees do not die during the initial year of drought, critical ecosystem changes and mortality may still occur in subsequent years, a phenomenon known as drought legacy or lag effects (Obladen et al., 2021; Pohl et al., 2023; Schnabel et al., 2022).

The mechanisms leading to tree dieback may be well understood at the local level, but they are not necessarily applicable to the landscape level (Clark et al., 2016), and our understanding of the regional effects of tree mortality is inconclusive. As comprehensive large-scale datasets on tree mortality are lacking, many of our findings stem from compiled and harmonized datasets of *in situ* observations of dieback events (Allen et al., 2010; Hammond et al., 2022). Due to a lack of standardised survey methods, often only damaged areas of a certain minimum size are included, which poses two problems for investigating the extent and the underlying causes: standing deadwood often accumulates over extended periods and the temporal link between the environmental cause and the dieback event may be weakened or already obscured by other factors. Tree mortality often occurs gradual and scattered across the landscape, and is likely to be underrepresented in the aforementioned data sets (Cheng et al., 2024; Milodowski et al., 2017).

The national forest condition survey (Waldzustandserhebung, WZE) has been assessing tree vitality since 1984 (1990 for the new federal states) and has recorded increased tree mortality in recent years following consecutive drought years in Germany. The annual survey is based on a total of 402 systematically distributed investigation plots across Germany and reports tree mortality based on approximately 10 000 randomly sampled trees (BMEL 2023). Since full forest inventories are unrealistic, remote sensing methods are better suited for comprehensive large-scale analyses. Although remote sensing has been demonstrated to capture large-scale patterns of tree mortality (e.g., Brodrick & Asner, 2017; Byer & Jin,

2017; Garrity et al., 2013; Hansen et al., 2013; Schwantes et al., 2016), the scattered nature of tree dieback impedes the detectability, when the spatial resolution of the employed sensors is coarser than the targeted trees. As reference data is scarce, tree mortality is often not mapped directly. Instead, vegetation indices are used as a proxy of dieback, but the reasons for changes in vegetation indices are plenty and may not necessarily indicate mortality but rather vitality decline.

1.3 REMOTE SENSING OF VEGETATION

1.3.1 FUNDAMENTALS OF REMOTE SENSING OF VEGETATION

“Remote sensing has been variously defined but basically it is the art or science of telling something about an object without touching it.” (Fischer et al., 1976, p.34) To put it more technically, remote sensing describes the process of obtaining information about the Earth’s surface from a distance by measuring the reflected or emitted electromagnetic radiation (Lillesand et al., 2015). Remote sensing of vegetation is a specialized field that focuses on collecting information about the characteristics of vegetation and changes thereof. The electromagnetic spectrum that is typically measured in remote sensing of vegetation ranges from the visible light (400–700 nm) through the infrared range (700 nm–1 mm) to microwaves (1 mm–1 m) (Jones & Vaughan, 2010). Depending on the system and application, different properties of the electromagnetic wave are measured. Passive remote sensing methods record the naturally occurring radiation, namely reflected solar radiation or emitted thermal radiation. Active remote sensing systems, on the other hand, emit energy and capture the radiation reflected from the Earth’s surface.

Remote sensing data can be characterized by their spatial, temporal, spectral, and radiometric resolution. Spatial resolution describes the smallest possible distance between two adjacent points where they can still be distinguished from each other. Temporal resolution is the time interval between two acquisitions of the same area. Spectral resolution refers to the wavelength ranges—so-called bands—that a sensor can separate. The larger the number of bands and the narrower the wavelength ranges they cover, the higher the spectral resolution. There is a trade-off between spatial and spectral resolution due to limitations of the incident energy at the sensor. The higher the spatial or spectral dimensions are resolved, the less energy of the incident radiation is available in the resolution cells of the sensor. When increasing the resolution for one dimension, the other dimension is automatically limited in its maximum resolution. Another important trade-off concerns the spatial resolution and the area covered by the sensor, i.e., sensor footprint. The number of resolution cells of the sensor is technically limited. The maximum achievable spatial resolution is therefore inversely dependent on

the field of view of the sensor, and a higher spatial resolution comes with a smaller sensor footprint. Radiometric resolution describes the ability of a sensor to measure and store differences in the amount of incident energy. Except for laser-based remote sensing, the recorded data is typically stored and distributed as a raster image with a defined pixel size.

In remote sensing of vegetation, the observed signal results from a complex interaction between radiation incident on the surface and the biochemical and structural properties of the vegetation (Jones & Vaughan, 2010). The absorption of incident wavelengths is mainly controlled by the content of various biochemical components such as water, pigments (e.g., chlorophyll, carotenoid), and leaf dry matter. The scattering of incident and transmitted radiation is controlled by structural properties such as shape, size, arrangement, and orientation of leaves within the canopy, as well as the density of the vegetation (Asner, 1998; Ollinger, 2011). Remote sensing applications have used these unique reflectance properties, that are specific to objects and materials, to effectively characterize vegetation by employing suitable sensors. Typically, optical sensors are utilized to derive biochemical properties, whereas active sensors such as radio detection and ranging (radar) and light detection and ranging (lidar) are used to derive biophysical properties or ecosystem structure (Fassnacht et al., 2016).

Another important factor in remote observation of vegetation is the phenological cycle. During a year, plants undergo seasonal changes in the biophysical and -chemical characteristics which are valuable to deriving information about vegetation health, productivity, or temporal dynamics in general.

There are two basic modelling approaches for harnessing remote sensing data in vegetation science: empirical models and radiative transfer models (RTM). A further model type are so-called semi-empirical or hybrid models as a combination of the former two. Empirical models are based on statistical relationships between the remote sensing signal and ground-based reference measurements or observations. RTMs are physical-based models that attempt to directly model the radiative transfer process of light inside plants. The inversion of these models allows deriving the biochemical and physical properties from the remote sensing signal. Independent of the model type, ground reference data are needed, either for model training, model accuracy assessment, or instrument calibration. Large amounts of reference data are required to build robust models, depending on the research subject and question (see section 1.3.2).

The Sentinel-1 and Sentinel-2 satellite missions of ESA's Copernicus program, or the Landsat satellites by NASA, are of paramount importance in vegetation remote sensing. Sentinel-2 was launched in 2015 and is equipped with a multispectral sensor that samples the electromagnetic spectrum in 13 spectral bands: four bands at 10 m spatial resolution (RGB and NIR), six bands at 20 m resolution (VNIR and SWIR), and three bands at 60 m resolution (aerosols and cirrus detection). It has a temporal resolution of five days in its current two-satellite constellation. Sentinel-1

was launched in 2014 and is equipped with a microwave synthetic-aperture radar (SAR) instrument that operates in the 3.75–7.5 cm wavelength ranges (C-Band). It was designed as a constellation of four satellites with a combined temporal resolution of four days. However, at present, only one of the two already launched satellites is operative. In its main operational mode over land—interferometric wide swath mode (IW)—the signal is acquired in VV+VH polarization.

1.3.2 REFERENCE DATA REQUIREMENTS

Most methods for the analysis of remote sensing data require *ground reference data*, either for model calibration, validation or both. The ground reference data are typically recorded *in situ* within plots or point observations and need to fulfil manifold requirements to suit remote sensing applications (Fassnacht et al., 2016). However, field-based reference data are prone to observer and sampling bias (Asner et al., 2015; Lepš & Hadincová, 1992; Vittoz & Guisan, 2007) and do not always provide exact *ground truth*. A spatially explicit link between the ground reference data and remotely sensed data is prerequisite for any remote sensing application. This link is not trivial to establish (Leitão et al., 2018) and can be hampered by several factors. The geographical position of the field data is measured using a global navigation satellite system (GNSS). The GNSS-measurements in the field typically show positional inaccuracies in the range of decimetres to metres when differential GNSS corrected with ground data is used and even exceed several metres when using stand-alone GNSS, particularly under dense vegetation (Kaartinen et al., 2015; Valbuena et al., 2010). In addition to the positional accuracy, geometric properties of the object under investigation are decisive for the spatial link. So even if the geolocation is precisely determined, for example, the measured tree stem coordinates may not correspond to the tree crowns targeted from above. Scale effects further complicate the link between remote sensing and reference data, as the spatial entities captured (i.e., field plots and raster pixels) represent different processes when recorded at different scales (Anderson, 2018). Remote sensing data originate from the *bird's-eye* view and provide a continuous representation (i.e., raster image) of the landscape and the upper canopy of the vegetation in particular. This perspective does not necessarily match ground-based reference data, which for example in the case of trees is even recorded from the *worm's eye* view. Ideally, reference data are ample, are distributed in space—in case of time-series based approaches also in time—and cover large environmental gradients. Recording suitable ground truth data can be a task that is costly and labor-intensive to accomplish and, hence, one of the most limiting factors for large-scale remote sensing analyses.

1.3.3 UAV AS INTERMEDIARY: LINKING GROUND AND SATELLITE DATA

UAVs¹ are established remote sensing systems used for the acquisition of high-resolution data in local level studies (Anderson & Gaston, 2013). There exist mainly two types of UAVs, i.e., fixed-wing and rotor, and various sensors can be mounted on the platform (e.g., multispectral, thermal, lidar). The geolocation accuracy of the resulting data is in the centimetre range when equipped with a differential GNSS. Imagery acquired by UAV systems can be applied to generate orthorectified mosaics—orthomosaics—through a photogrammetric structure-from-motion (SfM) processing chain. Therefore, the drone is piloted over the survey area in a predefined flight plan and multiple orthophotos are captured with overlapping fields of view. For best reconstruction of vegetation, the flight plan is ideally in a criss-cross pattern (Frey et al., 2018). The spatial resolution of the resulting orthoimagery is typically in the single-digit centimetre range, sometimes even millimetres, and is controlled by the UAV flight height and focal length of the camera.

Recent advancements in the field of robotics have increased the usability and lowered the cost of UAVs. Hence, even off-the-shelf consumer drones can be considered a valuable scientific remote sensing tool and very high-resolution imagery of vegetation is becoming widely available. Consequently, UAVs have been frequently used in ecology and precision agriculture (e.g., Alvarez-Vanhard et al., 2021; Osco et al., 2021; Torresan et al., 2017; Zhang & Zhu, 2023). With their flexible and easy deployment, UAVs enable data acquisition over previously inaccessible areas and allow the coverage of large environmental gradients. Ultimately, UAVs already fulfil many of the previously described reference data requirements (see section 1.3.2). They comprise a flexible and easy method of reference data acquisition in comparison to field-based methods, and they are less subject to observer and sampling bias. A growing body of literature exploits the synergies of UAVs and satellites (e.g., Alvarez-Vanhard et al., 2020; Kattenborn et al., 2019b). In most cases, UAV data could not replace *in situ* reference data, but provided the bridge from ground-based truth to satellite data (Alvarez-Vanhard et al., 2021). Recent advancements in deep learning technology are currently paving new avenues for the interpretation of remote sensing data (see section 1.4) and can help establish stronger synergies, for example through multiscale or data fusion approaches.

1.3.4 REMOTE SENSING IN THE ERA OF BIG DATA

We have come far since the first systematic Earth observation with the launch of Landsat 1 in 1972 (Campbell et al., 2023), and we are currently at the beginning

¹ The term *unmanned* aerial vehicles may be more familiar, but inspired by Joyce et al. (2021) I support the use of an inclusive and gender-neutral language.

of an era of big data in remote sensing. One definition of *big data* are the ‘*three Vs*’—that is, data being collected and stored in increasing *volumes* at accelerating *velocity* and in great *variety*. As of May 2023, there were 1 298 actively operating Earth observation satellites in space according to the Union of Concerned Scientist (www.ucsusa.org/resources/satellite-database). This includes both commercially operated satellites such as the Dove fleet (Planet Labs Inc.) or Worldview (Maxar Technologies Inc.) and satellites operated by government authorities such as the Landsat (NASA) or Sentinel (ESA) fleets. The Sentinel satellites alone generate 16 Terabytes of data every day, and thus manifest the increasing volume and velocity in the era of big data.

With the ever-increasing volume of satellite data, the paradigm of ‘*bringing users to the data rather than data to the users*’ is becoming increasingly important. The velocity of data processing is no less important if not only new data is to be generated, but also to be analysed within an adequate time horizon that fits with ecological objectives. Finally, the variety of different platforms (e.g., UAV, aircraft, or satellite), the different remote sensing methods (i.e., multispectral, hyperspectral, lidar, radar) and the different scales (from the leaf level to individual plants and stands to landscapes) requires unifying frameworks to use the data effectively. To facilitate and standardize access to remote sensing data, the European Commission has launched the Copernicus *data and information access services* (DIAS) platforms providing centralized access to Copernicus data and cloud-based processing services. This concept has been adopted at national level, and in Germany, for example, the two platforms code-de.org for authorities and eo-lab.org for research have been set up. Data analysis and management frameworks, such as *ForceEO* (Frantz, 2019) or *Open Data Cube* (Killough, 2018), facilitate harmonized processing of the raw data. Comparable platforms from commercial providers include, for example, Google Earth Engine (Gorelick et al., 2017) or SentinelHub (Sinergise Ltd.).

In the context of *big data*, it is also noteworthy that there exist several platforms that curate openly available data sets contributed by research groups or citizen scientists, for example, for UAV orthoimagery (e.g., geonadir.com, opendrop.de, and openaerialmap.org), plant photographs (e.g., iNaturalist.org), and biodiversity databases (e.g., TRY plant trait database, Kattge et al., 2020).

1.4 DEEP LEARNING

A method frequently associated with big data is deep learning. Deep learning is a sub-field of machine learning, and both terms fall under the general category of artificial intelligence. In general, machine learning attempts to transform input data into a meaningful output and to learn suitable representations of the input data in the process. For more complex data, this usually requires

manual preparation of the input data—so-called *feature engineering*—for a model to properly learn suitable representations. As a specialization of machine learning, deep learning attempts to learn multiple successive layers of lower- and higher-level data representations, hence the name *deep*. This task is already incorporated by the layered design of deep learning architectures, which greatly simplifies the entire workflow and is usually referred to as *end-to-end learning* (Chollet et al., 2022). In simple terms, deep learning learns *what* and *how* to see simultaneously, whereas machine learning only learns *what* to see (Kattenborn et al., 2021).

1.4.1 FUNDAMENTALS OF DEEP LEARNING

Deep learning methods are based on *neural networks*. A neural network is an interconnected group of *nodes*, and the nodes are organized in *layers*. The first and last layer of a deep neural network are the input and output layers, with at least two internal—or hidden—layers in between. The nodes are interconnected and are arbitrarily initiated with *weights* and *biases*—also called *trainable parameters*. Training of a neural network means adjusting these parameters so that they become meaningful regarding the task at hand. To adjust the parameters, the mismatch between the predicted output—based on the arbitrary initialisation—and the true target is calculated using a *loss function* (Chollet et al., 2022). Typical loss functions are, for example, *mean squared error* for regression tasks, *cross-entropy loss* for classification tasks, or *focal loss* for object detection tasks. Since the described operations are differentiable mathematical functions, the gradient of the loss function can be calculated. This is done by the *optimizer* and tells the direction in which to adjust the parameters to minimize the loss (Chollet et al., 2022). Typically, employed optimizers include *SGD* (stochastic gradient descent), *adam* (adaptive moment estimation), or *RMS-Prop* (root mean square propagation). In simple terms, a neural network is a large chain of differentiable operations and the chain rule can be applied to pass the parameter adjustments through the network starting from the final loss. This central algorithm is termed *backpropagation*. The parameters are iteratively adjusted in epochs by repeatedly passing the training data set through the network. An epoch is defined as a complete pass of the entire training data through the network. Depending on the size of the network, training can be very memory and computation intensive, and the parameter adjustments are therefore done using small batches of data successively. To select the epoch the model was best trained and to prevent the network from overfitting, the data set is split into a training set and a test set, on which the model is later evaluated. After many epochs, the loss of the training set converges towards a minimum and the network will probably begin to overfit. As soon as the network starts to overfit, the loss of the test set stagnates or increases again. This reversal point is the epoch in which the model is best trained. A third validation set is required if *hyperparameters*—architecture-level parameters of the network, such as number of

layers, number of filters per layer, or batch size—are still to be optimized when creating the network. This is because tuning the hyperparameters based on the results of the test set would leak information from the test set into the model, thereby inflating its performance. (Chollet et al., 2022)

A *convolutional neural network* (CNN) is a specialized form of a neural network that is mostly used in image interpretation. Its architecture is built on *convolutional* and *pooling* layers. In its core, CNN learn the data representations via convolutional *filters* (or kernels) that extract (spatial) patterns in the data. The filters are usually small quadratic matrices with an uneven number of rows and columns (e.g., 3×3 or 5×5 matrix) that are moved over the input image where the dot-product is formed. A subsequent pooling layer then downsamples the collected information by selecting a small window (typically 2×2) of the input and by applying a pooling operation (typically the maximum, so-called *max-pooling*). All nodes of consecutive layers are connected to each other (*fully connected*). This structure allows a CNN to learn spatial hierarchical patterns: early filters may recognize simple patterns such as corners or edges, while deeper filters combine these learned pattern and hence can detect higher-level concepts, such as leaves, branches, or flowers. For large, high-resolution image data, the data size often exceeds the available memory, necessitating the division of images into individual tiles. In a segmentation task, training data in the form of masks are also split into the same tiles. To increase the size and heterogeneity of the dataset, data augmentation can be applied. Typically, this involves varying parameters such as saturation, brightness, or contrast, as well as zooming, rotating, or flipping the images.

A form of neural networks specialized for processing and interpretation of sequence data are *recurrent neural networks* (RNN). One particular feature of recurrent neural networks is their incorporated memory state, which enables the stepwise processing of small chunks of sequence data while keeping the overall context in memory. RNNs are known to suffer from the *vanishing* or *exploding gradient problem*, that arises when the parameter adjustments become minimal or large and potentiate during backpropagation for the gradient to eventually vanish or explode. This problem was first described by Hochreiter and Schmidhuber in 1991 and culminated in the introduction of the *long short-term memory network* (LSTM, Hochreiter & Schmidhuber, 1997). The core of an LSTM layer is the LSTM unit that takes temporal dependencies into account by controlling the network memory. It does so using three sigmoid activations (*gate units*): a forget gate, an input gate, and an output gate. Depending on the output of the previous cell and the current input, the forget gate controls whether the previous memory cell state will be kept by means of a *sigmoid* function. The input gate, similarly, controls which part of the memory cell will be updated using a *sigmoid* function, combined with a *tanh* function that creates weights that are then used to update the new cell state. Finally, the output is determined by the output gate that decides which

information of the cell state will be forwarded by means of a *sigmoid* function and a *tanh* function.

1.4.2 DEEP LEARNING IN REMOTE SENSING OF VEGETATION

Machine learning in remote sensing of vegetation first became practicable with the launch of the first digital scanner on board of Landsat-1 in 1972 (Campbell et al., 2023). Early machine learning methods comprise principal component analysis for dimensionality reduction, k-means clustering, or more sophisticated classification and regression methods such as Support Vector Machines (Cortes & Vapnik, 1995) or Random Forests, (Breiman, 2001) which are all well established in current remote sensing. Although the fundamental methods of deep learning have been established since the 1990s, it was only with advances in the development of the appropriate hardware (i.e., graphics processing unit, GPU) that development gained momentum in the 2010s (Chollet et al., 2022). The first scientific articles using deep learning in remote sensing of vegetation emerged in 2016. Based on a literature search on the Web of Science (www.webofscience.com) using the keywords '*remote sensing*', '*deep learning*', and '*vegetation*', the number of related articles has exploded since then to 1 019 publications in total and 271 new articles in 2023 alone (and 137 articles in 2024, as of June). Since its introduction, deep learning applications are increasingly replacing established remote sensing image analysis methods that are either pixel-based or object-oriented analysis methods. CNNs are specifically designed to analyse spatial pattern and are particularly suitable for interpreting remotely sensed imagery, and RNN for analysing sequential data (e.g., satellite image time series) (Brodrick et al., 2019; Hoerer & Kuenzer, 2020; Zhang & Zhu, 2023; Zhu et al., 2017).

CNNs haven proven highly effective in image processing tasks, such as *image classification*, *object detection*, and *semantic segmentation*. In image classification, the overall information of an image is used to assign a label to it, and it is frequently applied for plant identification of herbarium specimen (Younis et al., 2018) and field observations (Labenski et al., 2022; Reeb et al., 2022; Wäldchen & Mäder, 2018). Image classification of remote sensing imagery either relies on prior segmentation of the target (e.g., Hartling et al., 2019; Natesan et al., 2019; Sothe et al., 2020), or predictions are assigned to tiles of an image and subsequently reassembled (e.g., Kattenborn et al., 2020; Qian et al., 2020; Rezaee et al., 2018). Frequently used model architectures for image recognition are, for example, *VGG-16*, *ResNet*, *Inception*, or *EfficientNet*. These models often build the backbone of object detection and segmentation tasks, and pre-trained variants of the former can build the foundation of subsequent specialized applications, to accelerate and facilitate model learning. Object detection extends the concept of image classification and identifies individual occurrences of objects within the image, typically by locating the centre of an object and approximating its extent

using a rectangular bounding box. Object detection is particularly suitable for demarcated objects and in remote sensing of vegetation is often used in agriculture (e.g., Chen et al., 2019; Csillik et al., 2018; Freudenberg et al., 2019) or in natural environments, e.g., for the accounting of individual trees (Weinstein et al., 2019), cacti (López-Jiménez et al., 2019), seedlings (Fromm et al., 2019), or bark beetle infested trees (Safonova et al., 2019). Semantic segmentation aims to delineate the actual extent of an object and assigns a certain class to each pixel. It is ideally suited for remote sensing of vegetation as it best captures the natural, irregular shapes and smooth transitions between species or vegetation types. Frequently used models include *U-net* (Ronneberger et al., 2015), *SegNet* (Badrinarayanan et al., 2017), *FC-DenseNet* (Jégou et al., 2017), and *DeepLabV3+* (Chen et al., 2017). Their applications in remote sensing of vegetation span from mapping single species (e.g. Ferreira et al., 2021; Fricker et al., 2019; Kattenborn et al., 2019a; Popp & Kalwij, 2023; Wagner et al., 2020), to structural components (e.g. Hamdi et al., 2019; Jiang et al., 2019; Kislov & Korznikov, 2020), to vegetation communities or types (e.g. Kattenborn et al., 2019a; Wagner et al., 2019). Instance segmentation goes one step further and segments individual entities of the respective class, for example, individual trees of one species (Beloïu et al., 2023; Braga et al., 2020). Further promising applications of CNNs include, for example, *gap filling* of cloud-obscured optical data by means of radar data (Meraner et al., 2020), improving spatial resolution by means of *super-resolution* (Wang et al., 2022), or *data fusion* of multimodal remote sensing data (Lefèvre et al., 2017).

The high temporal resolution of current satellite missions (see chapter 1.3) provides dense satellite image time series (SITS). Traditional algorithms, such as Random Forests and Support Vector Machines, have been shown to handle the high dimensionality of such time series data, but temporal dependencies remain underexploited (Pelletier et al., 2019b). Specifically designed deep learning algorithms reveal the recurring pattern in sequential data and are ideally suited in the analysis of such time series data (Reichstein et al., 2019; Zhong et al., 2019; Zhu et al., 2017). Typical model architectures include, for example, RNNs, LSTMs, and Transformers. They have been used for the classification of land use and land cover types (Campos-Taberner et al., 2020; Rußwurm & Körner, 2017, 2018; Yuan & Lin, 2021), tree species (Xi et al., 2021), and wildfire detection (Kong et al., 2018).

1.5 RESEARCH NEEDS

Increased tree mortality has been observed globally (Allen et al., 2010; Byer & Jin, 2017; Rakovec et al., 2022; Senf et al., 2018), but the exact extent and causes are not yet fully explored at the landscape-level (Allen et al., 2010; Hartmann et al., 2018a). Remote sensing has proven to be an effective method for characterizing vegetation on large scales, and numerous satellites provide medium- to high-

resolution data in terms of space and time. The large stream of daily acquired satellite data (*big data*) presents both advantages and disadvantages. On one hand, most applications benefit from the high spatial and temporal resolution of these images. On the other hand, the sheer volume of data poses significant challenges in handling and utilizing it effectively. However, the spatial resolution of these satellite data is above the size of individual trees, which hampers the link with ground reference data. The resulting lack of reference data is the primary limitation for large-scale satellite-based remote sensing methods in detecting deadwood, leading to an incomplete understanding of the processes causing tree mortality. UAVs can bridge the gap between ground reference data and satellite data by providing high-resolution imagery suitable for detecting individual trees. Given the large quantity and diversity of remote sensing data, along with the high spatial resolution of UAV data and the high temporal resolution of satellite image time series, traditional remote sensing methods are reaching their limits. This necessitates the development of adapted methods. Deep learning techniques have already proven effective in other disciplines, such as CNN for image data interpretation (e.g., classification, object detection) and LSTM for processing sequential information (e.g., speech recognition).

The aim of this thesis therefore is twofold: **(1)** evaluating deep learning approaches for remote sensing of vegetation and **(2)** integrating multimodal and multidimensional remote sensing data from UAVs and satellites. Both objectives are based on the underlying question of how this aids understanding patterns and drivers of tree mortality. At the core of this thesis is the upscaling approach: initially, CNNs are used to automatically segment standing deadwood from UAV-based orthomosaics. The detected deadwood then acts as reference data for LSTMs, which leverage satellite image time series (i.e., Sentinel-1 and Sentinel-2) to facilitate large-scale detection of standing deadwood across Germany. The following main research questions are investigated and sought to be answered:

1. How are deep learning algorithms suited to analyse the dense spatial information in very high-resolution remote sensing data?
2. In what way is the concerted use of UAVs and deep learning capable of closing the reference data gap on tree mortality?
3. To what extent is deep learning suitable for extracting temporal information from satellite image time series?
4. What are the spatio-temporal patterns and environmental drivers of tree mortality in Germany?

These main research questions are examined in three studies that have been published in international peer-reviewed scientific journals (chapters 2 and 3)

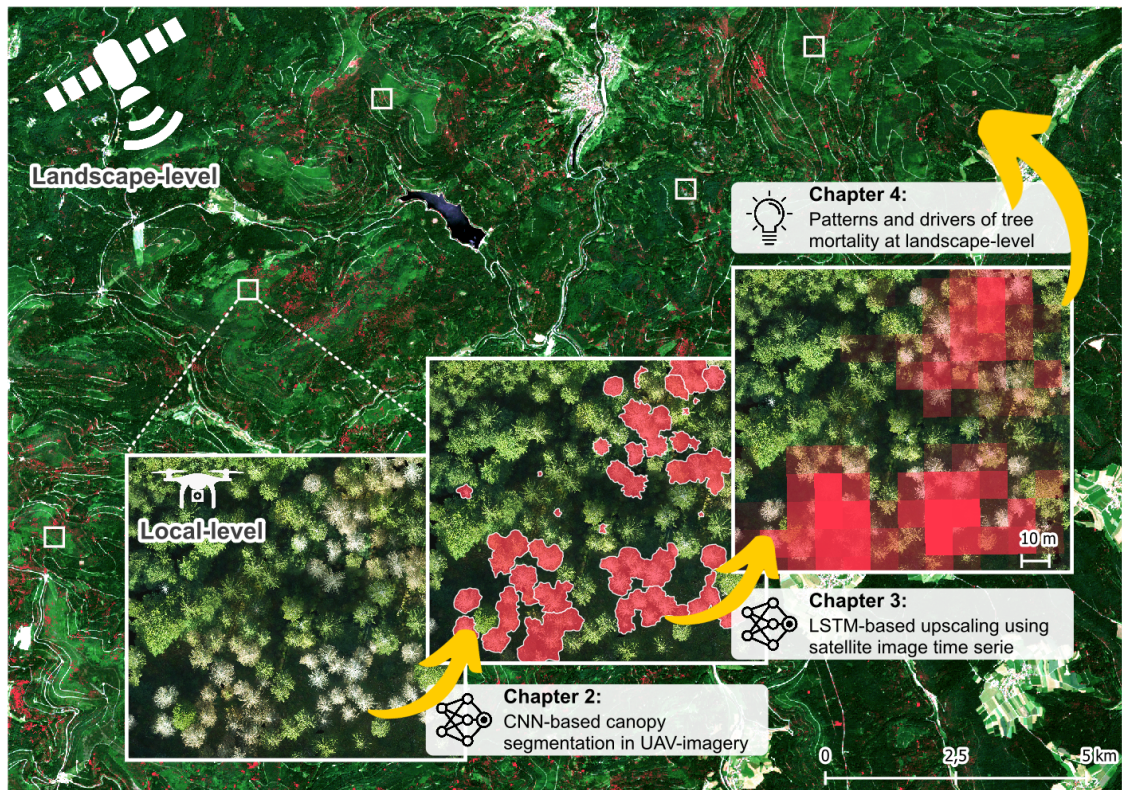


Figure 1.1: Overview of the upscaling approach presented in this thesis: (1) automated classification and segmentation of standing deadwood in high-resolution UAV-imagery using CNN (chapter 2); (2) utilization of these segmented canopies as reference data for LSTM models for area-wide mapping of tree mortality from satellite data time series (chapter 3); (3) enhanced understanding of patterns and drivers of tree mortality at the landscape level (chapter 4).

or currently have been submitted for peer review (chapter 4). In chapter 2, I assess the potential of CNNs to map forest tree species from very high-resolution UAV-based RGB imagery. I test this on 51 UAV-orthomosaics and over a large and heterogeneous sample of mixed stands of forest trees. Since little is known about the requirements of remote sensing data for deep learning approaches, I therefore test several spatial resolutions, the additional value of photogrammetric 3D-information, and different tile sizes of the input images.

To compensate for the lack of ground reference data on tree mortality, in chapter 3, I propose an upscaling approach in which fine-scaled patterns in UAV imagery are harnessed to create ample reference data. I use this local-level data for training models that predict standing deadwood at the landscape-level using multitemporal and multispectral information of satellite data. I seek to answer the questions, whether CNN-based predictions of standing deadwood are robust across a wide range of forest stand characteristics and over multiple

years. Subsequently, these predictions are input to a long short-term memory model (LSTM) to infer fractional cover of standing deadwood based on Sentinel-1 and Sentinel-2 time series data. I further test whether this upscaling approach is transferable across regions and different years.

This upscaling approach enables the extrapolation of local-level deadwood observations to entire landscapes. In chapter 4, I want to assess the suitability of the resulting Germany-wide maps of standing deadwood for investigating the processes of tree mortality at the landscape level. To this end, I look at the spatial and temporal patterns of standing deadwood in Germany and compare the patterns found with other remote sensing and ground-based assessments. To investigate the drivers of the observed tree mortality, I look at the influence of several environmental parameters on the occurrence of standing deadwood.

2 MAPPING FOREST TREE SPECIES IN HIGH RESOLUTION UAV-BASED RGB-IMAGERY BY MEANS OF CONVOLUTIONAL NEURAL NETWORKS

This chapter has been published as: Schiefer, F., Kattenborn, T., Frick, A., Frey, J., Schall, P., Koch, B., & Schmidlein, S. (2020). Mapping forest tree species in high resolution UAV-based RGB-imagery by means of convolutional neural networks. *ISPRS Journal of Photogrammetry and Remote Sensing*, 170, 205–215. <https://doi.org/10/ghrrhs>

ABSTRACT

The use of uncrewed aerial vehicles (UAV) in vegetation remote sensing allows a time-flexible and cost-effective acquisition of very high-resolution imagery. Still, current methods for the mapping of forest tree species do not exploit the respective, rich spatial information. Here, we assessed the potential of convolutional neural networks (CNN) and very high-resolution RGB imagery from UAVs for the mapping of tree species in temperate forests. We used multicopter UAVs to obtain very high-resolution (<2 cm) RGB imagery over 51 ha of temperate forests in the Southern Black Forest region, and the Hainich National Park in Germany. To fully harness the end-to-end learning capabilities of CNNs, we used a semantic segmentation approach (U-net) that concurrently segments and classifies tree species from imagery. With a diverse dataset in terms of study areas, site conditions, illumination properties, and phenology, we accurately mapped nine tree species, three genus-level classes, deadwood, and forest floor (mean F1-score 0.73). A larger tile size during CNN training negatively affected the model accuracies for underrepresented classes. Additional height information from normalized digital surface models slightly increased the model accuracy but increased computational complexity and data requirements. A coarser spatial resolution substantially reduced the model accuracy (mean F1-score of 0.26 at 32 cm resolution). Our results highlight the key role that UAVs can play in the mapping of forest tree species, given that air- and spaceborne remote sensing currently does not provide comparable spatial resolutions. The end-to-end learning capability of CNNs makes extensive preprocessing partly obsolete. The use of large and diverse datasets facilitates a high degree of generalization of the CNN, thus fostering transferability. The synergy of high-resolution UAV imagery and CNN provides a fast and flexible yet accurate means of mapping forest tree species.

2.1 INTRODUCTION

Forest ecosystems cover about one-third of the Earth's land area (FAO, 2020), providing countless and substantial ecosystem services. There is, therefore, great interest in obtaining information on the state of forest ecosystems. Many problems in this context require the acquisition of tree species composition at a high spatial resolution—a goal to which remote sensing can ultimately contribute significantly (Fassnacht et al., 2016). A combination of two technological and methodological advances offers great potential for accurately mapping forest tree species: the use of uncrewed aerial vehicles (UAV) and deep learning. Whereas the use of very high-resolution UAV-data is no novelty in this regard (Franklin & Ahmed, 2018; Gini et al., 2014; Michez et al., 2016; Nevalainen et al., 2017), deep learning is only recently being introduced into vegetation remote sensing (Audebert et al., 2019; Brodrick et al., 2019; Ma et al., 2019; Zhang et al., 2016; Zhu et al., 2017).

The most effective deep learning algorithms in analysing high spatial resolution remote sensing data are convolutional neural networks (CNN) since these are specifically designed to analyse spatial patterns. CNNs autonomously extract low-, mid- and high-level feature representations (e.g., corners, edges, abstract shapes) that best describe targets, such as classes or continuous values, through a series of convolutions and pooling operations. Several studies have already used CNNs and very high-resolution remote sensing data for the mapping of tree species. To detect tree individuals outside forests, good results have been reported from urban environments (Hartling et al., 2019; Lobo Torres et al., 2020; Santos et al., 2019), and plantations (Csillik et al., 2018; Freudenberg et al., 2019; Li et al., 2017; Osco et al., 2020) but these results are hardly transferable to heterogeneous forest. Specifically targeting forest environments, Fricker et al. (2019) used a CNN for classifying and mapping seven tree species in a mixed-conifer forest from airborne data, with very accurate results for hyperspectral and moderately accurate results for pseudo-RGB data. Trier et al. (2018) also used airborne hyperspectral data to classify pine, spruce, and birch trees in a boreal forest using a CNN. Nezami et al. (2020) showed very accurate results for classifying the same tree species testing CNNs with different combinations of hyperspectral and RGB imagery and canopy height models. Thus far, mapping tree species in forests often requires high spectral resolution data, which is cumbersome to access for non-specialist users. Solely relying on RGB information, individual tree species have been accurately mapped against a background of other species using CNNs (Kattenborn et al., 2019a, 2020; López-Jiménez et al., 2019; Morales et al., 2018; Wagner et al., 2020). Natesan et al. (2019) used a CNN to classify previously extracted tree crowns from RGB data into white pine, red pine, and non-pine. Spectral resolution notwithstanding, many studies used additional preprocessing steps prior to classification (e.g., tree segmentation or tree localization from ancillary remote sensing data, background

removal, feature engineering), which limits the transferability and increases the computational load of such applications.

With consumer-grade UAVs on the rise, which enable easy and low-cost acquisition of very high-resolution RGB data, the mapping of tree species in heterogeneous forests using solely RGB imagery is of high interest, as it does not rely on sophisticated sensors, does not require extensive calibration and preprocessing and, therefore, enables the application by a wide audience (Komárek, 2020). The above-mentioned studies demonstrated that, regardless of the spectral resolution, high spatial resolution remote sensing data can be sufficient for mapping tree species when small samples of species or relatively homogeneous environments with little site variability are considered.

To further assess the potential of very high-resolution imagery for mapping forest tree species, it would be desirable to test CNNs on a large and heterogeneous sample of species with a wide gradient of forest types, site conditions, and stand structures. Moreover, such an assessment based on RGB imagery alone would be valuable, since the use of RGB data ensures access to such applications for a wide audience. Recent CNN architectures for semantic segmentation (e.g., U-Net (Ronneberger et al., 2015) or DenseNet (Jégou et al., 2017)) facilitate end-to-end learning that can be directly applied on the raw remote sensing data and enable mapping at the original image resolution and overcome the need for prior segmentation and feature engineering steps. Here, we would like to assess the potential of very high-resolution RGB imagery from UAVs to map forest tree species with a large and heterogeneous sample on mixed stands of forest trees. We used CNNs to map tree species from UAV-based very high-resolution RGB imagery in temperate deciduous and mixed-coniferous forests in Germany. We used a multiclass semantic segmentation approach (U-net) to simultaneously segment and classify 14 classes (i.e., nine tree species, three genus-level classes, deadwood, and forest floor). Our main research question is as follows: Is RGB imagery sufficient to accurately map tree species in heterogeneous forests? Moreover, given the very recent introduction of CNNs into vegetation remote sensing, little is known about the requirements regarding the remote sensing data. We, therefore, tested several spatial resolutions, the additional value of photogrammetric 3D-information, and different tile sizes of the input images.

2.2 MATERIAL AND METHODS

2.2.1 STUDY AREA

The study area is in the Southern Black Forest region and the Hainich National park (NP), in the German states of Baden-Württemberg and Thuringia, respectively (Figure 2.1). The Southern Black Forest study site is situated in a mountain range

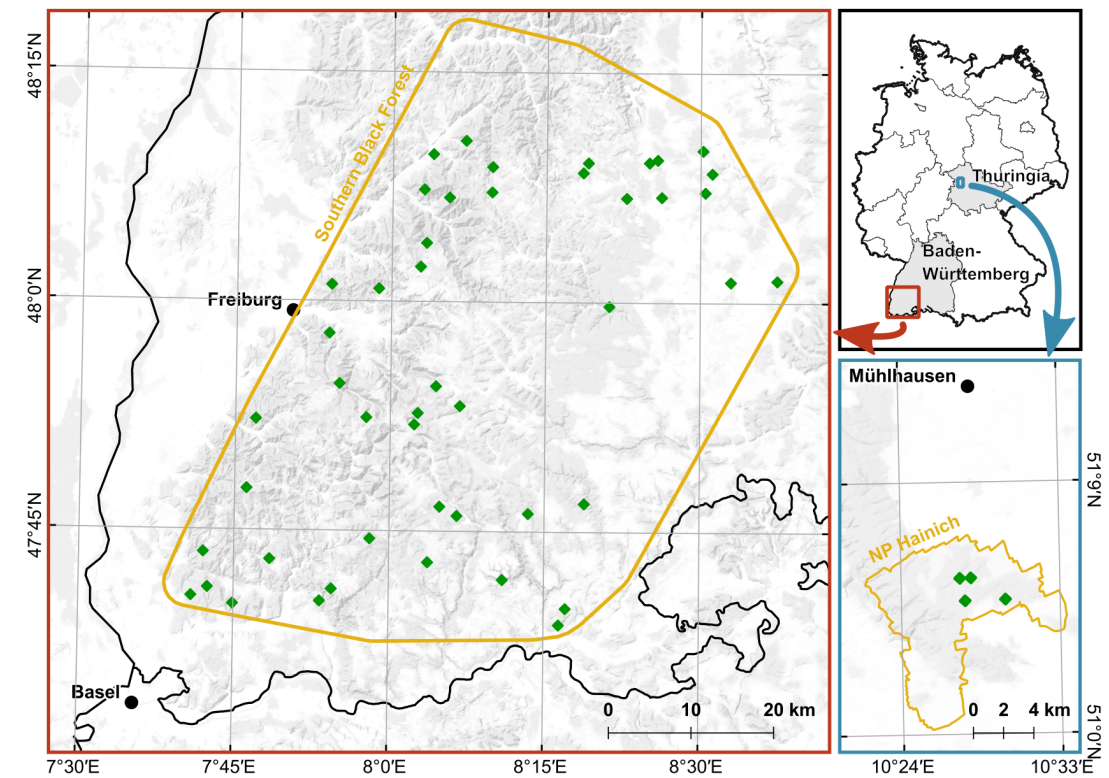


Figure 2.1: Map of the two study areas, Southern Black Forest and Hainich NP in Germany. Green markers indicate the locations of the research plots. Projection: WGS84 UTM Zone 32N

between 120 and 1492 m a.s.l. between the Rhine valley and the highest peak at Feldberg. The area is mostly covered by mixed and coniferous forests, largely managed for timber production (Kändler & Cullmann, 2015), and covers a wide range of forest types and age classes (Frey et al., 2018). The main tree species are *Picea abies* L. (40% cover), *Fagus sylvatica* L. (18%), and *Abies alba* Mill. (13%). Less common tree species are *Quercus robur* L. (5%), *Pinus sylvestris* L. (4%), and *Pseudotsuga menziesii* Mirbel (4%). Parent rock mainly consists of granite and gneiss, with some admixture of sandstone (Storch et al., 2020).

The Hainich NP lies on a ridge between 225 and 494 m a.s.l. and covers an area of 7600 ha. It is characterized by unmanaged mixed deciduous forests on limestone and dominated by *F. sylvatica*. Subordinate species include *Fraxinus excelsior* L., *Acer pseudoplatanus* L., *Acer platanoides* L., *Q. robur*, *Quercus petraea* (Matt.) Liebl., *Tilia cordata* Mill., *Tilia platyphyllos* Scop., *Carpinus betulus* L., and others. The heterogeneity of both study areas is exemplified by the forest inventory plots (details, see section 2.2.2), with species numbers per plot between two and ten and tree densities ranging from 179 and 851 trees per hectare.

2.2.2 DATA ACQUISITION

The ConFoBi-Project (Conservation of Forest Biodiversity in Multiple-Use Landscapes of Central Europe) has implemented 135 research plots (100 × 100 m) within state-owned forests in the Southern Black Forest region (Storch et al., 2020). A full forest inventory was conducted between October 2016 and February 2018. In each plot, we recorded tree species, diameter at breast height DBH, and height of all trees with a DBH \geq 7 cm. In addition, each plot was inventoried with an octocopter UAV (OktoXL 6S12, Mikrokopter GmbH, Moormerland, Germany) carrying a consumer-grade full-frame RGB camera (Alpha 7R, Sony Europe Limited, Weybridge, Surrey, UK) with a 35 mm prime lens. Flights were carried out in snowless conditions between March 2017 and April 2018. For each flight, the UAV maintained an altitude of 80 m above ground at a flight speed of 3.5 m/s and followed a criss-cross pattern using the onboard GNSS (see Frey et al., 2018, for details). The camera was aligned nadir and perpendicular to the flight direction, and triggered automatically every 3–4 m of the flight track. This resulted in forward overlaps of $>95\%$ and ground sampling distances of about 1.1 cm. Because we adopted an area-wide digitization of the reference data to gain a full picture of the model performance across sites, the digitization of all plots would have been too labor-intensive and we randomly selected 47 plots. From all 135 plots, plots with leaf-off conditions, plantation-like forest structures as overly easy targets, or cloud shadows in parts of a scene were excluded.

Within the Biodiversity Exploratories framework (Fischer et al., 2010), 13 research plots (100 × 100 m) were implemented in the Hainich NP. In the off-season from 2014–2015, all plots were surveyed and trees with a DBH \geq 7 cm were recorded with species information, DBH, tree height, and geographic location of the stem (Schall et al., 2018). For 4 of these plots, UAV based RGB imagery was acquired in September 2019 with a DJI Phantom 4 Pro+ (DJI Technology Co., Ltd., Shenzhen, China) quadcopter with a ground sampling distance of <1.35 cm, at a flight speed of 2.8 m/s, and forward overlap of 90%.

We derived a total of 51 orthomosaics using a Structure from Motion-based photogrammetric processing chain in Agisoft Metashape v.1.5.4 (Agisoft LLC, St. Petersburg, Russia). This included filtering of blurry images, image matching, and dense point-cloud creation. Digital elevation models were derived from the dense point cloud. Orthomosaics were created by projecting single images on digital elevation models. Georeferencing was performed automatically based on the GNSS trajectory logs of the respective UAV. We calculated normalized digital surface models (nDSMs) via subtraction of digital terrain models. The digital terrain models were derived from airborne laser scans with 1 m resolution and were provided by the states Baden-Württemberg (State Agency for Spatial Information and Rural Development Baden-Württemberg, LGL, Stuttgart, www.lgl-bw.de) and Thuringia (State Agency for Land Management and Geoinformation, TLBG, Erfurt,

www.geoportal-th.de). Orthomosaics were resampled to a spatial resolution of 2 cm. To compensate for differences in the illumination properties of the individual UAV scenes, we applied a histogram stretch to the 0.01 and 99.99% percentiles to all orthomosaics.

2.2.3 REFERENCE DATA EXTRACTION

Training of the U-net segmentation algorithm requires regular tiles of the RGB imagery. Besides, classified areas in the form of masks need to be provided for training. We derived these masks by visual interpretation and manual delineation of classes in the orthomosaics and normalized digital surface models (nDSM) using ArcGIS v.10.6.1 (ESRI, Redlands, CA, USA). A total of nine tree species, three genus-level classes, deadwood, and forest floor were classified in this study (Figure 2.2). Tree species composition, tree height, DBH, and relative position of trees from the forest inventory data aided the visual classification. For each plot, we digitized the classes. We did not explicitly delineate tree individuals because this was beyond the scope of the study. Delineation and the class assignment were cross-checked by at least one other interpreter. The visual, area-wide classification is not a necessity of the CNN approach, but it was, as already mentioned above, a requirement for gaining a comprehensive picture of the model performance across sites and with different tile sizes. Parts of the canopy that could not be assigned to classes with certainty (0.07% of the area, i.e., due to blurry image areas) were excluded from further analysis. The area-related share of a species in the dataset and the number of sites in which the species occurred is shown in Table 2.1. We tested squared tiles with three different edge sizes: 128 pixel, 256 pixel, and 512 pixel corresponding to 2.56 m, 5.12 m, and 10.24 m, respectively. We seamlessly cropped orthomosaics and class delineations into non-overlapping tiles, resulting in a maximum of 36^2 , 18^2 , and 9^2 tiles for the respective tile sizes per scene. Tiles containing empty raster cells (artefacts from the SfM-workflow caused by too little image overlap) in the orthomosaics or unidentified species in the mask were excluded from further analysis. In total, we extracted 62 826, 15 094, and 3 112 tiles for the respective tile sizes.

2.2.4 DATA SPLITTING

Training of a CNN is performed in epochs, which are defined as one complete pass through a training dataset. To assess whether a CNN is starting to over-optimize on training data, the CNN is evaluated against a validation dataset after each epoch. To get an independent assessment of the model accuracy, a model has to be evaluated with independent test data. Prior to model training, we randomly sampled 10% of the dataset (based on the 512-pixel tiles) as independent test

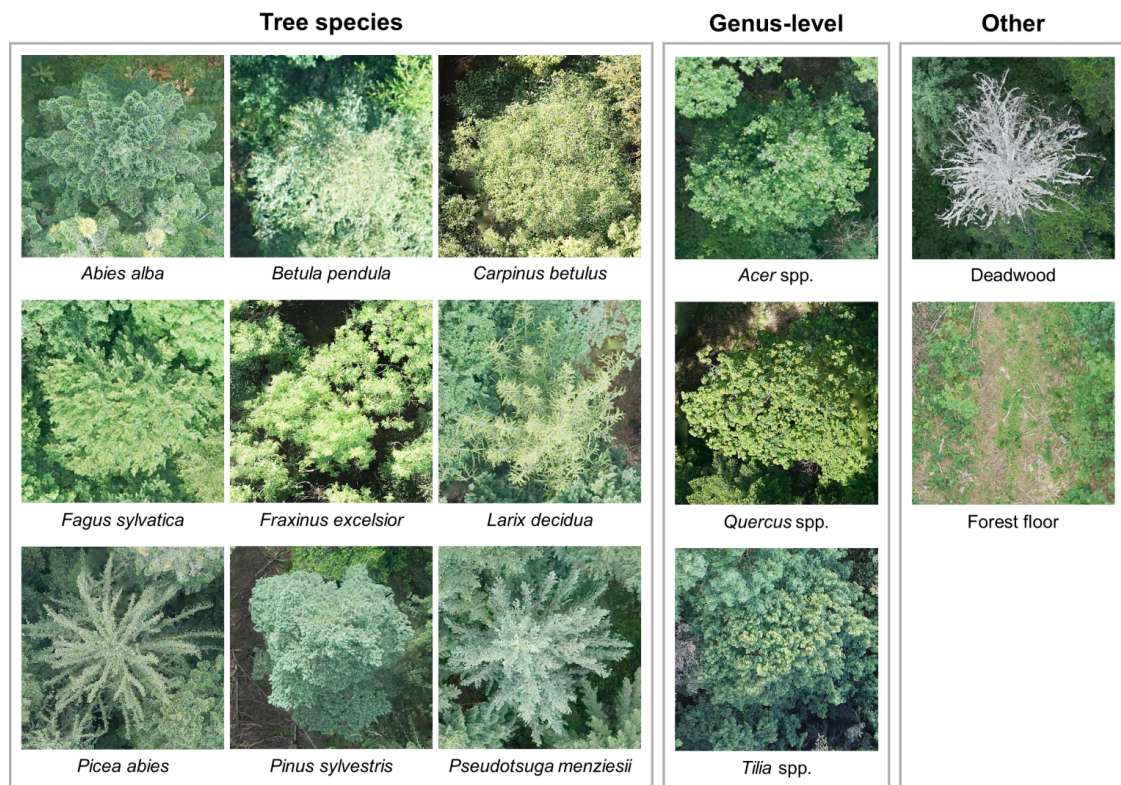


Figure 2.2: Detailed overview of the occurring tree species and classes.

data. Additionally, for visual inspection of the results, the UAV-scene of an entire 100×100 m plot was set aside. The area covered by the 512-pixel test tiles was also used for the test datasets of the smaller tiles, with an accordingly higher resulting number of tiles. With the same procedure as for the test dataset, we randomly split the remaining dataset into 75% for model training and 25% for model validation.

2.2.5 CNN-BASED TREE SPECIES MAPPING

For tree species mapping, we adapted the U-net CNN-architecture (Ronneberger et al., 2015, Figure 2.3). The U-net consists of a contracting path (Figure 2.3, left side) to capture context and a symmetric expanding path (Figure 2.3, right side) to map the contextual information to the original image resolution. In our implementation, the contracting path featured four blocks. Each block consisted of two 3×3 convolutions, both followed by batch normalization and Rectifier linear unit (ReLU) activation. A 2×2 max pooling operation with a striding of two concluded each block, reducing the spatial dimensions of the feature maps by half. After each max pooling operation, we doubled the number of

feature maps. Each block of the expanding path consisted of up-sampling of the feature maps and subsequent 2×2 convolution (“*up-convolution*”), reducing the number of feature maps by half. The resulting feature maps were concatenated with the feature maps of the corresponding blocks from the contracting path. This was followed by repeated 3×3 convolutions, batch normalization, and ReLU activation. With each block of the expanding path, we halved the number of feature maps and doubled the spatial dimensions. The pixel-wise classification was performed at a subsequent 1×1 convolutional layer with a softmax activation. This softmax activation mapped the learned features to the final class probabilities. The maximum class probability of a pixel represented the final class of the respective pixel.

Due to the imbalanced distribution of the tree species (Table 2.1), we used weighted categorical cross entropy as loss function during model training. Thereby, the categorical cross entropy between masks and model output was weighted by the area-related share of a species; in this case inversely proportional. As optimizer, we chose RMSprop with a learning rate of $1e-4$. For better model generalization, we performed a random data augmentation during model training. This augmentation included inflating the training dataset to four times its size, applying random horizontal and vertical flips, and randomly changing brightness (90–110%) and contrast (80–120%) values of input tiles. Models were trained for 40 epochs with batch sizes of 3, 12, and 46 for 128×128 , 256×256 , and 512×512 pixel tiles, respectively. The epoch with the lowest loss value from the validation dataset was kept as the final model. All code was written in R v.3.6.3 (R Core Team, 2020), using the packages ‘tensorflow’ (Allaire et al., 2019b), ‘keras’ (Allaire et al., 2019a), ‘tfdatasets’ (Allaire et al., 2019c), and ‘tibble’ (Müller & Wickham, 2019), and is available at <https://github.com/FelixSchiefer/TreeSeg>. We used the R interface to Keras (Chollet & Allaire, 2017) with the TensorFlow backend v.2.0.0 (Abadi et al., 2016). Training of a CNN model on a CUDA-compatible NVIDIA GPU (GeForce RTX 2080 Ti, 11 GB RAM) and the cuDNN library (Chetlur et al., 2014) took between 7–14 hours. Upon request, the data used in this study can also be made available.

2.2.6 ACCURACY ASSESSMENT

To analyse the effects of the tile size, height information, and spatial resolution on CNN accuracy, we compared the results of several models. Three CNNs were trained with RGB data; each with a different tile size. Another three CNNs were trained with RGB+nDSM data; each with a different tile size. To analyse the influence of spatial resolution, we trained four CNNs with RGB+nDSM data and a fixed tile size of 256×256 pixel; each with a different spatial resolution (4, 8, 16, and 32 cm). We compared manually delineated tree crowns from the

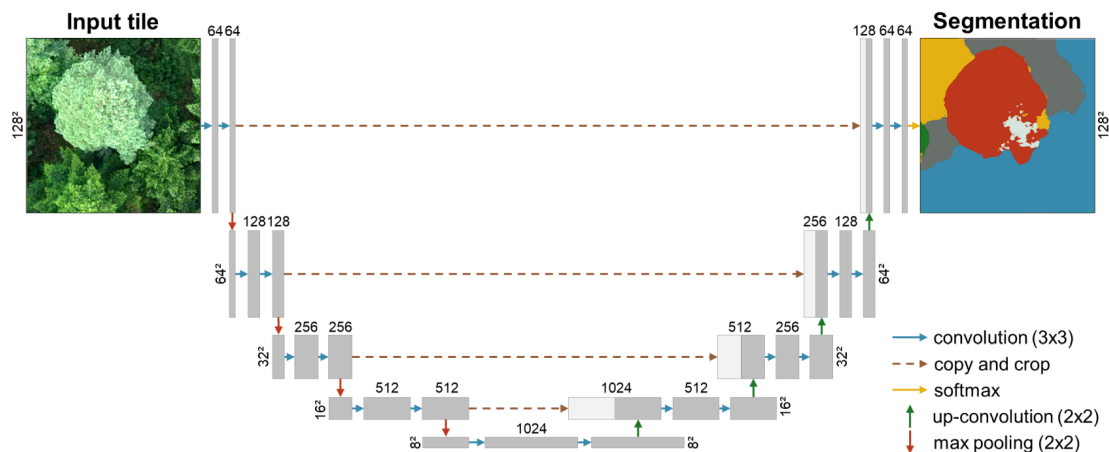


Figure 2.3: Adapted U-net CNN-architecture for the tree species segmentation (Ronneberger et al., 2015). This scheme illustrates how 128×128 pixel tiles were analysed. Values on top of the boxes depict the number of calculated feature maps with the respective x-y-dimensions as vertically oriented labels.

test dataset with CNN predictions to evaluate CNN models based on Overall accuracy (OA), precision, recall, and F1-score (harmonic mean of precision and recall). The reported accuracies are based on the pixel-level. For visual inspection, we applied the best model to an entire UAV-scene that was not used during model training. We used a moving window approach with a half tile size overlap in x- and y-direction. From the resulting nine predictions per pixel, final predictions were derived through majority vote.

2.3 RESULTS

2.3.1 MODEL TRAINING

For each model, the validation loss reached a minimum during the 40 epochs (Figure 2.4). After reaching its minimum, the training loss for all models converged towards zero (not depicted) whereas the validation loss stagnated or increased again. Models that were trained with smaller tiles, displayed a faster decrease in validation loss.

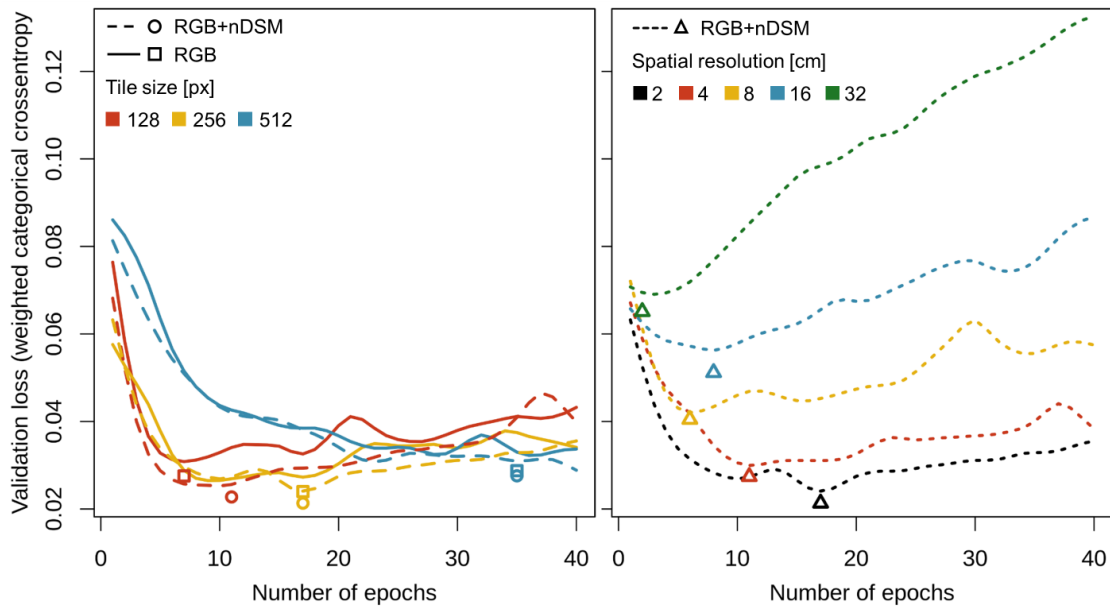


Figure 2.4: Validation loss during CNN model training. Curves were smoothed for better visualization. The symbols represent the unsmoothed validation loss of the best epoch.

2.3.2 MODEL RESULTS

The model that performed best was trained with RGB+nDSM data and a tile size of 128×128 pixel (OA = 89%, mean F1-Score = 73%), albeit only marginally better than models trained only with RGB data or with a larger tile size (Table 2.1). A coarser spatial resolution resulted in overall accuracy reduction from 89% at 2 cm to 62% at 32 cm resolution, and mean F1-scores from 67% to 26%. Class-specific F1-scores were highest for *P. abies* (93%). Moreover, these scores did not differ much between models with different tile sizes, especially not for abundant species (i.e., *P. abies*, *F. sylvatica*, *A. alba*, *P. menziesii*, and *P. sylvestris*). For underrepresented species (i.e., *Acer spp.*, *F. excelsior*, *L. decidua*, *Quercus spp.*, *C. betulus*, *Tilia spp.*, and *B. pendula*), however, larger tile sizes resulted in lower F1-scores, with rare classes no longer being classified.

The use of weighted categorical cross entropy did not compensate for the imbalanced dataset. Setting the weights higher even worsened the results (see Appendix A1 for details). The same applied for models with a decreasing spatial resolution; 13 out of 14 classes were recognized at a spatial resolution of 4 cm, but only 8 classes at 32 cm resolution. Such decrease in model accuracy was even more evident for classes with a lower share. For example, *Larix decidua* had a high F1-score at 2 cm spatial resolution (F1 = 89%), but was not classified at 32 cm

Table 2.1: Tree species mapping model accuracies. Classes are sorted descending by their area-related share. For each class, the highest class-specific F1 score is highlighted in bold.

Input data	Tile size [pixel]				Spatial resolution [cm]					Area-related share ^a	Occ. ^b				
	128	256	512		128	256	512	2	4			8	16	32	
F1-Score															
<i>Picea abies</i>	0.89	0.93	0.91		0.93	0.93	0.93	0.93	0.93	0.91	0.86	0.81	0.70	32.97	45
<i>Fagus sylvatica</i>	0.89	0.90	0.87		0.90	0.90	0.86	0.90	0.86	0.86	0.79	0.75	0.66	29.80	46
<i>Abies alba</i>	0.79	0.85	0.86		0.86	0.87	0.86	0.87	0.83	0.60	0.60	0.60	0.34	10.91	37
<i>Pseudotsuga menziesii</i>	0.84	0.89	0.74		0.89	0.91	0.88	0.91	0.86	0.79	0.77	0.36	0.36	3.89	12
<i>Pinus sylvestris</i>	0.89	0.90	0.89		0.91	0.91	0.87	0.91	0.81	0.78	0.60	0.24	0.24	3.59	19
<i>Acer spp.</i>	0.70	0.72	0.53		0.80	0.73	0.40	0.73	0.60	0.40	0.37	0.12	0.12	2.33	23
<i>Fraxinus excelsior</i>	0.75	0.79	0.16		0.87	0.82	0.52	0.82	0.59	0.28	0.15	-	-	1.01	14
<i>Larix decidua</i>	0.80	0.82	0.80		0.83	0.89	0.82	0.89	0.65	0.21	0.17	-	-	0.98	19
<i>Quercus spp.</i>	0.64	0.49	0.28		0.58	0.39	0.02	0.39	0.38	0.00	-	-	-	0.88	10
<i>Carpinus betulus</i>	0.45	0.33	-		0.38	0.36	0.00	0.36	0.24	0.08	0.06	-	-	0.39	4
<i>Tilia spp.</i>	0.26	0.20	-		0.50	0.02	-	0.02	0.01	-	-	-	-	0.24	4
<i>Betula pendula</i>	0.07	0.33	-		0.27	-	-	-	-	-	-	-	-	0.20	8
Forest floor	0.78	0.83	0.82		0.83	0.84	0.84	0.84	0.84	0.82	0.80	0.77	0.72	11.79	50
Deadwood	0.71	0.73	0.68		0.72	0.75	0.69	0.75	0.70	0.53	0.57	0.44	0.44	0.95	44
Mean F1-Score	0.68	0.69	0.54		0.73	0.67	0.55	0.67	0.59	0.44	0.40	0.26	0.26		
Overall Accuracy	0.86	0.88	0.86		0.89	0.89	0.87	0.89	0.85	0.78	0.73	0.62	0.62		

^a Area-related share of the class in the dataset [%]. ^b Occurrence of class in number of sites

spatial resolution. This variation was species-dependent. For example, for *P. abies* the F1-score decreased far less, from 93% at a spatial resolution of 4 cm to 70% at 32 cm resolution. Site-specific F1-scores did not show large fluctuations over the research plots from different study areas and years (see Appendix A2 for details).

2.3.3 PREDICTION ON INDEPENDENT SCENE

We applied the best model (i.e., CNN trained with RGB+nDSM on 128×128 pixel tiles) to a UAV-scene that had not been used for training (Figure 2.5). Model inference took about 3 minutes for the entire 100×100 m UAV-scene. Abundant classes were almost perfectly predicted, but the model struggled with underrepresented classes. The CNN predictions on larger tiles resulted in similar patterns, but edge effects of the tiles were less pronounced (not shown).

2.4 DISCUSSION

2.4.1 MODEL PERFORMANCE

The model accuracies achieved in our study were relatively high, especially when considering the high number of 14 classes (i.e., nine tree species, three genus-level classes, deadwood, and forest floor) and the fact that we only used RGB imagery. Moreover, our data are characterized by a high degree of heterogeneity, as they include different forest types (i.e., mixed, deciduous and coniferous), different types of use (i.e., unmanaged forests in Hainich NP and commercial forest in the Southern Black Forest), and feature a diverse age structure. By using a semantic segmentation approach, no tree segmentation or localization steps prior to model inference were required, allowing us to fully exploit the end-to-end learning capabilities of CNNs. The classification of comparably high numbers of tree species using CNNs has been demonstrated in subtropical forests (OA = 84%), but hyperspectral UAV data was used and the targeted tree crowns were previously extracted from the imagery (Sothe et al., 2020). Similar accuracies have been reported for the classification of seven tree species in mixed coniferous forest using airborne hyperspectral data (F1 = 87%) and pseudo-RGB data (F1 = 64%), after previous identification of the trees in lidar-derived canopy height models (Fricker et al., 2019). After the removal of shadowed, low-, and non-vegetated pixels prior to CNN-classification, *P. abies*, *P. sylvestris*, and *B. pendula* have been mapped in boreal forests in airborne hyperspectral data (OA = 87%) and RGB data (OA = 74%) (Trier et al., 2018). The same species have been mapped with different combinations of hyperspectral data, RGB imagery, and canopy height models with the highest accuracies (OA = 98%) (Nezami et al., 2020). CNNs have been successfully used to classify two *Pinus* species and non-*Pinus* in previously

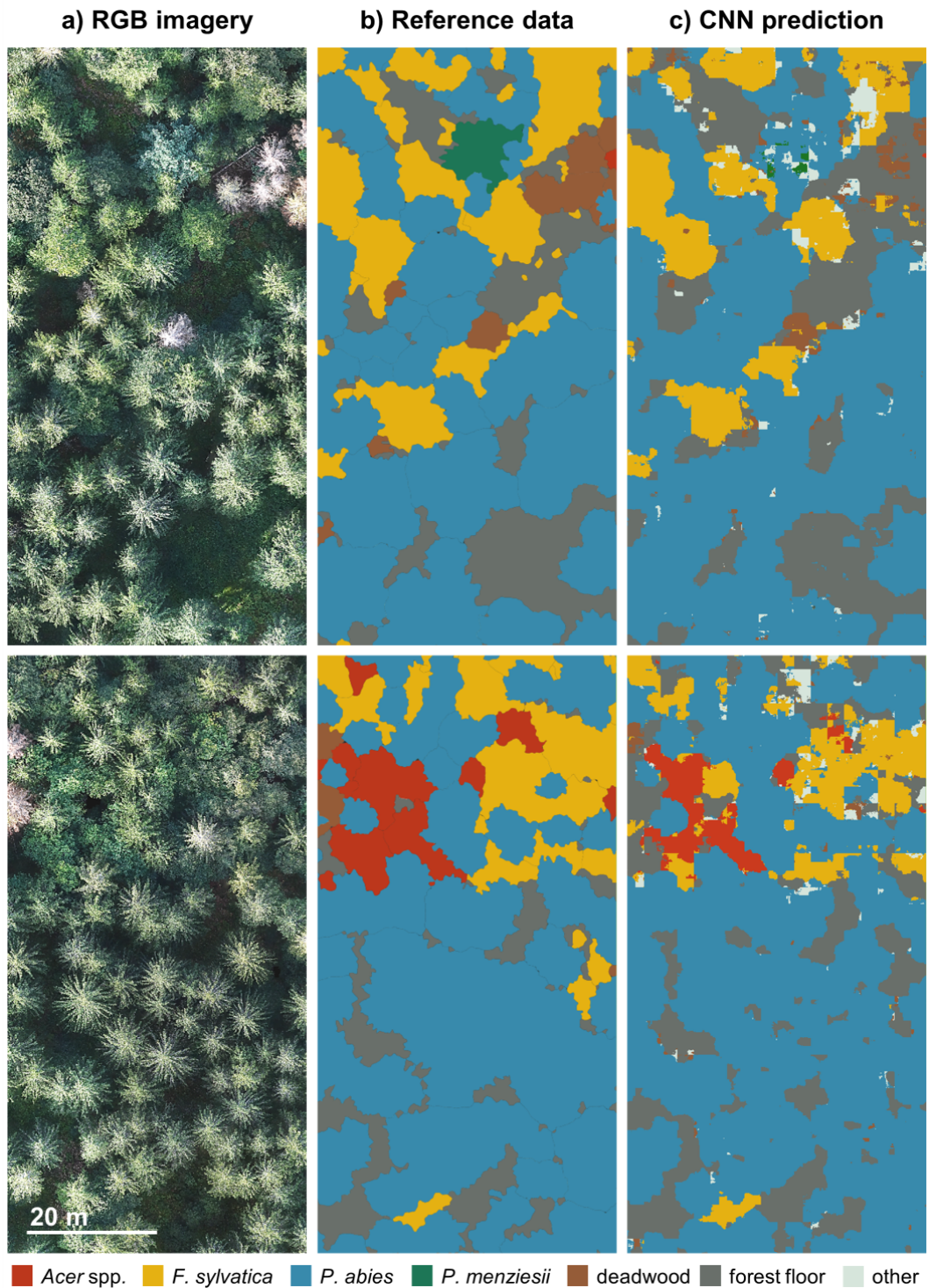


Figure 2.5: Predictions of a trained CNN on a 100×100 m plot. (a) UAV-based RGB orthomosaic, (b) manually delineated reference data, (c) CNN prediction based on 128×128 pixel tiles (RGB+nDSM). For illustrative purposes, the two sides of the plot are shown one above the other. Classes that did not appear in the reference data are grouped in the category “other”.

extracted tree crowns from UAV-based RGB imagery ($F_1 = 80\%$) (Natesan et al., 2019). However, a more detailed comparison of our results with the existing literature is hampered by the variety of applied CNN approaches (i.e., object detection, image classification/regression, and semantic segmentation), CNN architectures, forest types, and most of all the tree species studied.

2.4.2 TILE SIZE

For most of the classes, the tile size did not have a prominent effect on model performance. Only for underrepresented classes, a larger tile size was disadvantageous. This depended less on the tile size itself, but rather on the species coverage within the tiles. With smaller tiles, the area percentage of rare species on the tile was larger and underrepresented species thus contributed more to the model update during training. Whereas with larger tiles, underrepresented species got lost in the surrounding information of more frequent species. This was despite the use of weighted categorical cross entropy as loss function to compensate for such imbalances. The situation was different for classes that feature distinct characteristics (i.e., *L. decidua* and deadwood) as they were modelled equally well, regardless of the tile size. From the prediction map (Figure 2.5c) it becomes evident that the CNN, despite the employed moving window approach, suffered from edge effects, a known problem with CNNs. Obviously, this effect is more problematic with a smaller tile size. Hence, if sufficiently enough reference data for the targeted classes is available, a larger tile size should be preferred. This allows a larger spatial context to be considered—which is key information to CNNs—and speeds up model inference over large spatial extents. The fact that the models with smaller tile sizes reached their minimal validation loss earlier can be explained by the different batch sizes. The batch size is limited by the computational complexity of the CNN-architecture, the available RAM, and the size of the images. To analyse the influence of the batch size on the model performance is beyond the scope of this study. With the different batch sizes for the CNNs of the different tile sizes, we ensured that the models were exposed to the same amount of information in terms of area coverage.

2.4.3 CANOPY HEIGHT INFORMATION

Adding height information from nDSM to the CNN slightly increased the model accuracies for most of the classes. This contrasts with Sothe et al. (2020) and Hartling et al. (2019) who found additional height information to decrease the model performance. Kattenborn et al. (2020) found no clear positive effect of combining height information with RGB data and suggested that the structural aspect is redundant in both height and RGB information. Analogous to our visual perception of the tree crowns, we assume that the basic structural information

of nDSMs is already inherently included in RGB data through shadows and illumination differences. Whereas the creation of a digital surface model from UAV data is required for the calculation of the orthomosaic anyway, one should keep in mind that for the calculation of nDSMs a digital terrain model is needed (Wallace et al., 2019), which in turn requires additional processing steps. Furthermore, including additional layers to the CNN increases the number of parameters and thus computational complexity and could outweigh the benefit introduced.

2.4.4 SPATIAL RESOLUTION

Our results showed that very-high spatial resolution was essential for accurate mapping of forest tree species using RGB data. These findings underline the key role that UAVs can play for the remote sensing-based forest assessment, given that airborne and satellite remote sensing data currently do not provide a comparable spatial resolution. While most species with small shares of the dataset could not be identified with coarsening spatial resolution, deadwood could still be sufficiently identified, despite its small share of the dataset (0.95%). This is probably because the visual characteristics of deadwood were still represented at coarser spatial resolutions. This indicates that for some classes, mapping might be possible even at coarser spatial resolutions if prominent features exist. Accordingly, Safonova et al. (2019) used CNNs on UAV-based RGB imagery with 5–10 cm spatial resolution to detect damaged and dead trees of *Abies sibirica* after bark beetle infections with F1-scores up to 93%.

For a qualitative inspection of the effect of the spatial resolution and to obtain a causal explanation for our results, we inspected the learned features of the CNN based on filter visualizations (Figure 2.6). The latter are synthetic images that would maximally activate the respective filter of a trained network—in other words, they reflect what the network is looking for (technical details on the filter visualization are given in the Appendix A3). The filter visualizations of the fourth block and the centre block of the CNN revealed fine-scale patterns that resemble typical canopy features, e.g., conifer-like branching structures (Figure 2.6 a,c), or broad-leaf-like canopy structures (Figure 2.6 b,d). Such patterns could not be revealed with coarser spatial resolutions, which underlines our findings that a very high resolution is key to identifying forest tree species. It, therefore, seems possible that further increasing the spatial resolution (e.g., sub-centimetre) may even improve the capabilities for a CNN-based tree species mapping.

2.4.5 MODEL GENERALIZATION

The validation from the test dataset revealed high generalization abilities for the identification of 14 classes with a mean F1-score of 0.73 (128 × 128 pixel tiles,

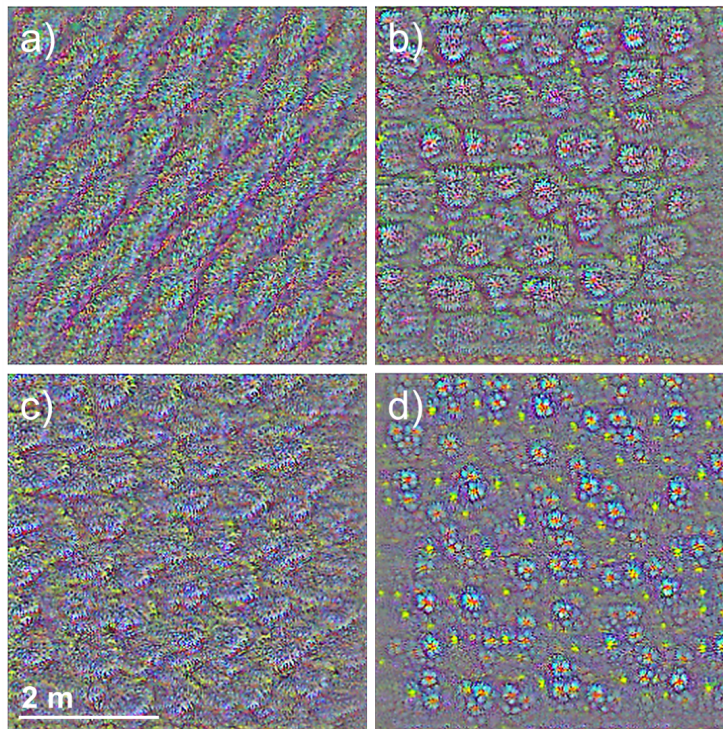


Figure 2.6: Selection of synthetic filter visualizations resembling patterns that would most stimulate the CNN (for technical details, see Appendix A3). The filter visualizations correspond to the dimensions of the tile size (here 256×256 pixel) and highlight the importance of fine-scale features.

RGB+nDSM) and evenly distributed site-specific F1-scores across all sites and years. Sothe et al. (2020) reported problems in generalizing the learned features of nine tree species when individual CNNs were trained locally on different sites. For the discrimination of two *Pinus* species from non-*Pinus*, Natesan et al. (2019) showed a higher F1-score (80%) when CNNs were trained with samples from several years than when trained with only one year (50%). Similarly, Weinstein et al. (2020) reported high generalization abilities of CNNs for the detection of individual trees over four different forest types. They found a CNN trained on all available forest types to outperform individual, locally trained CNNs. Their results suggest high model transferability when CNNs are trained over large and heterogeneous data. The data used in this study were collected in 51 one-hectare plots in two different forest types (temperate deciduous and mixed coniferous forests), different managements (managed and unmanaged), and study areas (Southern Black Forest and Hainich NP), and included a variety of growth stages. UAV data acquisition took place in the years 2017–2019 from June–September (day of the year 110–307) and covered a variety of illumination situations due to the different recording times from 7 am to 6 pm. In addition, data augmentation was

used to increase the size and variance of the training dataset, and to minimize spatial autocorrelation of adjacent tiles. We, therefore, assume that the high generalization abilities of the CNNs, as indicated by the overall accuracy, as well as the evenly distributed F1-scores across all sites, are the result of including many sites from different areas, different forest structures, different seasons and years, and varying illumination properties. This way, it can be ensured that the CNN learns features of tree species that are representative for different growth stages and site conditions. In line with Weinstein et al. (2020), we assume that more training data and increased heterogeneity will further enhance the accuracy and generalization of CNNs. Coupled with the establishment of large databases of remote sensing and reference data (Zhu et al., 2017), this opens the possibilities of transfer learning or even the creation of universal models. In the case of transfer learning, CNNs are pre-trained on large and heterogeneous datasets and the model weights are fine-tuned for the respective use case, while a universal model is trained on all existing data and is therefore transferable across sites. Weinstein et al. (2020) already demonstrated this future perspective for the detection of trees over various landscapes. Our results show a path for widely applicable mapping of tree species in temperate forests using only low-cost UAV-based RGB data and CNNs.

2.4.6 CNN ARCHITECTURE

Frequently applied approaches for mapping vegetation from remote sensing data using CNN comprise image classification/regression or object detection. Classification and regression approaches either rely on prior segmentation of the target (cf. Hartling et al., 2019; Natesan et al., 2019; Sothe et al., 2020), or predictions are assigned to an entire image tile (cf. Kattenborn et al., 2020; Qian et al., 2020; Rezaee et al., 2018). The output of the object detection task is typically a bounding box drawn around the object of interest (cf. Chen et al., 2019; Csillik et al., 2018; Fromm et al., 2019; Safonova et al., 2019; Santos et al., 2019; Weinstein et al., 2019, 2020). The capability of such approaches to derive spatially explicit maps can be limited by a number of reasons: (1) they require additional preprocessing steps (e.g., segmentation, background removal), or (2) classification on the single-pixel level is required to retrieve pixel-based predictions, or (3) the results represent object location and (rectangular) extent rather than spatially explicit objects. In contrast, semantic segmentation is an end-to-end learning approach that combines segmentation and classification in a pixel-based fashion at the original spatial resolution and is thus ideally suited for mapping tree species in forests. No prior segmentation or classification is necessary apart from the creation of a training samples.

In this study, we used the U-net architecture, given its good performance even with small amounts of labelled data (Ronneberger et al., 2015). Besides its relatively

low computational complexity, several studies have successfully demonstrated the suitability of the U-net for the mapping of single plant species (Kattenborn et al., 2019a; Wagner et al., 2020), individual trees (Freudenberg et al., 2019; Lobo Torres et al., 2020), forest damage and disturbance (Hamdi et al., 2019; Kislov & Korznikov, 2020; Wagner et al., 2019), forest types (Wagner et al., 2019), and plant communities (Kattenborn et al., 2019a). Since we were interested in the general applicability of CNNs for mapping forest tree species, we did not aim for benchmarking multiple architectures. Besides U-net, a variety of more elaborate model architectures for semantic segmentation exist (e.g., FC-DenseNet (Jégou et al., 2017), SegNet (Badrinarayanan et al., 2017), or DeepLabv3+ (Chen et al., 2017)). Lobo Torres et al. (2020) compared five models of varying complexity, namely U-net, FC DenseNet, SegNet, and two variants of the DeepLabv3+ for semantic segmentation of tree species in urban environments. Their results suggest the model accuracies of the architectures to be comparable, whereas more complex models (i.e., DeepLabv3+) required up to two or four times more time during model training and inference.

Another alternative to semantic segmentation is instance segmentation, i.e., segmenting not only classes but also individuals. Detecting individual trees would truly be of high value for forestry and conservation. However, from our experience from the visual interpretation, many tree crowns of the same species are hard to differentiate because branches may have crown-like characteristics (e.g., *F. sylvatica*, *F. excelsior*). This suggests that generating labels for the segmentation of individuals requires more sophisticated procedures that either require *in-situ* data with high-quality GNSS data on tree stem locations or a sophisticated link to ancillary remote sensing data (e.g., lidar data) to aid visual inspection. However, even if labels were available, we doubt that instance segmentation algorithms would be able to locate individuals in RGB orthomosaics given the above-described difficulties.

2.4.7 REFERENCE DATA

Reference data were derived through manual delineation in the orthomosaics after visual interpretation. Given the very high spatial resolution (<1.35 cm) of the imagery, tree species were clearly identifiable. To minimize errors in the visual interpretation, we used additional information from forest inventories (i.e., tree height, DBH, and partly tree stem coordinates), cross-checked the delineations by at least one other interpreter, and removed tree crowns that we could not identify with certainty. Several reasons suggest that when using very high-resolution image data, no other method is appropriate for obtaining reference data, especially in the case of deep learning: (1) the acquisition of *in-situ* data of the required amount is costly, time- and labor-intensive and might thus not be feasible; (2) the reference data from visual interpretation of the image data is not subject

to geolocation errors of GNSS-measurements as for *in-situ* measurements. Such errors are typically in the range of decimetres to meters when using differential GNSS and might even exceed several meters when using stand-alone GNSS, particularly under dense canopies (Kaartinen et al., 2015; Valbuena et al., 2010). Especially when using very high-resolution imagery, errors might exceed the spatial resolution by far, which makes *in-situ* measurements difficult to use; (3) *in-situ* data that can be recorded with the least effort in forests are typically point observations (e.g., tree stem coordinates) that do not necessarily allow for a spatially explicit link with the targeted variable (e.g., tree crowns). However, visual interpretation from RGB imagery is not free of misinterpretation, but due to the high amount of reference data required for CNNs and the need for high-precision geolocation within the high-resolution imagery, it seems to be the most effective way of collecting reference data. Furthermore, it has been shown that CNNs can compensate for faulty labels to some extent and that correct classes were predicted despite incorrectly labelled reference data (Hamdi et al., 2019; Kattenborn et al., 2020).

A probable reason for the decreasing accuracy with decreasing share of the species might be that less abundant species share similar features with more abundant species and are therefore misclassified. This could be the case especially with *F. sylvatica* and *C. betulus* whose leaves have a similar size and shape. On the other hand, rarely occurring species that show no or less similarities with more abundant species (e.g., small leaves and distinct habitus of *B. pendula*) have also been poorly classified, most likely due to their under-representation in the data set. The majority of observations in this study were situated along a gradient of forest connectivity and structure (Storch et al., 2020) and, hence, not optimized for representing all species for a remote sensing application. Thus, designing or updating a database towards sufficient observations for rare taxa, may be key for an accurate species mapping.

More technical alternatives for improving the accuracy for underrepresented species include tuning the weights in the loss function and setting them higher for less frequent classes (which in our case, however, rather worsened the results at some point), weight updating (i.e., updating the weights of an already trained CNN using solely data of less frequent species), or sampling tiles containing less frequent species more often during model training. The latter, however, was not an option due to the large range of occurrences in our dataset (0.2–33% area-related share), as it would have drastically reduced the dataset size or assumedly would have introduced large redundancies.

For the genera *Acer*, *Tilia*, and *Quercus*, we grouped the respective species into genus-level classes, since they were only present in very small quantities in the plots. While for some of these species a distinction in the RGB data might be easier due to visible differences in tree habitus or leaf shape (e.g., *Acer platanoides* and *Acer pseudoplatanus*), for other species with only subtle differences it might

be very difficult or even impossible (e.g., *Quercus petraea* and *Quercus robur*). The mapping of such species using very high-resolution UAV-based RGB data and CNNs could prove to be very difficult and should be subject to further research.

2.5 CONCLUSION

We showed that RGB imagery from consumer-grade UAVs in concert with a CNN-based semantic segmentation enables to map tree species across heterogeneous temperate forests stands with high accuracies. We tested CNN-based tree species mapping with different tile sizes, incorporation of height information (nDSM), and varying spatial resolutions. The tile size had no prominent influence on the model accuracy if enough reference data was available. By choosing a larger tile size, a larger spatial context was considered by the CNN, thereby minimizing edge effects, and accelerating the application over a large spatial extent. Additional height information from nDSMs slightly increased the model accuracy. Still, the inclusion of nDSMs should be carefully considered, since the increased computational complexity of the CNN and the need for a digital terrain model are major drawbacks. A high spatial resolution was indeed decisive for the accurate mapping of forest tree species using RGB data. Overall, our results showed that CNN models generalize well over the diverse dataset in terms of site conditions, forest types, stand structure, phenology, and illumination properties.

Our findings underline the synergies between high-resolution UAV imagery and CNN-based segmentation procedures. In view of the increasingly easy and affordable way to obtain very high-resolution RGB imagery with consumer-grade UAVs, and given that air- and spaceborne data currently do not provide comparable spatial resolutions, UAVs can play a crucial role in the mapping of forest tree species. CNN are able to learn species-specific features from such high-resolution imagery, while their end-to-end learning capabilities make extensive preprocessing of remote sensing data obsolete and simplify a widespread application. Our study demonstrates the potential of a concerted use of UAVs and CNNs and thus provides promising future perspectives for applications in forestry or large-scale and long-term ecological research. Such applications usually require large-scale and accurate maps of forest tree species, for which field-based methods might be too labor-intensive while commonly used machine learning approaches might not be accurate enough.

Given that training data generation for semantic segmentation is a laborious task and generalization across forest types is of primary concern, a flexible, widespread, and operational application of such an approach may be facilitated by incorporating transfer learning (i.e., updating and refining the learned feature representations of an already trained CNN by retraining the model with new

image data) or the development of universal models (i.e., one single model that has been trained over a variety of landscapes and many species).

DECLARATION OF COMPETING INTEREST

The authors declare that they have no known competing financial interests or personal relationships that could have appeared to influence the work reported in this paper.

ACKNOWLEDGMENTS

We thank the public forest authorities involved for facilitating this research and the State Agency for Spatial Information and Rural Development of Baden-Württemberg (LGL) for the provisioning of data. We thank the administration of the Hainich National Park for the opportunity for research within the National Park and the Biodiversity Exploratories project (German Research Foundation–DFG Priority Program 1374 "Infrastructure-Biodiversity-Exploratories") for their cooperation, support, and provision of data. We want to especially thank Johannes Penner from the ConFoBi coordination team and Andrey Lessa for the provision of the forest inventory data for the black forest region. Many thanks to Kathrin Wagner and Benjamin Stöckigt for their aid in UAV image acquisition and Johannes Hoffmann and Timo Schmid for the assistance in visual image interpretation. The study has been funded by the German Aerospace Centre (DLR) on behalf of the Federal Ministry of Economics and Technology (BMWi), FKZ 50EE1909A. The data acquisition within the black forest was founded by the German Research Foundation DFG (GRK 2123).

3

Chapter 3

UAV-BASED REFERENCE DATA FOR THE PREDICTION OF FRACTIONAL COVER OF STANDING DEADWOOD FROM SENTINEL TIME SERIES

This chapter has been published as: Schiefer, F., Schmidlein, S., Frick, A., Frey, J., Klinke, R., Zielewska-Büttner, K., Junttila, S., Uhl, A., & Kattenborn, T. (2023a). UAV-based reference data for the prediction of fractional cover of standing deadwood from Sentinel time series. *ISPRS Open Journal of Photogrammetry and Remote Sensing*, 8, 100034. <https://doi.org/10.1016/j.ophoto.2023.100034>

ABSTRACT

Increasing tree mortality due to climate change has been observed globally. Remote sensing is a suitable means for detecting tree mortality and has been proven effective for the assessment of abrupt and large-scale stand-replacing disturbances, such as those caused by windthrow, clear-cut harvesting, or wildfire. Non-stand replacing tree mortality events (e.g., due to drought) are more difficult to detect with satellite data—especially across regions and forest types. A common limitation for this is the availability of spatially explicit reference data. To address this issue, we propose an automated generation of reference data using uncrewed aerial vehicles (UAVs) and deep learning-based pattern recognition. In this study, we used convolutional neural networks (CNNs) to semantically segment crowns of standing dead trees from 176 UAV-based very high-resolution (<4 cm) RGB-orthomosaics that we acquired over six regions in Germany and Finland between 2017 and 2021. The local-level CNN-predictions were then extrapolated to landscape-level using Sentinel-1 (i.e., backscatter and interferometric coherence), Sentinel-2 time series, and long short-term memory networks (LSTMs) to predict the cover fraction of standing deadwood per Sentinel-pixel. The CNN-based segmentation of standing deadwood from UAV imagery was accurate (F1-score = 0.85) and consistent across the different study sites and years. Best results for the LSTM-based extrapolation of fractional cover of standing deadwood using Sentinel-1 and -2 time series were achieved using all available Sentinel-1 and -2 bands, kNDVI, and NDWI (Pearson's $r = 0.66$, total least squares regression slope = 1.58). The landscape-level predictions showed high spatial detail and were transferable across regions and years. Our results highlight the effectiveness of deep learning-based algorithms for an automated and rapid generation of reference data for large areas using UAV imagery. Potential for improving the presented upscaling approach was found particularly in ensuring the spatial and temporal consistency of the two data sources (e.g., co-registration of very high-resolution UAV data and medium resolution satellite data). The increasing availability of publicly available UAV imagery on sharing platforms combined with automated and transferable deep learning-based mapping algorithms will further increase the potential of such multiscale approaches.

3.1 INTRODUCTION

Tree mortality has immense consequences for forestry, environmental protection, and ecosystem services, and it is increasing globally due to changes in climate and related extreme events (Allen et al., 2010; Hartmann et al., 2022). For instance, in Europe recent excess rates of tree mortality could be related to intense drought events in the years 2018 and 2019 (Bastos et al., 2021; Senf et al., 2020, 2021). Still, the mechanisms and factors explaining excess rates of tree mortality are not fully understood (Hartmann et al., 2018b). For instance, tree mortality varies widely depending on tree species composition, forest management, and site conditions. Furthermore, drivers of tree mortality, such as climate extremes, have complex spatial and temporal patterns. They may even act in compound events, such as consecutive drought years, late spring frosts, and subsequent insect and pathogen outbreaks (Hartmann et al., 2018b; Huang et al., 2020; Zscheischler et al., 2020). To understand recent excess rates of tree mortality or to develop methods to forecast such events in the future, we need spatially and temporally continuous information on tree mortality (Hartmann et al., 2022). However, detecting and quantifying tree mortality over large spatial and temporal scales remains challenging.

Remote sensing is being successfully applied for the detection of abrupt and large-scale stand replacing disturbances, such as those caused by windthrow, wildfire, or clear-cut harvesting, to be feasible at regional and global scales at a 30 m spatial resolution (Hansen et al., 2013; Senf & Seidl, 2021; White et al., 2017). Less focus has been given to non-stand replacing disturbances, where tree mortality occurs more subtle and scattered across landscapes, affecting only individual trees or smaller groups. For example, this type of disturbance dynamics can be triggered by drought or insects (Coops et al., 2020), particularly in the initial phase of disturbance. Such patterns are critical to our understanding of tree mortality dynamics, but cannot be accurately detected at 30 m spatial resolution (Frolking et al., 2009; Senf et al., 2021; Trumbore et al., 2015).

Various studies have demonstrated the potential of higher spatial resolution satellite data (Liu et al., 2021) or aerial (ortho-)images (Chiang et al., 2020; Fricker et al., 2019; Jiang et al., 2019; Meddens et al., 2011; Monahan et al., 2022; Sylvain et al., 2019; Zielewska-Büttner et al., 2020) to explicitly detect tree mortality. However, such datasets are usually limited to small extents, are expensive to acquire, and are often only acquired sporadically, which limits the spatially and temporally systematic detection of deadwood. Other studies have attempted to compensate for the coarse resolution of Earth observation satellites by using spectral information to indirectly track tree mortality. For example, tree mortality was approximated from relative changes of spectral indices (Bárta et al., 2021; Thonfeld et al., 2022) or biochemical and biophysical traits obtained from radiative transfer models (Ali et al., 2021). However, such spectral indices or traits also

vary depending on a number of factors unrelated to tree mortality (e.g., species composition, forest structure), but in a confounding way (Frolking et al., 2009; Glenn et al., 2008; Xue & Su, 2017). Such approaches can only provide indirect information on tree mortality, and therefore do not explicitly indicate whether tree crowns are dead or not.

Explicit detection and quantification of tree mortality, for instance in terms of cover of dead tree crowns per area, requires spatially explicit reference data for model calibration and validation. However, such reference datasets are scarce and costly to obtain, and are therefore one of the most limiting factors for conducting large-scale remote sensing analyses for deadwood detection (Frolking et al., 2009; McDowell et al., 2015; Schuldt et al., 2020; Trumbore et al., 2015). Moreover, existing *in situ* reference datasets, such as those from national forest inventories, are not explicitly designed to study or quantify tree mortality, and often do not provide an estimate of canopy cover, which limits their usability for remote sensing approaches. Several authors have highlighted this lack of ground reference data and emphasized the need for global reference databases on tree mortality following standardized protocols (Allen et al., 2010; Buras et al., 2020; McDowell et al., 2015; Schuldt et al., 2020). Initiatives such as the International Tree Mortality Network are compiling harmonized global datasets on field-based research plots to study tree mortality (Hammond et al., 2022). But even with a well curated dataset of global coverage, the integration of ground-based reference data with Earth observation satellite data is challenging: Pixel sizes of suitable Earth observation satellite missions, such as Landsat or Sentinel, do not enable to resolve individual trees and, hence, hamper the link with ground reference observations. In addition, properties typically measured on the ground (e.g., tree stem coordinates) do not necessarily allow for a spatially explicit link to what satellites ‘see’ from a *bird’s-eye* perspective (e.g., tree canopy reflectance) (Pause et al., 2016; Schiefer et al., 2020). Moreover, dense canopy cover or complex topography can considerably limit GNSS accuracies of ground measurements, making reliable geopositioning in the field even more difficult (Kaartinen et al., 2015; Valbuena et al., 2010). Overall, both the quality and quantity of common reference data do not facilitate the mapping of tree mortality at large spatial scales with Earth observation data.

These practical limitations and the general scarcity of ground reference data on tree mortality may be compensated by uncrewed aerial vehicles (UAVs, Alvarez-Vanhard et al., 2021; Kattenborn et al., 2019b; Liu et al., 2021; Schiefer et al., 2020). The very-high spatial resolution of UAV RGB imagery enables precise segmentation of dead tree crowns, and the flexible deployment of UAVs further enables efficient detection of tree mortality events over large and even inaccessible areas. Especially in combination with recent advances in pattern recognition and deep learning, such as convolutional neural networks (CNNs), very accurate results for crown segmentation of standing dead trees have been demonstrated (Chiang et al., 2020; Sani-Mohammed et al., 2022; Schiefer et al., 2020). Because

such predictions also emerge from the bird's-eye perspective, they may be readily used for subsequent satellite-based and thus large-scale analyses (Kattenborn et al., 2019b). The concerted use of UAVs and CNNs and their efficiency enable the generation of ample amounts of reference data over large areas and multiple years. This may greatly facilitate the training of robust satellite-based models that are transferable across temporal, spatial, or environmental conditions. Hence, to compensate for the lack of ground reference data on tree mortality, we propose an upscaling approach in which fine-scaled patterns in UAV imagery are harnessed to create ample reference data at local scales for training models that predict standing deadwood at the landscape-scale using multitemporal and multispectral information of satellite data. In doing so, we seek to answer the following research questions: **(1)** Are CNN-based predictions of standing deadwood from UAV imagery robust across a wide range of forest stand characteristics and over multiple years? **(2)** Can these CNN-based predictions from UAV imagery serve as reference data to accurately predict fractional cover of standing deadwood with Sentinel imagery at 10 m spatial resolution? **(3)** Is this upscaling approach transferable across regions and different years?

3.2 MATERIAL AND METHODS

The workflow of this study consisted of a local-level and a landscape-level part (Figure 3.1). In the local-level part, we tested the combination of UAV RGB imagery and CNN-based pattern recognition for an automated extraction of standing dead tree crowns. We then upscaled these UAV-based segmentations of standing dead trees to fractional cover at the landscape-level using satellite-based time series analysis. For this upscaling, we used Sentinel-1 and Sentinel-2 time series together with a long short-term memory network (LSTM).

3.2.1 STUDY AREA AND UAV DATA ACQUISITION

This study comprised a set of UAV data acquisitions from the six study regions Southern Black Forest, Northern Black Forest, Dresden Heath, Karlsruhe-Bretten, and Hainich National Park in Germany, as well as Helsinki, Finland (Figure 3.2). The sites comprise a large heterogeneity in terms of species composition and forest structure, which results from different environments and forest management (see site information in Table 3.1). In total, we acquired orthoimages over 176 sites across the six regions. For each site, we acquired UAV-based RGB-photographs and derived orthomosaics using Structure-from-Motion (SfM) photogrammetric processing chains (details see e.g. Schiefer et al., 2020). The UAV orthoimagery was acquired with different UAV platforms, camera systems, flight planning

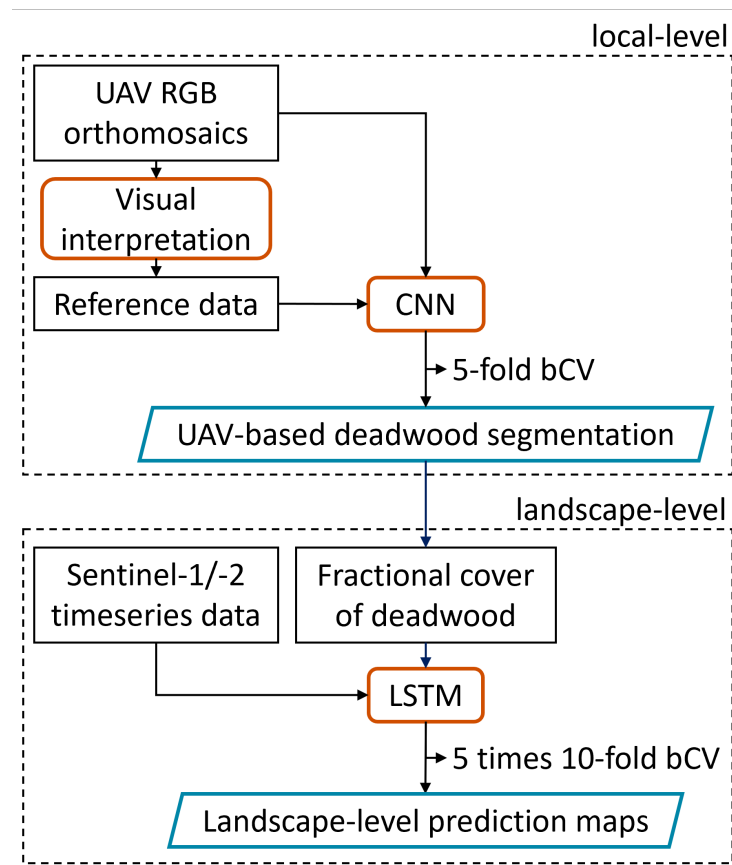


Figure 3.1: Schematic workflow of the upscaling approach. CNN-based deadwood segmentation from UAV RGB orthomosaics (local-level) are upscaled to fractional cover of standing deadwood using Sentinel-1/-2 time series data and an LSTM model (landscape-level). bCV: block cross-validation.

software, acquisition settings, and photogrammetric workflows for orthoimage generation (an overview of the different settings for each dataset is given in Table 3.1). The orthoimagery covered a total area of 727.33 ha and the spatial extent of the individual orthomosaics ranged from 1.29 to 32.72 ha. The ground sampling distance (GSD) ranged from 0.60 to 3.39 cm and was resampled to a common pixel size of 4 cm.

3.2.2 CNN-BASED SEGMENTATION OF STANDING DEADWOOD AT LOCAL LEVEL

For mapping dead trees at the local level, we choose a semantic segmentation approach that allows to predict dead tree crowns at the original pixel-size of the UAV imagery. The training of common CNN segmentation models requires

Table 3.1: Summary of the regions, sites, and the corresponding UAV acquisitions.

Study region	Site information			UAV data			
	Number of sites n = 176	Forest type (management)	Dominant tree species	UAV system (camera)	GSD [cm]	covered area [ha]	year(s) of acquisition
Southern Black Forest	141	mixed and coniferous (managed for timber production)	<i>Picea abies</i> L.,	HiSystems MK	0.65-3.12	375.13	2017-2021
			<i>Fagus sylvatica</i> L., <i>Abies alba</i> Mill.	Okto-XL (Sony Alpha 7R)			
Northern Black Forest	14	mixed and coniferous (managed for timber production; unmanaged)	<i>Picea abies</i> ,	DJI Phantom	1.08-2.68	169.00	2019, 2021
			<i>Abies alba</i> , <i>Fagus sylvatica</i>	4 Pro (FC6310S)			
Dresden Heath	8	mixed and coniferous (managed for timber production)	<i>Picea abies</i> ,	DJI Phantom	1.92-2.60	46.41	2021
			<i>Fagus sylvatica</i> ,	4 Pro			
			<i>Quercus spec.</i> ,	(FC6310S)			
			<i>Betula pendula</i> (Roth)				
Karlsruhe-Bretten	6	mixed (managed for timber production)	<i>Pinus sylvestris</i> L.,	HiSystems MK	1.62-2.76	37.57	2019
			<i>Quercus rubra</i> L.,	Okto-XL			
			<i>Carpinus betulus</i> L.,	(Canon 100D)			
			<i>Fagus sylvatica</i>				
Hainich National Park	4	mixed deciduous (unmanaged)	<i>Fagus sylvatica</i>	DJI Phantom	0.80-1.35	8.58	2019
				4 Pro (FC6310S)			
Helsinki	3	mixed and coniferous (managed for path safety)	<i>Picea abies</i> ,	DJI Phantom	2.97-3.39	90.63	2020
			<i>Pinus sylvestris</i> ,	4 Pro			
			<i>Betula pendula</i> ,	(FC6310S)			
			<i>Populus tremula</i> L.				

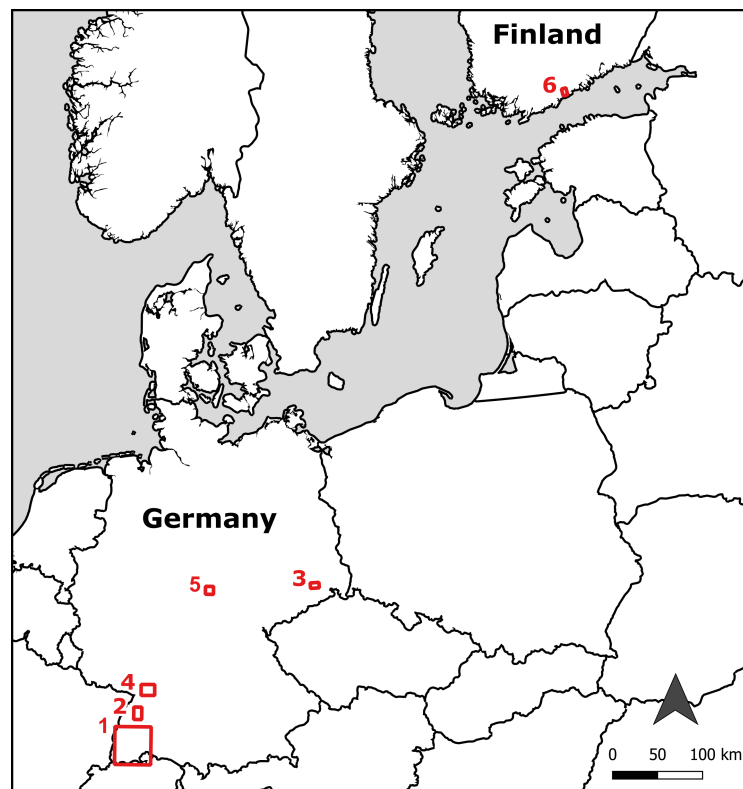


Figure 3.2: The six study regions: (1) Southern Black Forest, (2) Black Forest, (3) Dresden Heath, (4) Karlsruhe-Bretten, (5) Hainich National Park, and (6) Helsinki.

image data that is fully labelled in form of masks. We prepared binary masks (absence/presence of dead tree crowns) by delineating standing dead trees from all the available orthomosaics using visual interpretation in ArcGIS v.10.6.1 (ESRI, Redlands, USA). Labelling all sites is not a requirement of the CNN approach, but is necessary to obtain a comprehensive picture of the model performance across sites and years. We delineated trees and branches that were clearly identifiable as dead, as indicated by degraded, discoloured, or entirely absent foliage. Trees that were damaged but still had green foliage (e.g., green attack after bark beetle infestation) were not included, which facilitates visual interpretation and ensures its robustness.

For the CNN model training, we cropped the orthomosaics and the corresponding masks into 40 451 non-overlapping tiles of 256×256 pixels (edge length of 10.24 m). We used the U-net CNN architecture (Ronneberger et al., 2015) to automatically segment standing dead trees in the orthomosaics. The U-net features an encoding path to capture spatial features and their context, and a decoding path to map the resembled information to the original image dimensions. Here, we used five blocks in the encoding path, each consisting of two 3×3 convolutions,

followed by batch normalization, a linear rectifier unit activation, and 2×2 max pooling operation with a striding of two. In these blocks, the convolutional layers had a depth of 1024, 512, 256, 128, and 64 layers for the encoder path and the same but in reverse order for the decoder path. A detailed description of the utilized U-net architecture can be found in (Schiefer et al., 2020). Here, we used a sigmoid activation in the final layer. The CNN was trained with a batch size of 32 tiles over 60 epochs using binary cross entropy loss and RMSprop optimizer with a learning rate of $1e-4$. For model regularization, we augmented the training tiles using random horizontal and vertical flips and random changes in image brightness (90–110%), contrast (80–120%), and saturation (80–120%), thereby increasing the size of the training dataset to twice its size.

To avoid biased model performance estimates due to spatial dependence between training and test data, we assessed the CNN model performance using five-fold spatial block cross-validation (Kattenborn et al., 2022). We randomly split the image tiles from the study sites ($n = 176$) into five folds, thereby ensuring, that from each of the six study regions, at least one site was included. In each step, the sites from one fold served as an independent test set, and the sites from the remaining four folds were split into 80% training and 20% validation set. Using the independent test set, the final model performance was assessed on a per-pixel level based on precision, recall, and F1 score (the harmonic mean of the first two).

3.2.3 MAPPING DEADWOOD COVER FRACTIONS AT LANDSCAPE LEVEL USING SATELLITE TIME SERIES

3.2.3.1 *Satellite time series*

For the extrapolation to landscape-level using satellite data and LSTM, we used the CNN-based segmentations (not the manually created masks) from high-resolution UAV imagery and calculated the fractional cover (%) of standing deadwood per Sentinel grid cell using a superimposed Sentinel-2 pixel grid (10 m resolution). Summary statistics for all sites are given in Appendix A5. To map the fractional cover of standing dead trees at the landscape level, we extracted time series from Sentinel-1 and Sentinel-2 images acquired between 1st October 2015 and 30th September 2021. For Sentinel-2, we used the Level-2A product that provides atmospheric- and terrain-corrected Bottom Of Atmosphere (BOA) reflectance images (Main-Knorn et al., 2017). We selected bands with 10 m GSD (i.e., B2 blue, B3 green, B4 red, and B8 near infrared), 20 m GSD (i.e., B5–B7 red edge, and B11–B12 short-wavelength infrared), and two with 60 m GSD (i.e., B1 aerosols and B9 water vapor). In addition to the spectral bands, we calculated the kernel normalized difference vegetation index (kNDVI, Camps-Valls et al., 2021) using the red (B4) and near infrared (B8) bands, and normalized difference water index (NDWI, Gao, 1996) using the narrow near infrared (B8A) and short wave infrared

(B11) bands. Pixel values with $kNDVI < 0.1$ were masked out from the Sentinel-2 bands, as they primarily represent atmospheric water and clouds.

For Sentinel-1, we selected Level-1 ground range detected (GRD) and single look complex (SLC) data from interferometric wide swath mode (IW) in dual polarization of type VV+VH. We used the Copernicus analysis ready data (CARD) processors that provide terrain-corrected backscatter (CARD-BS) and interferometric coherence (CARD-COH6) data. The CARD-BS processor consists of application of orbit file, removal of border and thermal noise, radiometric calibration, and terrain correction. The CARD-COH6 processor consists of application of orbit file, TOPSAR split, back-geocoding, coherence, TOPSAR deburst, TOPSAR merge, multilooking, and terrain correction. For terrain correction, the Copernicus DEM 30 m elevation data was used.

For both Sentinel-1 and -2, all spectral bands were resampled to 10 m spatial resolution using nearest-neighbour interpolation. We linearly interpolated missing values and converted the time series to 7-day intervals using arithmetic mean. Non-forested areas according to the Sentinel-2 Global Land Cover (S2GLC) map (Malinowski et al., 2020) were excluded from further analysis. All satellite images were accessed and preprocessed using Copernicus data and information access services (DIAS) via the CREODIAS platform (CloudFerro, Warsaw, Poland).

3.2.3.2 LSTM modelling

We used a long short-term memory network (LSTM) to predict fractional cover of standing deadwood based on the Sentinel-1 and Sentinel-2 time series. As a baseline to the deep learning method, we trained random forest models (Breiman, 2001), but these models performed worse (see Appendix A4). LSTM is a special kind of recurrent neural network (RNN) capable of learning long-term dependencies from sequences of data without suffering from the vanishing or exploding gradient problem that can occur when training RNNs (Hochreiter & Schmidhuber, 1997). LSTM units take temporal dependencies into account by controlling the network memory (or memory cell) using three sigmoid gate units (σ): a forget gate, an input gate, and an output gate (Figure 3.3). Depending on the output of the previous cell (h_{t-1}) and the current input (x_t) the forget gate controls whether the previous memory cell state (C_{t-1}) will be kept by means of a sigmoid function. The input gate, similarly, controls which part of the memory cell will be updated using a sigmoid function, combined with a \tanh function that creates weights that are then used to update the new cell state (C_t). Finally, the output (h_t) is determined by the output gate that decides which information of the cell state will be forwarded by means of a *sigmoid* function and a *tanh* function that scales the output between -1 and 1. Using a bidirectional implementation of LSTM, the network trains in both time directions, thereby learning temporal dependencies from past and future time steps (Schuster & Paliwal, 1997). We used two bidirec-

tional LSTM layers of 100 LSTM units each, followed by a fully connected layer and a sigmoid activation that predicts the final class probabilities

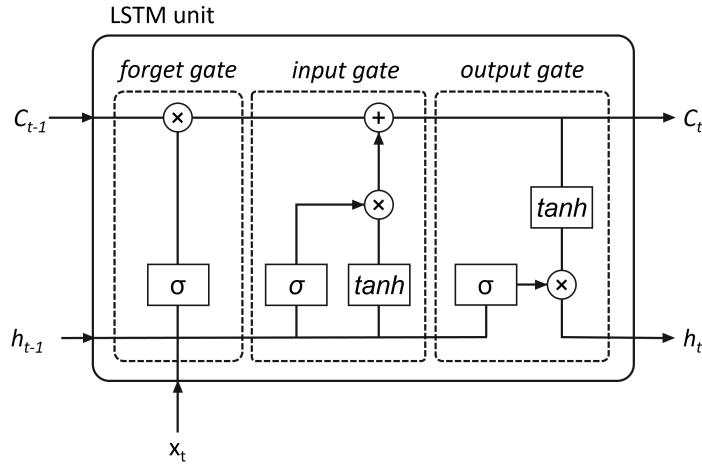


Figure 3.3: Structure of an LSTM unit

We tested four different input band sets to the LSTM, namely only Sentinel-2 (S2), Sentinel-1 and Sentinel-2 (S1+S2), Sentinel-2 and vegetation indices (S2+VI) and the combination of all available data (S1+S2+VI). We assessed the predictive performance of the LSTM models using a five times repeated ten-fold spatial block cross-validation. Here, the blocks were corresponding to the individual sites (an area covered by an individual orthomosaic). In each repetition, we randomly split the data on a site-basis ($n = 176$) into ten folds. In each cross-validation step, data from one fold served as independent test data and data from the remaining nine folds were split into 80% training and 20% validation data. Every LSTM model was trained for 150 epochs with a batch size of 64 using Adam optimizer. A subset ($n = 6\,300$) we sampled from the entire dataset to ensure a balanced distribution of fractional coverage values (0–100%). Because the spectral signal of bare ground can be similar to that of dead tree canopies, we added such observations (i.e., open forest floor and sparsely vegetated areas) delineated from national aerial surveys to avoid misclassification (a total area of approximately 10.14 ha).

To further validate the upscaling from high-resolution UAV imagery to satellite time series, we compared the LSTM predictions with fractional cover values obtained from an aerial orthophoto (GSD = 20 cm) for the Saxon Switzerland National Park, which was not part of model training and validation. Therefore, we semi-automatically classified the standing deadwood in the orthophoto (i.e., red-green band ratio, thresholding, manual refinement), calculated the fractional cover of standing deadwood with the superimposed Sentinel-2 grid, and compared it with the LSTM predictions. All analyses were conducted in R language (R

Core Team, 2022) and the code is available at <https://github.com/FelixSchiefer/TreeMortality>. Landscape-level prediction maps for Germany are available at <https://doi.org/10.5445/IR/1000155244> and will be continuously expanded.

3.3 RESULTS

3.3.1 CNN-BASED DEADWOOD SEGMENTATION IN UAV-ORTHOMOSAICS (LOCAL LEVEL)

The CNN-based segmentation of standing deadwood in the UAV imagery was very accurate with precision = 0.9, recall = 0.82, and F1-score = 0.85 derived from the five-fold block cross-validation (Figure 3.4a). Model performance was relatively consistent across all study sites, as shown by the median F1-score of 0.82 (interquartile range: IQR = 0.15) (Figure 3.4b). Model performance was also con-

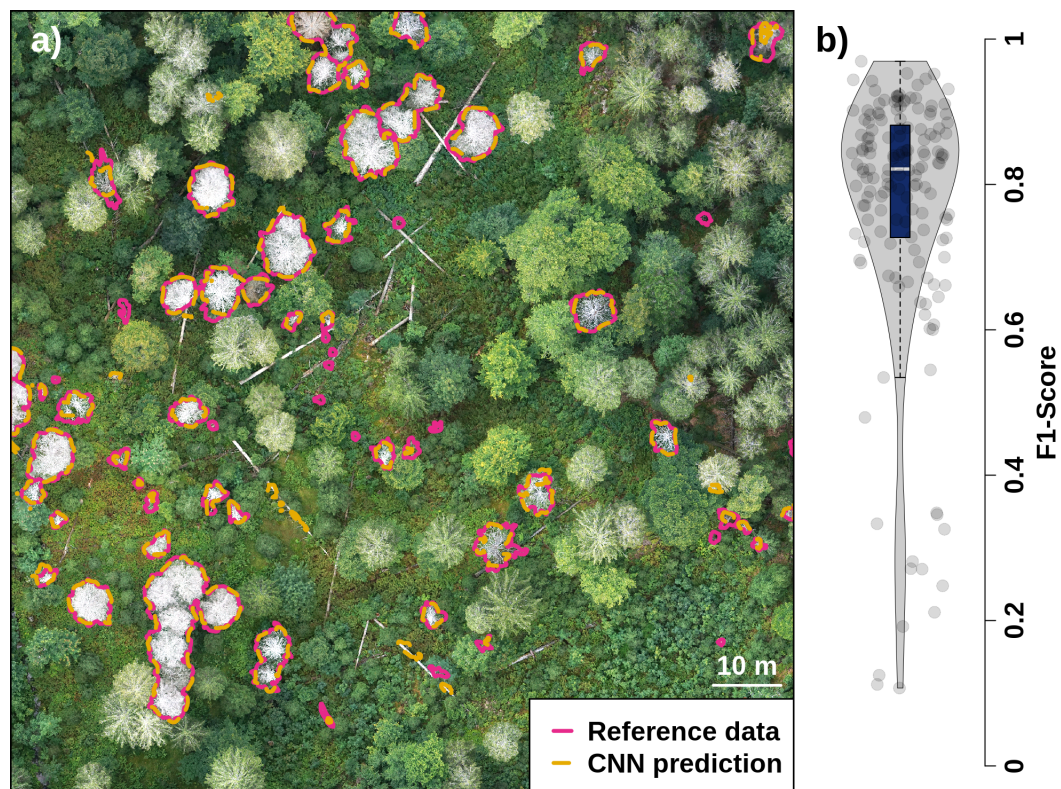


Figure 3.4: a) Illustration of the CNN model performance for the semantic segmentation of standing deadwood in CNN orthoimagery for a Southern Black Forest site. (Coordinate reference system: WGS84 UTM zone 32N, EPSG:32632). b) Distribution of F1-score values across study sites from the five-fold block cross-validation.

sistent across different years, with median F_1 -scores of 2017: 0.79 (IQR = 0.20, $n = 56$), 2018: 0.66 (IQR = 0.30, $n = 5$), 2019: 0.82 (IQR = 0.16, $n = 60$), 2020: 0.81 (IQR = 0.15, $n = 35$), and 2021: 0.87 (IQR = 0.07, $n = 20$). The median F_1 -scores per study region were Southern Black Forest: 0.82 (IQR = 0.15), Northern Black Forest: 0.87 (IQR = 0.07), Dresden Heath: 0.87 (IQR = 0.08), Karlsruhe-Bretten: 0.61 (IQR = 0.16), Hainich National Park: 0.11 (IQR = 0), and Helsinki: 0.78 (IQR = 0.04) (see Appendix A5 for site-specific values). Low F_1 -scores for standing deadwood were mainly observed at sites with very low area-related proportions of standing deadwood and at sites where the UAV acquisition was very late in the growing season (e.g., Hainich National Park). For the latter, deciduous trees that had already shed some of their foliage were partly misclassified as standing deadwood. Low F_1 -scores together with low precision, but high recall were observed for sites where there were many dead branches on the forest floor after very recent logging, which could easily be mistaken for standing deadwood.

3.3.2 MAPPING FRACTIONAL COVER OF STANDING DEADWOOD FROM SENTINEL TIME SERIES USING LSTM (LANDSCAPE LEVEL)

Figure 3.5 shows the Pearson's correlation coefficient (r) and the slope value of the total least squares (TLS) regressions for the different input band sets to the LSTM models. The highest median r -value (0.62) was observed for the S_2+VI input band set with 12 Sentinel-2 bands from the five times repeated ten-fold block cross-validation. Total least squares regression slope values closest to 1 were observed for the S_1+S_2+VI input band set, but with all available Sentinel-2 bands (median slope = 1.56). In general, additional information from Sentinel-1 alone (i.e., backscatter and interferometric coherence) reduced model performance compared to the models using only Sentinel-2 data. Contrary, model performance increased when vegetation indices (i.e., $kNDVI$ and $NDWI$) were added to the Sentinel-2 data. Using all available input band sets especially improved the regression slope values. LSTM model performance increased with more spectral information from the 20 m Sentinel-2 bands (i.e., 10 bands) and even more with the 20 m and 60 m Sentinel-2 bands (i.e., 12 bands).

Based on the TLS slope value closest to 1 (slope = 1.58, Pearson's $r = 0.66$), the LSTM model with the S_1+S_2+VI and 12 Sentinel-2 bands input band set was selected for landscape-level predictions (Figure 3.6). Uncertainties in the predictions were evenly distributed across the entire value range (Figure 3.6), except for observed values close to 0 and 1, where we observed overpredictions near 0 and underpredictions near 1. Model performance was stable across the study regions with RMSE values for the Southern Black Forest: 0.21, Northern

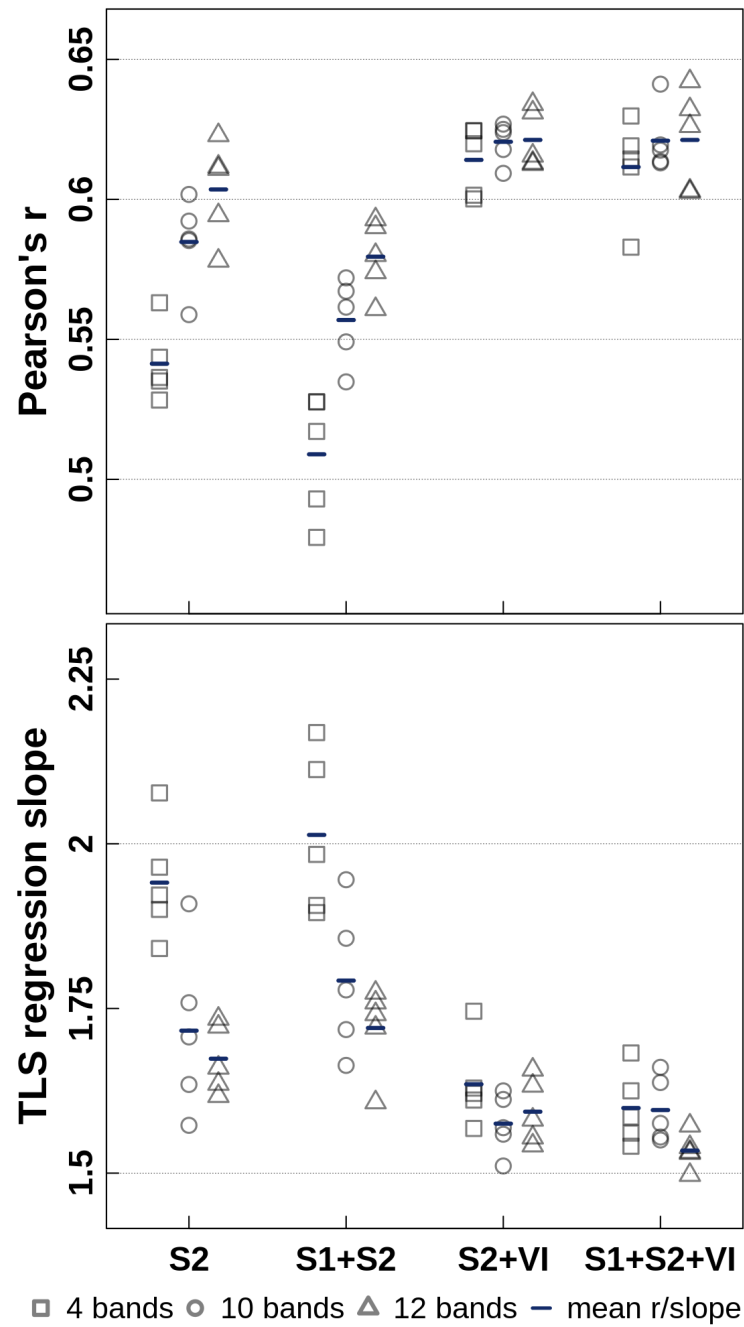


Figure 3.5: Pearson's r (upper panel) and total least squares regression slope (lower panel) of the five times repeated ten-fold cross-validations of the LSTM models for different inputs of Sentinel-1 and Sentinel-2 band sets (S2: Sentinel-2; S1+S2: Sentinel-1 and Sentinel-2; S2+VI: Sentinel-2, kNDVI, and NDWI; S1+S2+VI: Sentinel-1, Sentinel-2, kNDVI, and NDWI), each with different Sentinel-2 bands (4: 10 m bands; 10: 10 & 20 m bands; 12: 10, 20 & 60 m bands).

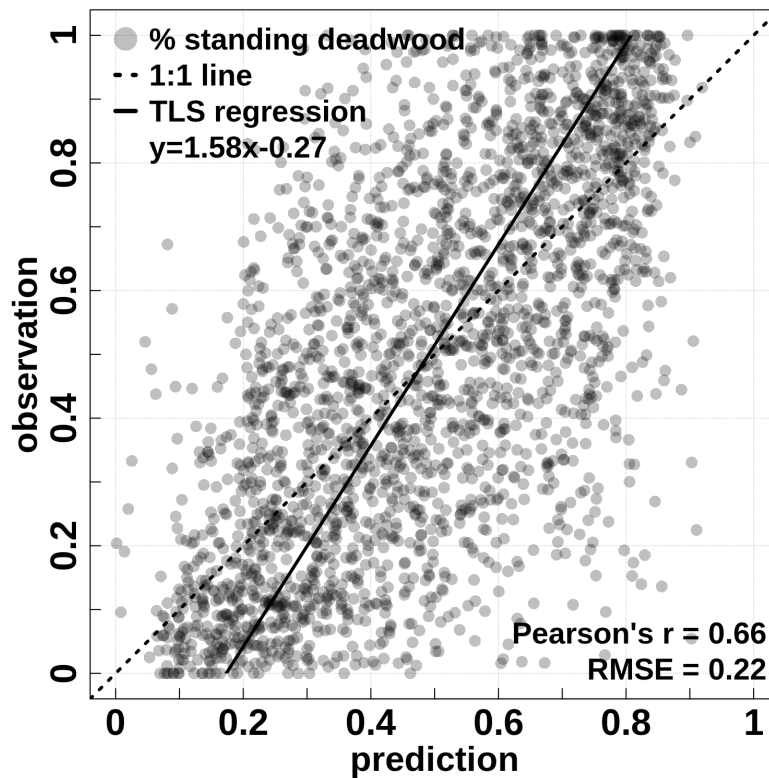


Figure 3.6: Scatterplot of observed and predicted fractional cover values of standing deadwood [%] at landscape level from the selected LSTM model (S_1+S_2+VI , 12 Sentinel-2 bands). Each dot represents a 10 m Sentinel-2 pixel with reference data available from the UAV-based segmentation.

Black Forest: 0.21, Dresden Heath: 0.22, Karlsruhe-Bretten: 0.23, Hainich National Park: 0.21, and Helsinki: 0.19 (see Appendix A5 for site-specific values).

Figure 3.7 shows the Sentinel-based prediction map of standing deadwood cover for the year 2020 using the previously selected best-performing LSTM model (S_1+S_2+VI with 12 Sentinel-2 bands) exemplary for the Saxon Switzerland National Park and its surroundings in Germany. The latter was largely affected by the drought events of 2018 and 2019 and thus provides a suitable test region with large gradients in deadwood cover. As expected, the map overview (centre) reveals ample occurrences of tree mortality in the National Park, with 24.1% of the Sentinel pixels showing more than 50% standing deadwood cover and 6.6% of the pixels showing more than 75% standing deadwood cover. As can be seen in comparison with independently acquired aerial orthoimagery in the close-up panels (top and bottom), crown cover of standing deadwood was accurately predicted from Sentinel data with a high spatial detail (10 m spatial resolution).

3 UAV-BASED REFERENCE DATA FOR THE PREDICTION OF FRACTIONAL COVER OF STANDING DEADWOOD FROM SENTINEL TIME SERIES

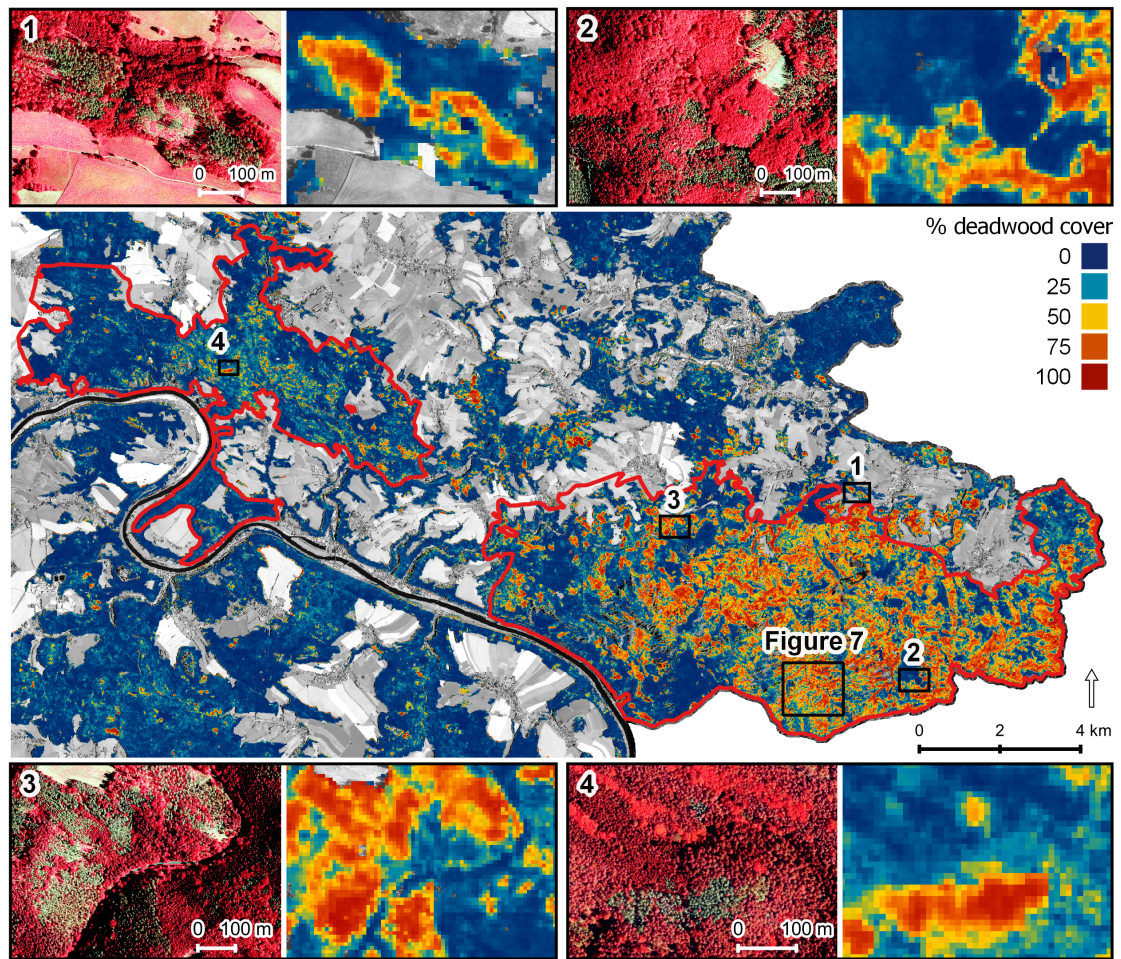


Figure 3.7: Sentinel-based LSTM prediction map of fractional standing deadwood cover for the year 2020 in Saxon Switzerland National Park (red outline), Germany (Coordinate reference system: WGS84 UTM zone 33N, EPSG:32633; centre coordinates: 450795.3, 5638435.7). Close-ups in the panels show amplified examples of forest condition in Colour infrared-orthophotos (Staatsbetrieb Geobasisinformation und Vermessung Sachsen, GeoSN) and corresponding prediction maps.

Annual LSTM prediction maps of standing deadwood cover in an example region in the Saxon Switzerland National Park for the years 2018 to 2021 are shown in Figure 3.8. The lower left panel displays histograms of fractional cover values of standing deadwood for each year between 2018 and 2021. After an initial crown dieback in 2018, most of the area was affected by tree mortality in 2019. The number of pixels classified with high fractions of standing deadwood subsequently decreased in the years 2020 and 2021. In the same years, more pixels with small values of standing deadwood cover can be observed in the histogram and are also apparent in the LSTM prediction maps as dark blue patches.

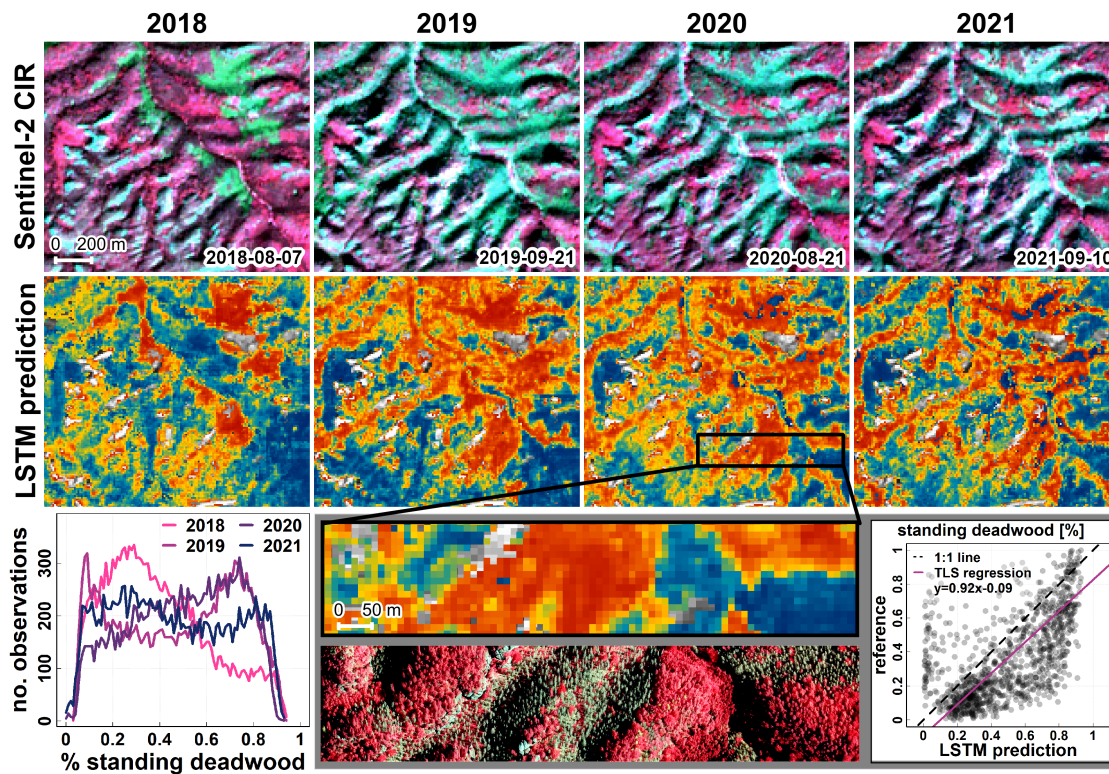


Figure 3.8: Sentinel-2 colour infrared image (CIR; top row; R=B8, G=B3, B=B2) and LSTM prediction maps of standing deadwood cover (centre row) in an example region in Saxon Switzerland National Park (see Figure 7 for the extent) across the years 2018, 2019, 2020, and 2021 (Coordinate reference system: WGS84 / UTM zone 33N, EPSG:32633; centre coordinates: 444628, 5643575). The histogram shows the standing deadwood cover values for each year. The grey box shows an independent validation of the LSTM predictions based on fractional cover values derived from an aerial orthophoto. Source CIR-orthophoto: Staatsbetrieb Geobasisinformation und Vermessung Sachsen (GeoSN)

3.4 DISCUSSION

3.4.1 UAV- AND CNN-BASED DEADWOOD SEGMENTATION AS A REFERENCE DATA SOURCE

With an F1-score of 0.85 from independent five-fold block cross-validation, the automated segmentation of standing deadwood in UAV imagery based on CNN models was confirmed to be very accurate. The very low median F1-score for the Hainich National Park sites (0.11) can be explained by the small proportion of standing deadwood for the respective sites, since even small areas can have a large relative effect on the model results (e.g., small branches that were classified

as deadwood but were not labelled as such in the reference data due to their small size). It should be noted that the model performance is based on reference data derived from a human interpreter. While the generation of reference data from visual interpretation of high-resolution imagery is a very common approach, it also comes with uncertainties that may likely result in an underestimation of the model performance (Kattenborn et al., 2021).

Consistent with our results, Sylvain et al. (2019) reported an F1-score of 0.95 for classifying tree health status (live or dead trees) using a VGG16 CNN on RGB aerial photos (20 cm GSD) over 990 1 ha sites in south-central Quebec, Canada. Jiang et al. (2019) also reported very high accuracies for the segmentation of standing dead trees using an FCN-DenseNet CNN, based on two airborne colour-infrared orthomosaics (20 cm GSD) from the Bavarian Forest National Park, Germany. Sani-Mohammed et al. (2022) used a Mask R-CNN for an instance segmentation of standing dead trees from an airborne colour-infrared orthomosaics (20 cm GSD) over the Bavarian Forest National Park, Germany, and reported an F1-score of 0.87. Yet, the dataset used here likely comprises a higher variability in site and data conditions than in the aforementioned studies. In this study, the RGB-orthomosaics were acquired in six study regions over 176 sites that differ in forest stand composition and structure. Imagery was acquired with different drone platforms and sensors and at different times of the day over a five-year period, resulting in very different sun-sensor geometries and environmental and atmospheric conditions. Given this heterogeneity of the dataset, our results show that the CNN-based segmentation of standing deadwood was spatially and temporally robust and that the CNN models generalized well.

While the present study focuses solely on RGB imagery due to its relative ease of acquisition and wide availability, other sensor types are also commonly used for dead tree detection, including multispectral (Jiang et al., 2019; Meddens et al., 2011; Sani-Mohammed et al., 2022; Zielewska-Büttner et al., 2020), hyperspectral (Einzmann et al., 2021; Fricker et al., 2019), and LiDAR (Briechle et al., 2021; Hell et al., 2022). While higher spectral resolution remote sensing data may be advantageous for separating spectrally similar classes (e.g., tree species), we have shown that RGB data are sufficient for separating live and dead trees in very high-resolution UAV-imagery. It should be noted, however, that we only defined dead trees or trees with clear signs of dieback or foliage discolouration as deadwood and that we did not consider early stages of tree mortality (e.g., green attack following bark beetle infestation).

Alternative detection methods, such as instance segmentation (Chiang et al., 2020; Sani-Mohammed et al., 2022) or object detection (Safonova et al., 2019, 2022), would even allow to map tree individuals. However, this would not have added value to this study because for the landscape-level upscaling we targeted the fractional cover of deadwood per Sentinel-2 pixel rather than the number of dead trees. An instance segmentation approach would have further complicated the

labelling of reference data and increased model complexity (see review by Hoerer & Kuenzer, 2020).

An often-reported problem in deadwood detection tasks is the difficulty in separating deadwood from bare ground (Fassnacht et al., 2014; Meddens et al., 2011; Zielewska-Büttner et al., 2020). While these findings have primarily been reported for pixel-based classification algorithms, we did not encounter substantial misclassifications in the CNN-based deadwood segmentation, suggesting that high-resolution textures are sufficient to separate bare ground from dead trees. For the time series-based upscaling approach, we added reference data from open forest floor and areas with sparse herbaceous vegetation. LSTM model performances clearly improved compared to an LSTM without these additional data (results not shown).

Overall, the described procedure can be used as an effective tool for rapid generation of reference data for large areas. This not only fosters research in remote or inaccessible areas, but also allows for the collection of larger amounts of reference data than field-based data collection would allow. The models can also be used to continuously append reference datasets with predictions from newly acquired orthomosaics, despite varying site and scene characteristics (e.g., environmental and atmospheric conditions, sun-sensor geometry). In this context, it is important to note that there are several platforms that curate openly available UAV orthoimagery (mostly RGB data) contributed by research groups or citizen scientists (e.g., <https://geonadir.com>, <https://opendrop.de> or <https://openaerialmap.org>). In combination with the described CNN-based methods, these databases and their spatio-temporal coverage can greatly stimulate the potential of using UAV-based reference data for satellite-based applications (Kattenborn et al., 2019b).

3.4.2 LSTM-BASED MODELLING OF STANDING DEADWOOD FROM SATELLITE TIME SERIES

Our results from the LSTM-based modelling of standing deadwood showed that using all available spectral information from Sentinel-2 increased model performance. We observed the highest model performance (according to TLS-regression slope) when integrating all spectral bands from Sentinel-2, Sentinel-1 backscatter and interferometric coherence, and the vegetation indices kNDVI and NDWI. While it is generally assumed that neural networks do not require pronounced feature engineering, our results indicate that adding vegetation indices to the raw spectral information can further refine the model. This may be explained by the fact that vegetation indices are often based on physical principles (e.g., NDVI as a ratio of light absorption and scattering). Indirectly incorporating such physical consistency may constrain the complexity of a model and facilitate the learning process (Reichstein et al., 2019). While Sentinel-1 information alone decreased model performance when added to the Sentinel-2 bands (S_1+S_2), incorporating

physical constraints into the model by means of vegetation indices (S_1+S_2+VI) also allowed the radar information to be used and thus showed the best model performance.

At first glance, LSTM model performance in upscaling, with a Pearson's r of 0.66 and an RMSE of 22% (S_1+S_2+VI), may not appear very high. Nevertheless, we consider these model performances promising considering the following aspects: Standing deadwood may appear very differently for different species and also for different stand characteristics. For instance, the different growth forms of broadleaf and needleleaf trees not only have different textural and spectral characteristics of healthy tree individuals but are also reflected in the appearance of dead tree crowns, complicating the modelling task. Different temporal signatures (e.g., deciduous and evergreen species) may further add complexity to the model, although little is known about this effect and its interactions with the textural and spectral properties. Moreover, in the UAV-based reference data acquisition, standing dead tree crowns were segmented by an area corresponding to a convex hull of the branches (see Figure 3.4). Thus, due to gaps within branches or holes in the canopy, the segmented canopy area may not exactly match the true cover of a dead tree crown, and thus the relationship between cover and reflectance signals may be compromised. This effect adds even more complexity when dense understory distinctly shines through the dead tree crowns (Frolking et al., 2009), which further constrains the isolation of unique spectral features of dead tree crowns in an already subtle process of non-stand replacing tree mortality. Thus, the task of mapping dead tree crowns may appear more trivial than it actually is, particularly for large environmental gradients.

Other studies have attempted to map tree mortality at landscape-level using upscaling approaches from high resolution aerial images to coarser resolution Landsat imagery (Campbell et al., 2020; Hart & Veblen, 2015; Meddens et al., 2013; Schwantes et al., 2016). Reported accuracies for the local-level predictions were comparably high but required more sophisticated input data (e.g., additional lidar data) or (pre)processing than the UAV RGB imagery and the end-to-end learning CNNs used here. Although these studies reported higher accuracies for landscape-level predictions, comparison of the results is limited because the coarser resolution of Landsat hardly accounts for subtle and small-scale deadwood occurrences and because of different definitions of deadwood (e.g., grey stage was excluded in Meddens et al., 2013).

Model performance was estimated using spatial block cross-validation, where each individual site with available UAV data was treated as a block during the cross-validation. Although several methods have been recommended to alleviate optimistically biased model performance (Burman et al., 1994; Roberts et al., 2017), recent studies suggest that spatial dependence in the raw data is often overlooked (Ploton et al., 2020). This is particularly the case in deep learning-based studies, where random cross-validation schemes prevail and spatial independence between

training and validation data is not always ensured (Kattenborn et al., 2022). Thus, the model performance assessed in this study may not be directly comparable to similar approaches using other biased validation schemes that do not account for the spatial dependence between training and test datasets. It should also be noted that the model performance was tested across years and regions, while growing seasons, and thus temporal patterns of the spectral signatures, may largely deviate across time and space (Hufkens et al., 2012; Verbesselt et al., 2010). Linking the two data sources is essential for model training, so the data must be spatially and temporally matched.

Reference data from UAV orthomosaics were acquired throughout the entire growing season (April to November), while the end of a satellite time series was set to October 30 of the respective year. Setting a specific end date was motivated by the LSTM modelling, which is facilitated by equidistant and synchronized time series. Consequently, a standing dead tree crown visible in a UAV scene was considered to be dead for the entire year of the acquisition. However, this may not be completely true for all observations, and such temporal mismatches may further reduce the estimated model performance.

In addition to a temporal mismatch between UAV and Sentinel data, a spatial mismatch can also hinder model training and reduce model performance estimates. In this regard, spatially more accurate UAV acquisitions using real-time kinematic (RTK) GNSS data may be very promising (not available in this study). However, it should be noted that RTK base stations are not always easy to deploy in forest environments, and RTK-based surveys only improve the absolute positional accuracy of the UAV data. A spatial mismatch between UAV and satellite data may remain, as the absolute geolocation accuracy of, for example, Sentinel-2 is specified at 12.5 m (Gascon et al., 2017). Additionally, automatic co-registration methods, such as scale-invariant feature transform SIFT (Lowe, 2004), are not suitable for remote sensing data with very different spatial resolutions, since the extracted image features will not be found in both images. Therefore, we tested a simple optimization method that co-registers resampled UAV imagery and the Sentinel-2 RGB-bands by iteratively shifting and rotating the UAV data and finding the maximum correlation of the spectral bands available in both datasets (i.e., red, green, and blue). Gränzig et al. (2021) presented a similar optimization approach where the optimal position is determined by the optimal fit between UAV-derived land cover fractions and Sentinel-2 spectral information. Independent validation of such optimization methods is difficult outside dedicated experiments, and we assumed the method to be valid if the LSTM model performance improved in the upscaling approach. Contrary to our assumption, the LSTM model performance did not improve (presumably due to the different UAV acquisition times compared to the constant Sentinel-2 overpass time and the resulting differences in lighting situation and shadows), and we decided to discard the co-registration approach in

this study. Yet, future studies may address the co-registration problem to further improve the potential of the presented approach.

Despite the presented sources of uncertainty, our results indicate a high transferability across the individual study regions with evenly distributed RMSE values ranging from 0.23 for the Karlsruhe-Bretten region to 0.19 for Helsinki). An independent comparison between the extrapolations and aerial orthophotos in space (Figure 3.7) and time (Figure 3.8) also suggests a robust and consistent predictive performance of the LSTM model. Time series approaches are particularly useful for capturing dynamic processes such as tree mortality, since a static selection of acquisition dates introduces selection bias and hence uncertainty (Frantz et al., 2022). For instance, after disturbance, increased light availability on the ground facilitates rapid (re)growth and greening of understory vegetation (Frolking et al., 2009; Meng et al., 2018). In addition, visibility of the understory from a bird's-eye perspective is enhanced by the sparse canopies of standing dead trees (particularly for deciduous trees). Modelling approaches based on single image acquisitions might easily confuse this regrown understory with a vital overstorey. Time series approaches, on the other hand, capture the context and dynamics prior to canopy mortality and should detect canopy mortality more robustly. The LSTM is specifically designed to detect temporal features of tree mortality throughout the time series and to indicate whether standing deadwood was present in the year of interest. This might be particularly relevant under common forest management practices (i.e., salvage logging and sanitation harvest after disturbance), where standing dead trees may have already been removed and thus may be missed by single time-step algorithms. For example, it is possible that standing dead wood has already been removed by foresters (e.g., for timber usage or path safety), but the algorithm can still detect the temporal presence of standing deadwood based on corresponding features in a period of the time series. Thus, the presented time series-based approach is also capable of detecting rapidly evolving and short-lived occurrences of standing deadwood.

An often-reported advantage of deep neural networks are their end-to-end learning capabilities without the need for enhanced preprocessing steps. In this study, the preprocessing for the LSTM modelling was confined to linear interpolation of missing values in the satellite time series and cloud masking. Results from Rußwurm and Körner (2018) indicate that the latter can be learned jointly with the classification task, further reducing preprocessing. Thus, in concert with cloud platforms where massive amounts of raw satellite data are stored (e.g., DIAS, Google Earth Engine), models may be trained that indirectly learn data quality features and transformations analogous to data preprocessing, which in turn could enhance the data processing efficiency and robustness for applications over large spatial and temporal scales.

In this study, we demonstrated the upscaling from standing deadwood segmentation maps at local-level (centimetre range) to continuous cover fractions at

coarser resolution (10 m resolution) and large areas by combining pattern recognition in UAV imagery and satellite time series analysis. This approach exploits both the high spatial information of UAV imagery and the high spectral and temporal information of satellite data. The quantitative performance assessment using spatially explicit validation data (Figure 3.7) as well as the continuous and multi-temporal prediction maps (Figure 3.8) showed that the predicted continuous cover fractions do not only resemble large-scale tree mortality rates (e.g., of entire forest stands), but also robustly predict transitions of tree mortality cover fractions or scattered occurrences at small spatial scales. The fractional cover maps presented here do specifically reflect the presence of dead trees, but do not indicate other sources of forest loss, e.g., due to logging or intense forest fires. This can be particularly important for monitoring the typically widespread and patchy patterns of tree mortality events associated with climate extremes such as drought, disease, pathogens, and their combined effects.

3.5 CONCLUSION

Spatio-temporal information on forest mortality and associated processes is scarce, but urgently needed for understanding climate change risks on forests. Earth observation satellites could provide spatially and temporally explicit information on tree mortality, but mapping tree mortality with such data requires ample training data. In this study, we presented a workflow that enables large-scale mapping of tree mortality. The automated generation of reference data from high-resolution UAV imagery enables spatially explicit training and validation of landscape-level models, which is hardly possible with most existing reference data sources. Opportunities for optimization exist, particularly regarding the spatial and temporal consistency between UAV and satellite products, and the representation of natural variability in the appearance of dead tree crowns in corresponding remote sensing signals and should be subject to further research. Precise estimates of fractional cover of standing deadwood could be used with other products, e.g., biomass estimates, canopy height, or species maps, to estimate tree mortality-related changes in carbon dynamics. Deadwood is also an important forest structural parameter, and large-scale continuous information on its fractional cover may foster forest biodiversity research and management. With the appropriate UAV data for reference data generation, the approach can be adapted to a wide range of applications in vegetation remote sensing (e.g., tree species or habitat mapping). In the future, the increasing availability of openly available UAV data in concert with automated and transferable deep learning-based mapping algorithms will further increase the potential of such multiscale approaches.

CREDIT AUTHORSHIP CONTRIBUTION STATEMENT

Felix Schiefer: Methodology, Software, Validation, Formal Analysis, Investigation, Data Curation, Writing—Original Draft, Writing—Review & Editing, Visualization. **Annett Frick:** Conceptualization, Validation, Resources, Writing—Review & Editing. **Julian Frey:** Investigation, Data Curation. **Randolf Klinke:** Validation. **Katarzyna Zielewska-Büttner:** Writing—Review & Editing. **Andreas Uhl:** Investigation, Data Curation. **Samuli Junttila:** Investigation, Writing—Review & Editing. **Sebastian Schmidlein:** Resources, Writing—Review & Editing. **Teja Kattenborn:** Conceptualization, Methodology, Writing—Original Draft, Writing Review & Editing, Supervision, Funding acquisition.

DECLARATION OF COMPETING INTEREST

The authors declare that they have no known competing financial interests or personal relationships that could have appeared to influence the work reported in this paper.

ACKNOWLEDGEMENTS

The study has been funded by the German Aerospace Centre (DLR) on behalf of the Federal Ministry for Economic Affairs and Climate Action (BMWK) [FKZ 50EE1909A]. The data acquisition within the Southern Black Forest was funded by the German Research Foundation DFG [GRK 2123]. SJ was funded through the Academy of Finland under grants [330422, 337127]. We thank the 3DGeo Research Group at Heidelberg University for the provision of UAV imagery from the Karlsruhe-Bretten study site and the Forest Research Institute Baden-Württemberg (FVA) and Black Forest National Park for the provision of UAV imagery from the Black Forest. We acknowledge support by the KIT-Publication Fund of the Karlsruhe Institute of Technology.

4 LARGE-SCALE REMOTE SENSING REVEALS THAT TREE MORTALITY IN GERMANY APPEARS TO BE GREATER THAN PREVIOUSLY EXPECTED

This chapter has been submitted as: Schiefer, F., Schmidlein, S., Hartmann, H., Schnabel, F., & Kattenborn, T. (n.d.). Large-scale remote sensing reveals that tree mortality in Germany appears to be greater than previously expected. (*under review*) *Forestry: An International Journal of Forest Research*

ABSTRACT

Global warming poses a major threat to forests and events of increased tree mortality are observed globally. Studying tree mortality often relies on local-level observations of dieback, while large-scale analyses are lacking. Satellite remote sensing provides the spatial coverage and sufficiently high temporal and spatial resolution needed to investigate tree mortality at landscape-scale; however, adequate reference data are scarce. In a deep learning-based upscaling approach from drone imagery to satellite data, Schiefer et al. (2023a) mapped standing deadwood in Germany for the years 2018–2021 at 10 m resolution. Here, we used these maps to study spatial and temporal patterns of tree mortality in Germany and analysed their biotic and abiotic environmental drivers using random forest regression. In 2019, the second consecutive hotter drought year, standing deadwood increased steeply reaching 334 ± 189 kilohectar (kha; uncertainty estimates resulting from sensitivity analysis) of standing dead trees approximately $2.5 \pm 1.4\%$ of the total forested area in Germany. *Picea abies*, *Pinus sylvestris*, and *Fagus sylvatica* showed the highest shares of standing deadwood. Over the years 2018–2021, 978 ± 529 kha ($7.9 \pm 4.4\%$) of standing dead trees accumulated. The differences to other surveys (such as the ground-based forest condition survey) can be attributed to the fact that remote sensing captures mortality from a bird’s-eye perspective and that the high spatial detail (10 m) in this study also captures scattered occurrences of tree mortality. Atmospheric drought (i.e., climatic water balance and vapour pressure deficit) and temperature extremes (i.e., number of hot days and frosts after vegetation onset) were the most important predictors of tree mortality. We found increased tree mortality for smaller and younger stands and also on less productive sites, which mitigates the findings of local-level studies where tree height largely explained tree mortality patterns. We relate this to an averaging effect when investigating entire landscapes and assume that tree mortality is rather driven by competition, depending on tree age, height, and productivity. Monospecific stands were generally not more affected by mortality, but only when interactions with damaging insects (e.g., bark beetle) occurred. Because excess tree mortality rates threaten many forests across the globe, similar analyses of tree mortality are warranted and technically feasible at the global scale. We encourage the international scientific community to share and compile local data on deadwood occurrences (see example: www.deadtrees.earth) as only such a collaborative effort can reveal and help understand mortality events on a global scale.

4.1 INTRODUCTION

Forests cover one third of the total land surface (FAO, 2020), are an important carbon sink, and provide a range of ecosystem services. Climate change and the associated rise in temperatures, the occurrence of episodic precipitation and droughts, or an increased atmospheric water vapour deficit pose a major threat to forests (Hartmann et al., 2022; McDowell et al., 2022; Schuldt et al., 2020). Consequently, trees get stressed and may eventually die due to carbon starvation, hydraulic failure, or ensuing pest infestations. This cascade of effects is particularly pronounced during ‘hotter droughts’, in which long periods of drought coincide with high temperatures (Allen et al., 2015; Hammond et al., 2022). With the rise in average temperatures, an earlier start to the growing season has also been observed in recent years. Nevertheless, late-frost events can still occur after bud burst, which can weaken the trees, prevent resprouting, and may ultimately lead to mortality (Vanoni et al., 2016).

We currently witness the emergence of hotter droughts even in temperate regions, such as the droughts that occurred between 2018–2020 (Allen et al., 2015; Hammond et al., 2022). Consecutive (hotter) droughts have also become more frequent (Hari et al., 2020; Rakovec et al., 2022), and large-scale tree stress responses and diebacks have been observed after the prolonged 2018–2021 drought in Central Europe (Rakovec et al., 2022; Schnabel et al., 2022; Schuldt et al., 2020) and the 2012–2016 drought in Northern America (Byer & Jin, 2017). Even if the trees do not die in a first year of drought, such as 2018, critical ecosystem changes and mortality may still occur in the years after the drought, known as drought legacy or lag effects (Obladen et al., 2021; Pohl et al., 2023; Schnabel et al., 2022). Due to a climate that is increasingly characterized by extremes, all these stress responses can also occur together, creating compound effects (Zscheischler et al., 2018). Understanding the mechanisms that lead to tree mortality is crucial to assess the impact of ongoing global warming on forests and to adapt forest management strategies accordingly.

Many of these tree mortality-related mechanisms are known from local studies, but are not easily transferable to larger scales (Clark et al., 2016). Due to a lack of large-scale data sets on tree mortality, many of our findings arise from compiled and harmonized data sets of in situ observations of dieback events (Allen et al., 2010; Hammond et al., 2022). As there are no standardized survey methods, often only damaged areas of a certain minimum size are included in such data sets. This poses two problems for the investigation of the underlying causes: large-scale occurrences of standing deadwood often only accumulate over time. The temporal link between the environmental cause and the dieback event may therefore be weakened or already overlaid by other factors. Furthermore, scattered

and gradual occurrences of tree mortality are likely to be underrepresented in the aforementioned data sets (Cheng et al., 2024; Milodowski et al., 2017).

Climate change and associated pest and pathogen outbreaks have increased the risk of large-scale tree mortality (Allen et al., 2010; Huang et al., 2020; McDowell et al., 2020), but some mechanisms are still unknown. For example, Socha et al. (2023) suggest that higher productivity and greater tree age enhance susceptibility to drought-induced mortality. The effect of tree height on mortality is under debate. While smaller and younger trees die mainly due to competition for resources (Kulha et al., 2023; Stephenson & Das, 2020), larger and older trees have an accumulated risk of disease and damage (Bennett et al., 2015; Stovall et al., 2019, 2020). The influence of tree species richness on mortality remains ambiguous as well (Depauw et al., 2024). While a positive effect of tree species richness on the stability and productivity of forests is assumed to be likely due to a performance enhancing and buffering effects of diversity (Anderegg et al., 2018; Schnabel et al., 2021), studies found mixed results regarding the effect of tree diversity on forest responses to drought (Grossiord et al., 2014). While recent experimental work points towards a generally positive or non-significant effect of tree diversity on tree mortality, Searle et al. (2022) found higher tree diversity to be correlated with higher tree mortality. These, at a first glance, contradictory results clearly illustrate that tree mortality is still not generically understood. The mechanisms that have been identified as causal for tree mortality at the individual tree level have not been investigated or confirmed at the landscape level and require further research (McDowell et al., 2022).

Large-scale patterns of tree mortality can be revealed using Earth observation satellite missions (Brodrick & Asner, 2017; Byer & Jin, 2017; Garrity et al., 2013; Hansen et al., 2013; Schwantes et al., 2016). Large-scale remote sensing assessments are based on satellite data that usually feature spatial resolutions that are much coarser than the tree canopies being targeted, such as 250 m spatial resolution of MODIS down to 30 m of Landsat (Byer & Jin, 2017; Campbell et al., 2020; Schuldt et al., 2020; Schwantes et al., 2016). Only a few studies use higher spatial resolution satellite data, for example 10 m spatial resolution of Sentinel-2 (Thonfeld et al., 2022), 3 m of PlanetScope (Francini et al., 2020), or even down to 0.5 m of WorldView and Quickbird (Garrity et al., 2013; Liu et al., 2021). Aerial images, such as those acquired from aircraft (Khatri-Chhetri et al., 2024; Schwarz et al., 2023) or uncrewed aerial vehicles (UAV, Schiefer et al., 2023a), offer an even higher spatial resolution. For accurate detection of dead trees, a higher spatial resolution (<10 cm) is more important than a high spectral resolution (Khatri-Chhetri et al., 2024; Schiefer et al., 2020). Reference data are the main limiting factor for large-scale, satellite-based remote sensing analyses of tree mortality (Schiefer et al., 2023a). Hence, studies often do not map tree mortality directly, but changes of vegetation indices as a proxy of dieback. However, the causes for such changes in

vegetation indices could be manifold and may not necessarily be linked to tree mortality but rather to vitality decline.

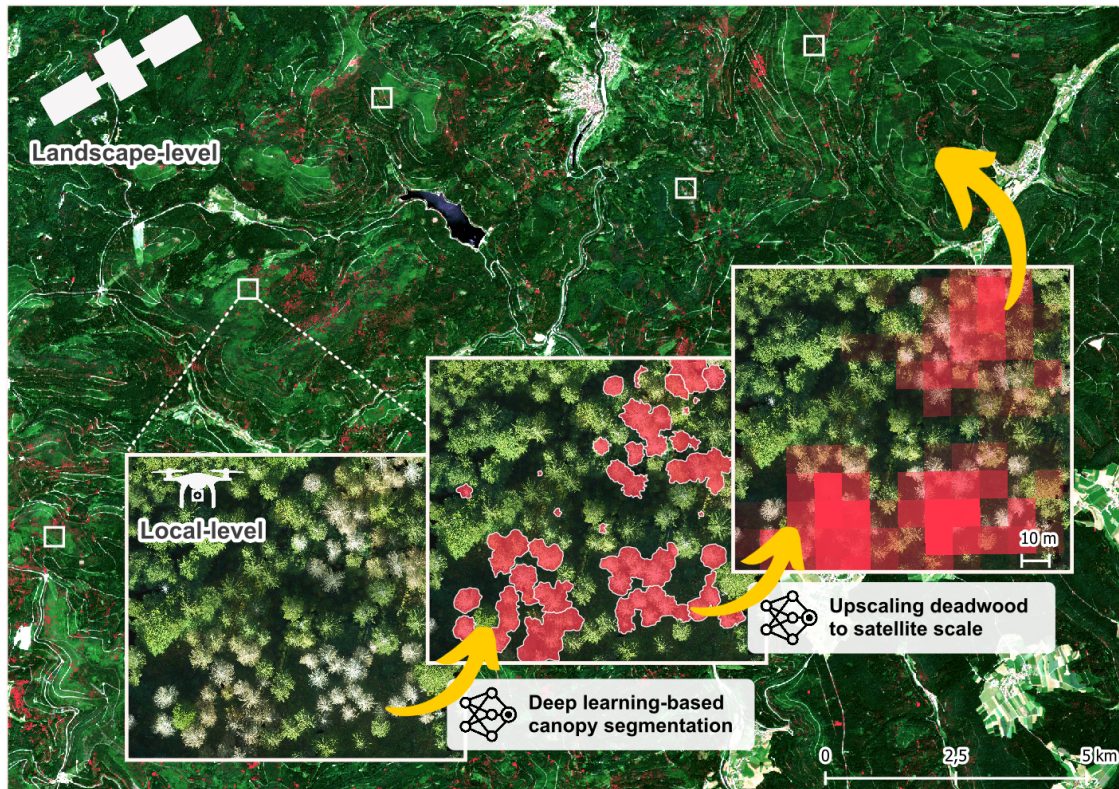


Figure 4.1: Schematic overview of the presented upscaling approach in Schiefer et al. (2023a) extrapolating local observations of standing deadwood in UAV-imagery landscape-level predictions based on satellite image time series.

Tree mortality can be scattered across the landscape and only affect individual trees in an otherwise intact and green canopy. The spatial resolution of existing large-scale satellite-based products cannot capture this adequately, and detected tree mortality events from such data sources typically reflect larger events and neglect smaller patches. Although high-resolution aerial imagery from aircraft and UAVs can provide this high spatial resolution, they are limited in their spatial and temporal coverage and hence can only provide spatial snapshots of tree mortality processes. Therefore, Schiefer et al. (2023a) presented an upscaling approach that combines the high spatial detail UAV imagery offers at local scales and the large-spatial coverage from the Sentinel satellites (see Figure 4.1). Their upscaling approach resulted in Germany-wide maps of fractional cover of standing deadwood at the original Sentinel image resolution of 10 m for the consecutive years 2018–2021. Such an extensive and detailed dataset provides a base for

large-scale, reproducible assessment of tree mortality dynamics. Here, we use this dataset to reveal the spatio-temporal dynamics of standing deadwood in Germany, and studied the species-specific patterns using tree species information from Blickensdörfer et al. (2024). We further investigate the influence of several biotic and abiotic environmental drivers on the observed tree mortality at landscape level.

4.2 MATERIAL AND METHODS

4.2.1 TREE MORTALITY IN GERMANY

To identify and study the pattern of tree mortality, we extracted fractional cover values of standing dead trees for the available years 2018–2021 from the Germany-wide layers Schiefer et al. (2023a)—an interactive preview is available at www.deadtrees.earth. This product was built from automatically segmented crowns of standing dead trees from very high-resolution UAV imagery available at local scales using convolutional neural networks (CNN). These segmentations were converted to cover fractions of standing deadwood per 10 m Sentinel-2 pixel and fed into long short-term memory networks (LSTM) for large-scale extrapolation using time series of Sentinel-1 and Sentinel-2 as predictors. The final Germany-wide maps show the percentage of standing deadwood per satellite pixel.

As standing deadwood is not always necessarily removed from the forest, it can appear in a pixel in consecutive years. To establish a meaningful link between the occurrence of standing deadwood and the prevailing environmental conditions and to only identify newly occurring standing deadwood, we, therefore, only considered the year of first occurrence of standing deadwood. We defined the year of the first occurrence of standing deadwood as the point at which the fractional cover exceeds a certain threshold for the first time. We conducted a sensitivity analysis applying different thresholds of standing deadwood continuously between 30% and 70% and averaged the results to avoid bias in the results by setting an arbitrary threshold. We calculated standard deviations to provide uncertainty estimates of the observed standing deadwood. The yearly binary maps of first occurrence then only served as a mask, and in subsequent analysis again the percentages of standing deadwood were used. We then overlaid the standing deadwood maps with maps of the dominant tree species by Blickensdörfer et al. (2024), who used national forest inventory and remote sensing to map 11 tree species in Germany, i.e., *Pinus sylvestris* (22% area share), *Picea abies* (31.4%), *Pseudotsuga menziesii* (2%), *Abies alba* (2%), *Larix spp.* (2.6%), *Fagus sylvatica* (15.1%), *Quercus spp.* (8.9%), *Betula pendula* (2.1%), *Alnus glutinosa* (2.6%), and two other deciduous species groups. The map of Blickensdörfer et al. (2024) has a spatial resolution of 10 m.

We assessed regional differences for Germany's 73 major natural regions first defined by Meynen and Schmithüsen (1953) adapted by the Federal Office for Nature Conservation (Bundesamt für Naturschutz—BfN). The major natural regions divide Germany into physical units of similar geography primarily based on geomorphological, geological, hydrological, and pedological criteria. They allow for a regional comparability beyond administrative boundaries.

4.2.2 IDENTIFYING DRIVERS OF TREE MORTALITY USING RANDOM FOREST

To identify the main predictors of tree mortality in Germany, we calculated random forest models (Breiman, 2001) using the previously described standing

Table 4.1: Environmental predictor variables

Variable	Spatial resolution	Unit	Data source
Slope		°	Slope and eastness (sinus) and northness (cosine) of terrain aspect derived from Copernicus DEM (2021)
Eastness	10 m	rad	
Northness		rad	
Sand content	30 m	%	Hengl, T. and Parente, L. (2022)
Stand age	100 m	years	Besnard et al. (2021)
Canopy height	10 m	m	Lang et al., 2023
Tree species richness	10 m	no.	Calculated from Blickensdörfer et al. (2024) as number of tree species in a 100 m buffer
Temperature annual range		°C	
Precipitation seasonality	30 sec	mm	Derived from Fick and Hijmans (2017)
Precipitation of warmest quarter		mm	
Late frosts*	1 km	days	Calculated from vegetation onset (DWD, 2023b) and CERRA reanalysis (Schimanke et al., 2021)
Soil drought intensity*	4 km	-	During vegetation period (Zink et al., 2016)
Vapour pressure deficit	5.5 km	Pa	Calculated as 75%-quartile of daily maximum during growing period (March-October) from CERRA reanalysis (Schimanke et al., 2021)
Climatic water balance*	1 km	mm	Calculated from DWD (2023d, 2023e) as anomaly from DWD (2023f)
Hot days*	1 km	days	DWD (2023a)
Biomass	100 m	Mg/ha	ESA Biomass CCI (Santoro & Cartus, 2023)
Net Primary Productivity	500 m	kgC/m ² /year	Running, S. and Zhao, M. (2021)

*Variable also for the year prior to the first occurrence of standing deadwood

4 LARGE-SCALE REMOTE SENSING REVEALS THAT TREE MORTALITY IN GERMANY APPEARS TO BE GREATER THAN PREVIOUSLY EXPECTED

deadwood maps as a response and 21 environmental predictor variables (Table 4.1). We dropped predictor variables with correlations higher than 0.7 to rule out multicollinearity, so that the ecologically more meaningful variable remained (Figure 4.2). An overview of the originally selected environmental variables along with the rationale for the selection of variables can be found in Appendix A6.

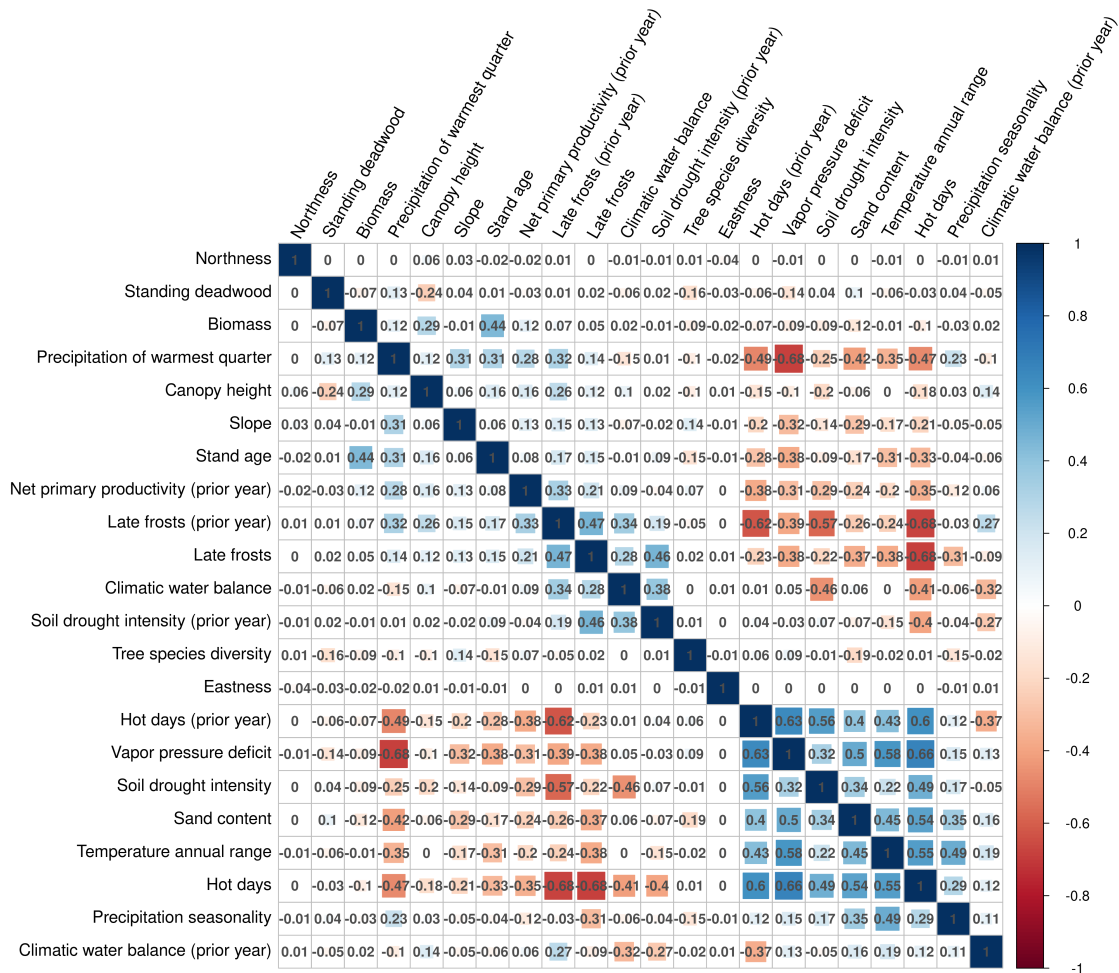


Figure 4.2: Correlation plot for the selected 21 environmental predictor variables and standing deadwood. Variables with correlations higher than 0.7 were dropped for subsequent analyses.

We separately analysed the seven main tree species—as defined by the German national forest inventory—*Fagus sylvatica*, *Quercus spp.*, *Picea abies*, *Pinus sylvestris*, *Abies alba*, *Pseudotsuga menziesii*, and *Larix spp.*. We ran random forest models for each species individually. For every model, we randomly sampled 32 000 observations (Sentinel-2 pixel equivalents), half with and half without standing deadwood.

To build temporally transferable models, we sampled 4 000 observations per each year of first occurrence. For every model, we calculated permutation importances and accumulated local effects (ALE, Apley and Zhu, 2020). Permutation importance measures the increase in model prediction error after permuting a variable's values, and is a straightforward means for identifying important variables. ALE plots further describe how a variable influences model predictions on average and can help understand the direction of a variable's effect. ALE plots are an alternative to the well-known partial dependence plots (Friedman, 2001) but they are less prone to erroneous results due to intercorrelated variables and are less computational demanding (Apley & Zhu, 2020). We repeated this procedure 100 times for every species and averaged the permutation importances and accumulated local effects. Based on model residuals, we calculated Moran's I to rule out spatial autocorrelation for the models (with all values being below 0.04). All analyses were conducted in R language (R Core Team, 2022) using the packages 'ranger' for the random forest implementation (Wright & Ziegler, 2017) and 'iml' for the accumulated local effects (Molnar et al., 2018).

4.3 RESULTS

In 2018 $1.4 \pm 1.0\%$ and an approximate area of 179 kilohectares (kha) of Germany's forests were dead (Figure 4.3). The largest share corresponds to *Pinus* with 113 ± 81 kha, which equates to $4.4 \pm 2.9\%$ of all *Pinus* trees in Germany. In 2019, standing deadwood increased for most species and particularly for *Picea* ($6.3 \pm 2.1\%$, 88 ± 39 kha) and *Pinus* ($6.7 \pm 3.8\%$, 201 ± 118 kha). 334 \pm 189 kha of forest died in 2019, approximately $2.5 \pm 1.4\%$ of the forested area in Germany. In 2020, the total amount of new standing deadwood slightly decreased to $2.6 \pm 1.3\%$ and 307 \pm 151 kha. For *Picea* ($8.3 \pm 2.5\%$, 146 ± 44 kha), *Fagus* ($3.5 \pm 1.5\%$, 17 ± 8.2 kha) and *Quercus* ($2.1 \pm 0.8\%$, 2.1 ± 1.2 kha) standing deadwood peaked in 2020. In 2021, mortality rates further decreased for all species. Accumulated over the years, in total 978 \pm 529 kha of forest died from 2018 to 2021, accounting for $7.9 \pm 4.4\%$ of the forested area in Germany. The variation around the mean of the different threshold values for the determination of the first occurrence of standing deadwood was high for some species, particularly *Pinus*. Detailed statistics of the temporal development of standing deadwood for the different species can be found in Appendix A8.

The mortality patterns between 2018–2021 varied considerably by region (Figure 4.4a). The most affected regions in terms of area of standing deadwood (Figure 4.4b) were Süder Uplands (region ID D38, 74.2 kha) and Harz (D37, 47.2 kha), followed by Fläming Heath (D11, 26.5 kha), Elbe-Mulde-Plain (D10, 26.1 kha), Brandenburg Heath and Lake District (D12, 25.1 kha), Lower Saxon Hills

4 LARGE-SCALE REMOTE SENSING REVEALS THAT TREE MORTALITY IN GERMANY APPEARS TO BE GREATER THAN PREVIOUSLY EXPECTED

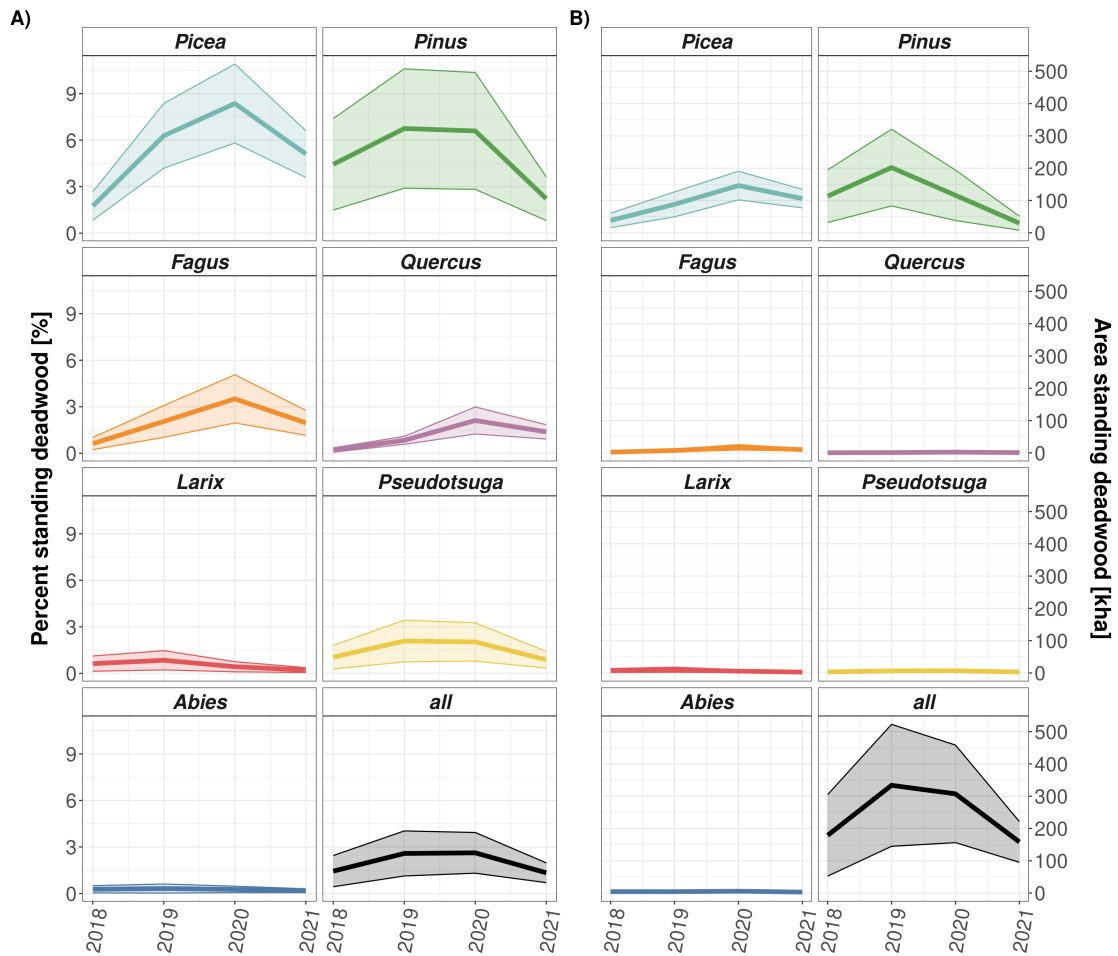


Figure 4.3: Temporal development of new standing deadwood from 2018 to 2021 for main tree species (*Abies*, *Fagus*, *Larix*, *Picea*, *Pinus*, *Pseudotsuga*, and *Quercus*) in Germany. A) The proportion of standing deadwood (% of the respective species), B) total affected area of the species (kha). The thick line represents the mean of the various threshold values, the correspondingly coloured ribbon the standard deviation.

(D36, 20 kha), Middle Elbe Plain (D09, 19.3 kha), and Wendland and Altmark (D29, 19 kha). The most affected regions in terms of percentage of standing deadwood (Figure 4.4c) were Harz (D37, 30.2%), Elbe-Mulde-Plain (D10, 21.4%), Middle Elbe Plain (D09, 21.1%), Saxon-Bohemian Chalk Sandstone Region (D15, 18.4%), Süder Uplands (D38, 17.1%), Wendland and Altmark (D29, 16.8%), Fläming Heath (D11, 16.4%), and Lusatian Basin and Spreewald (D08, 12.6%). A detailed overview of the accumulated standing deadwood during 2018–2021 for the major natural regions of Germany can be found in Appendix A9.

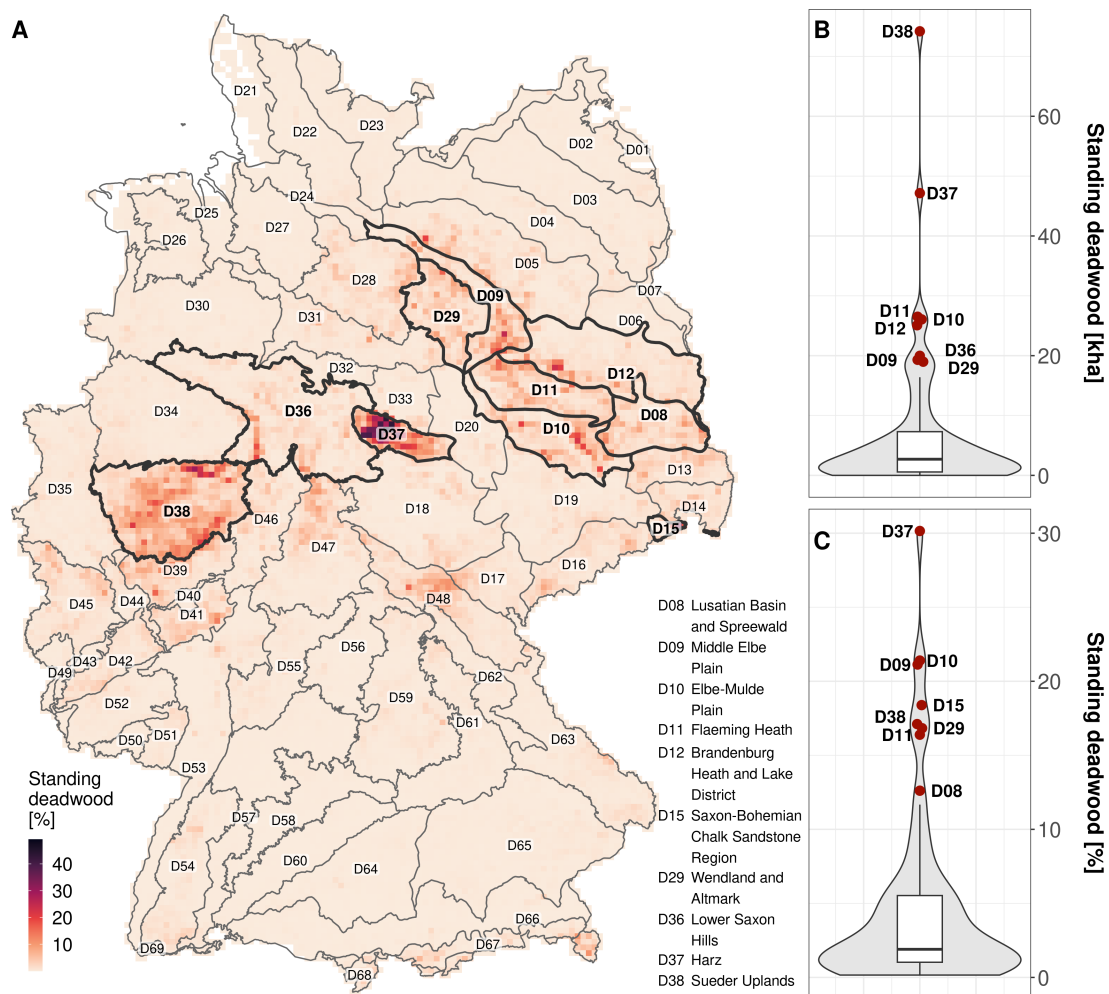


Figure 4.4: Accumulated standing deadwood from 2018–2021 for the major natural regions in Germany. (A) Map of accumulated standing deadwood in percent of the forested area. For visualization purposes, the maps from Schiefer et al. (2023a) were aggregated to 5 km spatial resolution. Most affected regions are highlighted with a bold outline, and region names along with the IDs (according to the official naming convention) are given in the figure. For the names of all other regions, see 5.4. (B) Total area [kha] and (C) percent [%] of affected forest areas for the major natural regions in Germany.

The mean explained variance (coefficient of determination R^2) of the species-specific random forest models was 0.68 for *Pinus*, 0.64 for *Abies*, 0.6 for *Fagus*, 0.46 for *Quercus*, 0.43 for *Picea*, 0.43 for *Pseudotsuga*, and 0.36 for *Larix*. The random forest permutation importance (Figure 4.5) reveals that climate and weather were the most important environmental factors explaining standing deadwood

4 LARGE-SCALE REMOTE SENSING REVEALS THAT TREE MORTALITY IN GERMANY APPEARS TO BE GREATER THAN PREVIOUSLY EXPECTED

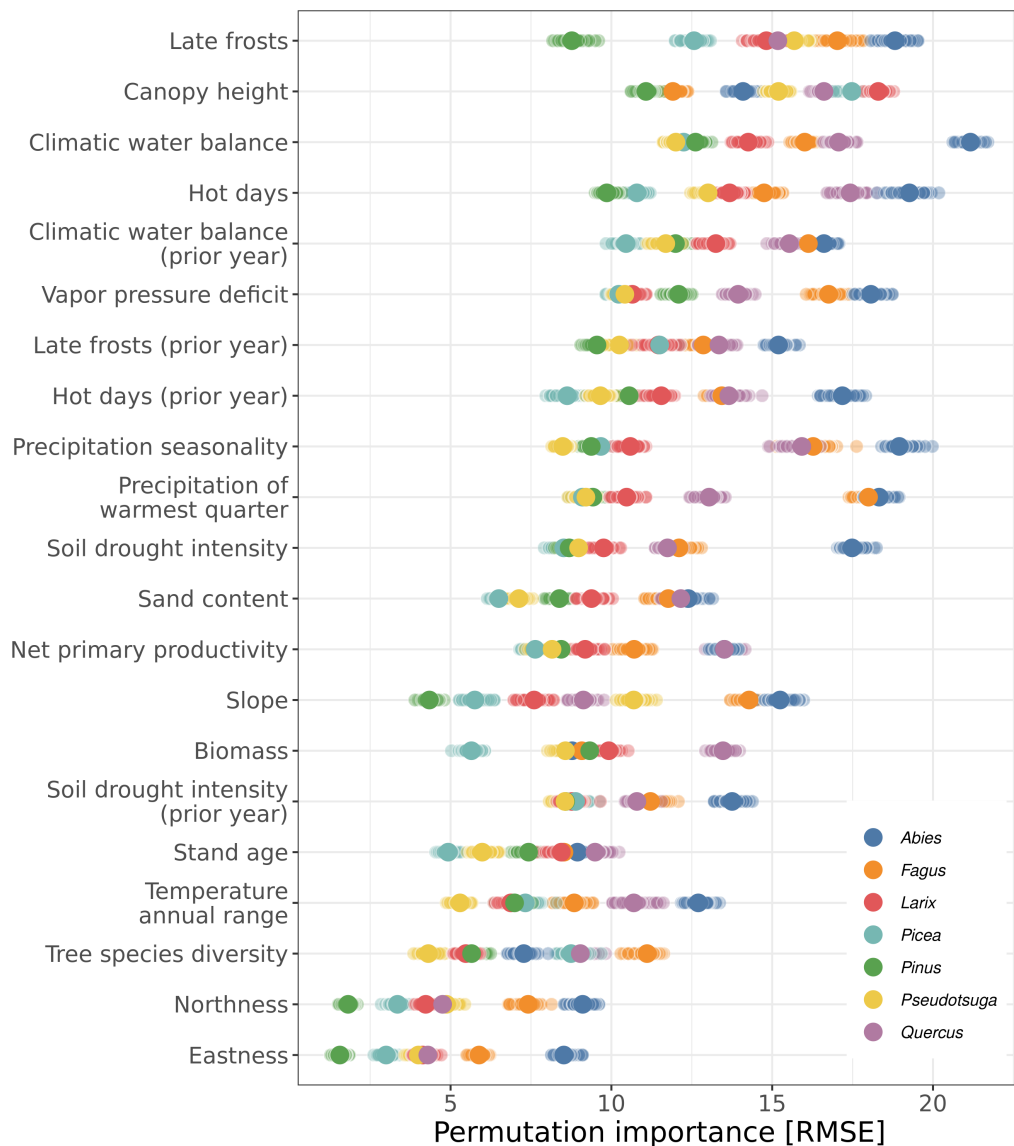


Figure 4.5: Variable permutation importance of the random forest models. Variables are in descending order according to their median variable importance over all species.

dynamics. Late frost was the most important variable (median permutation importance RMSE across species = 15.3%) followed by canopy height (15.2%) as the only non-climate/weather variable in the top group. Variable importances ranked three to ten were climatic water balance (14.3%), hot days (13.7%), climatic water balance of the prior year (13.2%), vapour pressure deficit (12.1%), late frosts of the prior year (11.7%), hot days of the prior year (11.6%), precipitation seasonality (10.6%), and precipitation of the warmest quarter (10.5%). The least

important climatic variable was temperature annual range (7.4%, rank 18). The edaphic variables soil drought intensity (9.8%), sand content (9.4%), and soil drought intensity of the prior year (9%) were less important for the models than the climatic variables. Net primary productivity (9.2%) and biomass (9%) ranked 13 and 15 in variable importance. The forest stand-related variables stand age (8.3%) and tree species richness (7.3%) ranked 17 and 19. Slope (9.1%) was the most important variable with the topographic site conditions. The aspect variables northness (4.7%) and eastness (4.1%) were the overall least important variables. *Abies* showed the highest importances for most of the variables, except for canopy height, biomass, stand age, and tree species richness. Lowest importances were observed for *Pinus* for most of the variables. Variables from the year of first occurrence of standing deadwood were more important than the respective variables from the prior year.

Detailed relationships were obtained using the local effect plots created for each of the 21 predictor variables (Figure 4.6). Surprisingly, late frosts showed no clear effect across species despite its high variable importance. *Pseudotsuga*, *Picea*, and *Abies*, however, showed a decreased mortality with more days of late frost, indicating a tolerance to frosts. For *Fagus* the effect was reverse with an increased mortality with more days of late frost. Late frosts of the prior year showed a clearer picture with an increased mortality with more days with late frosts for *Quercus*, *Pinus*, *Fagus*, and *Larix*. *Abies*, *Pseudotsuga*, and *Picea* were again more tolerant to late frosts. The effect of canopy height was similar across all species, with smaller trees linked to more and taller trees linked to less standing deadwood. This effect was largest for *Larix* and smallest for *Abies*. The effect of the climatic water balance was the same for all species and a more negative climatic water balance was linked to more standing deadwood, except for *Abies* that was inverted. For *Picea*, a smaller deficit was sufficient for increased mortality. Since *Abies* largely occurs at higher altitudes with higher precipitation, the precipitation amounts are still sufficient to compensate for the observed effect of the climatic water balance. The climatic water balance of the prior year showed the same general trends but with a smaller effect. Hot days are defined as days with a maximum temperature above 30 °C. The effect of hot days on the fraction of standing deadwood was similar for all species, with higher mortality with more hot days. When exceeding 11 to 17 hot days, depending on the species, more standing deadwood was observed. The effect of more hot days on standing deadwood was stronger for the current than the previous year. The largest effect of hot days for both years was observed for *Abies* and *Fagus*.

The differences in the effects between the species were greatest for vapour pressure deficit. *Quercus*, *Larix*, *Pinus*, *Pseudotsuga*, and *Picea* behaved similarly with increasing fraction of standing deadwood at higher vapour pressure deficits. However, the deficit at which the effect changed to more standing deadwood was

4 LARGE-SCALE REMOTE SENSING REVEALS THAT TREE MORTALITY IN GERMANY APPEARS TO BE GREATER THAN PREVIOUSLY EXPECTED

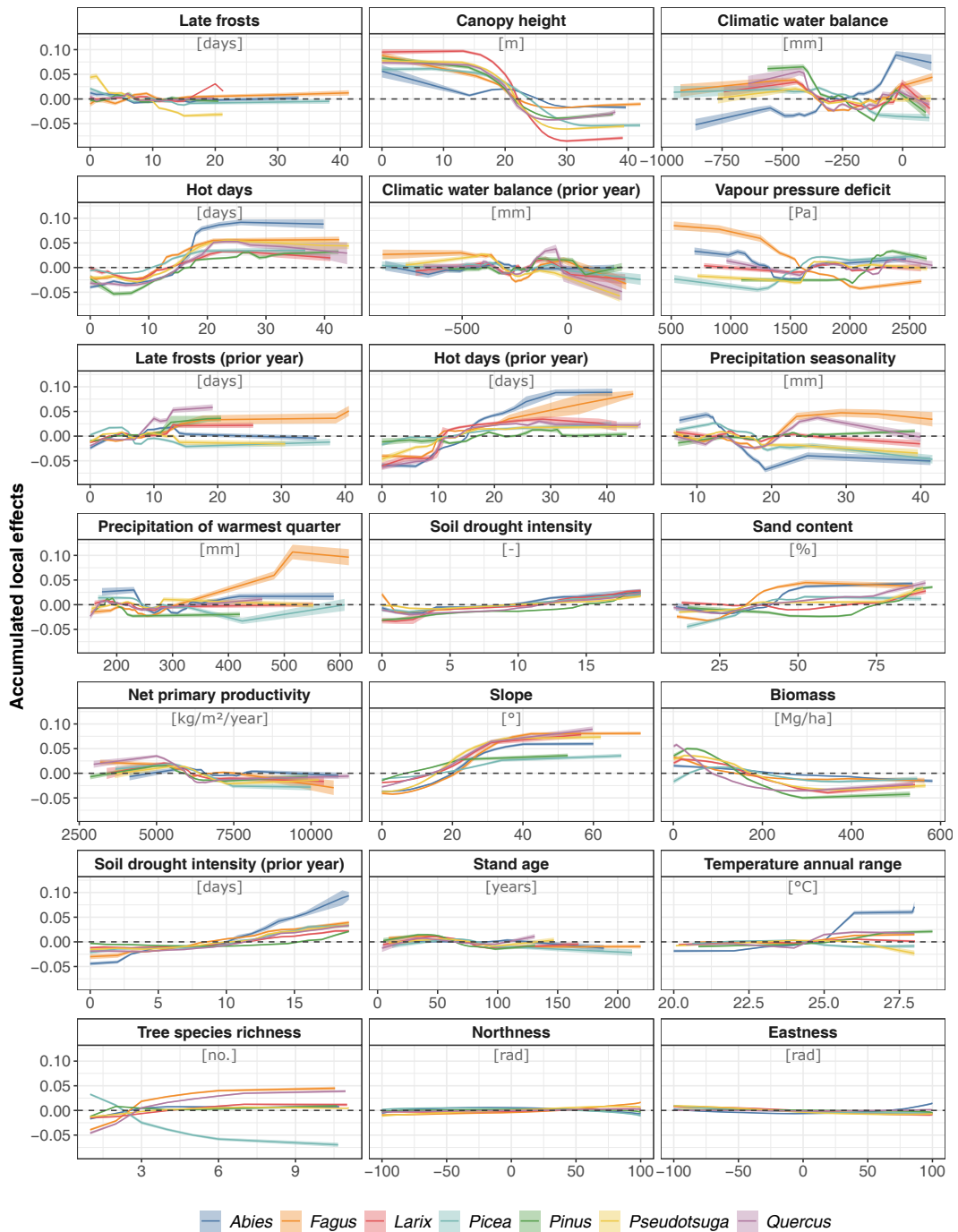


Figure 4.6: Accumulated local effect (ALE) plots for the 21 environmental predictor variables in descending order based on variable permutation importance. A positive value on the y-axis means contributing to more standing deadwood, negative values to less. ALEs are depicted separately for the seven main tree species (*Abies*, *Fagus*, *Larix*, *Picea*, *Pinus*, *Pseudotsuga*, and *Quercus*) in Germany. The solid lines show the mean effect across all repetitions, with the transparent ribbon denoting the standard deviation.

considerably higher for *Pinus* at 2.1 kPa compared to 1.5–1.7 kPa for the other four species. For *Abies* and *Fagus* a lower vapour pressure deficit was linked to more standing deadwood, and for *Fagus* a higher deficit even was linked to less standing deadwood. The effect of precipitation varied among the species with higher seasonality. *Picea*, *Pseudotsuga*, and *Abies* benefitted from higher precipitation seasonality and standing deadwood decreased, whereas standing deadwood for *Fagus* and *Quercus* increased. We observed increased mortality of *Fagus* in regions with a higher total precipitation during the warmest quarter. Higher soil drought intensities (both years) were linked to increased mortality, but the accumulated local effect was small. Only *Abies* experienced higher mortality rates than the other species when soil drought intensity of the year prior to dieback exceeded 10. The species showed different sensitivities towards sand content and its associated low water retention capacity. Whereas standing deadwood only increased at sand contents larger than 75% for *Picea*, *Quercus*, *Larix*, *Pseudotsuga*, and *Pinus*, higher amounts of standing deadwood were already observed at 30% sand content for *Fagus* and *Abies*. Lower net primary productivity and lower biomass were both linked to increased amounts of standing deadwood. Stand age showed only a small effect, with slightly increased mortality for younger stands. For the topographical conditions, slopes above 15° featured more standing deadwood, but the aspect components northness and eastness had no clear effect. For *Larix*, *Pseudotsuga*, *Pinus*, and *Abies*, tree species richness had no clear effect. A higher tree species richness was linked to more standing deadwood for *Quercus* and *Fagus*. *Picea* showed a contrasting effect, with less standing deadwood in more diverse forests.

4.4 DISCUSSION

4.4.1 PATTERN OF TREE MORTALITY IN GERMANY

The 2018–2021 summer droughts resulted in excess tree mortality rates in large parts of Central and northeastern Germany. Compared to the nationwide forest condition survey (BMEL, 2023), both assessments reveal a legacy effect, with standing deadwood only increasing sharply in the second consecutive drought year in 2019. However, our results indicate overall higher amounts of standing deadwood and an earlier increase in dieback after the 2018–2021 summer droughts. Whereas in 2018 the official statistics from the forest condition survey report 0.51% of standing deadwood in Germany (BMEL, 2023), our analysis resulted in $1.4 \pm 1.0\%$. In 2019, this percentage already increased to $2.5 \pm 1.4\%$ (for the single year) in our analysis, but only 0.9% (accumulated) in the survey. The steep increase in standing deadwood in 2020 was also mirrored in the forest condition survey with 2.25%, while our analysis revealed $2.6 \pm 1.3\%$ standing deadwood.

The highest percentage of standing deadwood in the forest condition survey is reported in 2021 with 2.35% in contrast to the $1.3 \pm 0.6\%$ found in our study.

We suspect several reasons for the differences between our analysis and the forest condition survey: Firstly, the forest condition survey is based on observations of individual dead trees ($n = 9,688$ from 402 sample plots according to BMEL, 2023) and is reported on the total number of trees in the survey. Whereas a large number of small individuals that were not affected by mortality might result in lower estimates of the forest condition survey, larger tree individuals might have an overly large impact on the cover value from the remote sensing perspective. Therefore, a direct comparison of this individual tree-based survey with the area-based remote sensing analysis is hampered. Secondly, the differences may be explained from the different perspective, as remote sensing data assesses tree mortality patterns from the bird's-eye perspective, while the forest condition survey data is recorded from the ground. The upper parts of the canopy are subject to higher levels of solar radiation, increased atmospheric coupling and long water conduits to the canopy and are, hence, particularly susceptible to dieback. The upward looking perspective of the forest condition survey can impede the view of this upper canopy (e.g., due to crown overlap and dense undergrowth) and result in an underestimation of standing deadwood. Lastly, our estimates of standing deadwood from Schiefer et al. (2023a) do not necessarily include only tree individuals but also partially dead tree crown or branches, which may result in higher estimates of standing deadwood.

Our observations of the temporal patterns confirm the findings of Thonfeld et al. (2022) and Global Forest Watch (GFW, 2023; Hansen et al., 2013). However, with 978 ± 529 kha from 2018–2021, our results suggest almost twice the amount of standing deadwood compared with 501 kha mapped by Thonfeld et al. (2022) and 543 kha mapped by the Global Forest Watch (GFW, 2023; Hansen et al., 2013). Although both products do not explicitly map tree mortality but also include other sources of forest loss, for example logging and windthrow, they detect considerably less forest loss. Thonfeld et al. (2022) used Sentinel-2 and Landsat 8 time series and calculated anomalies in the disturbance index. Index-based approaches circumvent the need for training data for supervised mapping approaches, but at the same time become hard to validate and interpret. The coarser spatial resolution of Landsat 8 (30 m) together with a binary classification (dead, not dead) does not fully reveal the scattered nature of canopy dieback and might hence lead to an underestimation of tree mortality (Cheng et al., 2024). Likewise, the forest loss maps from the Global Forest Watch (GFW, 2023; Hansen et al., 2013) also rely on the 30 m Landsat data and accordingly do not detect small-scale patterns, e.g., single dead tree crowns or patches thereof, and hence might underestimate forest loss (Galiatsatos et al., 2020; Hartmann et al., 2018b). The observed increase in accumulated standing deadwood in Germany peaked in 2019 and 2020 (see Figure 4.3), one year after the consecutive drought years

of 2018 and 2019 (Schnabel et al., 2022; Schuldt et al., 2020). The subsequent decrease in standing deadwood can be attributed to lower mortality rates in the following years. The produced maps exclusively depict standing deadwood. The decline can therefore also be attributed to the falling of dead parts of the tree crown or windthrow as natural causes. Anthropogenic causes include the removal of standing dead trees, which is a common forest management practice to prevent spreading of pest insects or to save timber values (Weslien et al., 2024).

Deviations from the standing deadwood cover fractions with other remote sensing products or field-based surveys may also stem from biases of the standing deadwood map used in this study. For example, we observed that sometimes the product of Schiefer et al. (2023a) overpredicted tree mortality near forest edges, roads, and paths. Another potential source of overestimation in our study is the shallow crown of some species, such as *Pinus*. Especially under dry conditions, the forest floor showing through the sparse canopy might be interpreted as a standing deadwood signal. Insect infestation can also lead to defoliation (Haynes et al., 2014; Skrzecz et al., 2020), which further thins out the crown, but the trees subsequently recover. This may be particularly true for the *Pinus*-dominated northeastern parts of Germany, and is reflected in the large standard deviation of standing deadwood from the sensitivity analysis of the different thresholds (see Figure 4.3).

The respective region was not recorded as being so severely affected by Thonfeld et al. (2022). However, for coniferous species the authors excluded pixels with NDVI values smaller than 0.5 from the analysis, which might underestimate standing deadwood in the case of *Pinus*, as the NDVI of *Pinus* is generally not very pronounced. We found coniferous species to show much higher rates of tree mortality, especially *Pinus* and *Picea* but also *Pseudotsuga*, compared to deciduous species. In the underlying tree species map (Blickensdörfer et al., 2024), *Pseudotsuga* and *Abies* showed the lowest accuracies (User's accuracy 37.07 ± 1.33 for *Pseudotsuga* and 24.65 ± 1.95 for *Abies*) and were often confused with *Picea*. Therefore, standing deadwood of *Pseudotsuga* and *Abies* is likely to be overestimated in our analysis. In our assessment, conifers often died back over larger areas in a short timespan, while for deciduous species smaller patches of standing deadwood accumulated over the years. This assessment matches our observations from the field, where broadleaved species usually showed gradual dieback of the canopy (i.e., dieback of single branches or parts of the crown), whereas coniferous species tended to die completely at one point in time.

4.4.2 ATMOSPHERIC CONDITIONS AS MAIN DRIVER OF TREE MORTALITY

We identified atmospheric conditions (i.e., late frosts, climatic water balance, hot days, and vapour pressure deficit) to be the most important predictors of tree mortality. The most important variable was late frost, although the accumulated

local effect was small. One reason for this may be that late frosts tend to have a large effect at a local level and are hence very important, but do not constitute a universal effect across the whole of Germany. Late frost occurs when tree buds have burst and leaves sprouted after spring warming, followed by temperatures well below zero. Late frosts often occur locally, which might explain the small accumulated local effects in our large-scale analysis. Especially for *Quercus* and *Fagus* (but also *Pinus*), more late frosts were associated with more standing deadwood. In the future, it is expected that late frosts will increase as a result of climate change (Vautard et al., 2023), putting vast areas of broadleaved trees at particular risk, given they are more susceptible to late frost events than conifers (Fisichelli et al., 2014).

Our results on the importance of the respective environmental variables (see Figure 4.5) confirm the importance of hotter droughts, in which atmospheric drought is accompanied by heat (Allen et al., 2015; Hartmann et al., 2022), for tree mortality during 2018–2020. Soil conditions were not as important as atmospheric drought and high temperatures. During drought, some tree species can compensate for water loss and prevent the death of plant material through various mechanisms (McDowell et al., 2022). Under simultaneous heat and drought, i.e., hotter droughts, negative impacts are aggravated because of greater atmospheric demands (higher vapour pressure deficit) and greater soil moisture limitations (Grossiord et al., 2020; Hartmann et al., 2022). In the first drought year in 2018, the trees already suffered damages (Schuldt et al., 2020) and thus started with significant abiotic and biotic legacies, such as depleted soil water reservoirs and damages to the tree’s water transport system (McDowell et al., 2022), into the consecutive drought years 2019 and 2020. These legacies likely induced the pronounced increases in tree mortality we observed during the subsequent drought years. Similarly, tree growth and physiological stress responses were found to be even more pronounced in 2019 than in 2018 as a result of such abiotic and biotic legacies (Schnabel et al., 2022). The predicted increase in such consecutive and hotter droughts (Hari et al., 2020) will likely further increase the risk for forest dieback events in the future.

4.4.3 MIXED EFFECT OF FOREST COMPOSITION AND STRUCTURE

4.4.3.1 *Canopy height and stand age*

Canopy height was the second most important variable based on random forest permutation importances, with a consistent effect across all species that smaller trees showed greater mortality and were more affected than tall trees. The same trend but with lower absolute accumulated local effect was found for stand age, where younger stands had higher mortality than older stands. Lower canopies would be rather young and dense stands, whereas higher canopies are often

structurally more diverse. Competition may be more severe in young stands, and additional constraints on resources may create severe shortages in many trees, ultimately resulting in increased mortality. In our study, we cover all forest management types across Germany, including naturally grown forests and plantations. We assume plantations with young and small stands to be exceptionally prone to competition-induced tree mortality, which might amplify mortality risks. These findings are consistent with Kulha et al. (2023) who examined mortality risks using national forest inventory data across Germany. Our results indicate that competition among younger and lower stands contributed more to the tree mortality pattern observed, and hence, that the effect of canopy height alone is smaller than found in other studies, where tree height largely explained mortality risks during droughts leaving especially larger trees at risk due to hydraulic vulnerability (Bennett et al., 2015; Gora & Esquivel-Muelbert, 2021; Stovall et al., 2019, 2020). Stovall et al. (2019, 2020) argue, that the intensity of an intrinsic height-mortality relationship is controlled by other factors, including environmental gradients of temperature, water, or competition. Based on our results, this height-mortality relationship would be reversed. Instead, we rather observe a mixed effect of forest composition and structure—including height. This observation supports findings by Stephenson and Das (2020) who found mortality to be more dependent on height-related changes in forest composition, rather than an intrinsically higher vulnerability of higher trees.

4.4.3.2 Site productivity and biomass

With increasing atmospheric CO₂ concentrations, increasing average temperatures, and a longer growing season in the future, an increase in forest productivity is expected (Lindner et al., 2014; McDowell et al., 2020). Higher site productivity increases growth rates of trees and may induce a higher susceptibility to embolisms and hydraulic failure during drought conditions (Pretzsch et al., 2018). At the same time, older trees usually have a reduced plasticity to changing environmental conditions and higher biomass that comes with higher maintenance costs, reducing soil water availability faster and therefore increasing drought stress and mortality risk (Jump et al., 2017). Consequently, Socha et al. (2023) found older and highly productive stands to be more susceptible to drought-induced tree mortality in *Pinus* dominated stands in Poland. In contrast, our results showed that a higher net primary productivity and a larger biomass decreased tree mortality. However, the different spatial resolutions of the input data should be considered when interpreting these results. Whereas standing deadwood was resolved at 10 m and tends to represent individual trees, the biomass (100 m) and net primary productivity (500 m) layers show averaged values at the stand level. Results from local-level studies are consistent with the mechanistic explanation for the mortality of taller, older and more productive tree individuals. However, this effect appears

to be mitigated at the landscape level, as the few large tree individuals do not contribute as much to productivity as the many young trees that grow back. Older and more productive stands therefore coped better with the observed prolonged and repeated hotter droughts. On average, these stands were therefore better adapted to extreme climatic conditions, for instance due to a deeper root system or greater water storage capacity, which can mitigate drought effects.

4.4.3.3 *Tree species richness*

The effect of tree species richness on tree mortality remains debated. In general, former studies on tree species richness effects on mortality yielded mixed results, with some species profiting from diversity and others not, depending on their functional traits (Blondeel et al., 2024; Depauw et al., 2024; Liu et al., 2022; Searle et al., 2022). For instance, Hajek et al. (2023) reported both synergistic tree species interactions in mixtures depending on the examined species during the 2018 hotter drought in an experimental setup. Across Germany, a higher degree of conspecific neighbours was recently shown to increase mortality risks relative to heterospecific neighbours using national forest inventory data in a study by Kulha et al. (2023). Here, we found that a higher tree species richness was not linked to lower tree mortality for most species and that tree species richness was generally less important than abiotic predictors and canopy height for explaining mortality patterns. However, the two broadleaved species *Fagus* and *Quercus* experienced higher mortality with increased tree species richness. One may speculate that the increased tree mortality for these species in mixed forests is caused by a higher competition for water in more productive mixed stands (Bauhus et al., 2017). However, our purely observational approach does not allow testing this assumption or rule out a potential confounding of this diversity effect with other abiotic variables, which would require explicit comparisons of mixtures with all of their constituent monocultures under comparable site conditions (see Baeten et al., 2013; Depauw et al., 2024). Therefore, future studies should aim to decipher the mechanisms that caused the increased mortality rates of *Fagus* and *Quercus* we observed. In contrast, *Picea* benefited from more diverse forest stands, and we observed larger amounts of standing deadwood in monocultures.

There is ample evidence that species mixing reduces the effect of specialist pests and pathogens (Jactel et al., 2021; Messier et al., 2022). Especially for *Picea* the reason for large-scale die-off is therefore the interaction of drought stress and bark beetle outbreaks, which can only propagate to this extent in vast monocultural stands. *Pinus* is also often planted in monocultures in Germany and died over extensive areas during 2018–2021. In contrast to *Picea*, however, the diversity of tree species was not related to mortality, presumably due to the regional lack of specialized pests. Stephenson et al. (2019) also highlighted this effect and found the combined effects of the presence of specialized bark beetles and drought

stress to greatly increase tree mortality. Despite the current absence of specialized pathogens and pests for some tree species, under changing climatic conditions, new specialized diseases are likely to spread and to put currently less affected tree species at risk.

4.5 CONCLUSION

Using a wall-to-wall remote sensing product with high spatial detail, we revealed almost twice as much standing deadwood in Germany during 2018–2021 than other sources, but different methodical approaches cannot be ruled out as reasons, for example, the different perspectives of satellite data and ground-based observations (such as the national forest condition survey), a high spatial detail of the employed remote sensing data that also captures scattered tree mortality, and an upscaling method based on actual observations of standing deadwood instead of index anomalies. In conclusion, remote sensing provides a valuable landscape-level view on tree mortality, complementing the insights on tree mortality processes we have from ground-based forest assessments. We found a complex interplay of environmental predictors, with extreme atmospheric conditions, i.e., hotter droughts but also late frosts, being the most important predictors for the observed tree mortality. The species' response varied greatly, and the revealed patterns provide important information for climate change adaptation. Mainly the coniferous species *Picea* and *Pinus* died, as they are not well adapted to hotter droughts. However, the extreme atmospheric conditions also put broadleaved species at risk, and particularly late frost events after vegetation onset played an important role in this respect. Our results showed that stand structure and composition influences tree mortality and, hence, that management of forest structure and composition can help mitigate the risks of global warming. Monocultures were particularly prone to mortality where pests interacted with drought. However, some species (*Fagus* and *Quercus*) also experienced higher mortality in more species-rich stands, an observation that warrants further investigations into unfavourable site conditions as a common reason for failure to achieve dominance and increased mortality but also into the trait-based mechanisms driving tree diversity effects on tree mortality at the stand and landscape scale.

Our results at the landscape level suggest that small, young stands contributed to more overall tree mortality in Germany due to competition for resources during extreme weather conditions than large tree individuals. Species information was crucial for interpreting patterns and predictors of tree mortality, and underlines the need for a heterogeneous database for upscaling local observations of standing deadwood to the landscape level. Adequate maps of standing deadwood are required, to gain insights on tree mortality processes at continental or global scales. This can only be accomplished if the scientific community contributes to the

collective gathering of reference data from multiple regions and biomes to improve the upscaling of standing deadwood observations from local-level to landscape-level, e.g., in initiatives such as www.deadtreatth.earth. Due to limited availability or limitations of computing power and models, environmental variables are often only considered as observations of points in time. The provision of corresponding time series data and the development of suitable models for investigating the complex spatio-temporal patterns should be advanced, considering the urgency of globally increasing tree mortality.

CREDIT AUTHOR CONTRIBUTIONS

Felix Schiefer: Conceptualization, Methodology, Software, Validation, Formal analysis, Data curation, Writing—Original Draft, Visualization. **Sebastian Schmidlein:** Supervision, Resources, Writing—Review & Editing. **Henrik Hartmann:** Writing—Original Draft, Writing—Review & Editing. **Florian Schnabel:** Writing—Original Draft, Writing—Review & Editing. **Teja Kattenborn:** Conceptualization, Methodology, Supervision, Writing—Original Draft, Writing—Review & Editing, Funding acquisition.

FUNDING

This work was funded by the German Aerospace Centre (DLR) on behalf of the Federal Ministry for Economic Affairs and Climate Action (BMWK) [FKZ 50EE1909A].

DATA AVAILABILITY STATEMENT

The data underlying this article (i.e., maps of standing deadwood in Germany) are available in the KITopen repository, at <https://dx.doi.org/10.5445/IR/1000158765>. Code for the conducted analyses is available on GitHub, at <https://github.com/FelixSchiefer/TreeMortalityPattern>.

SUPPLEMENTARY MATERIAL

Supplementary data is available at Forestry online.

CONFLICT OF INTEREST STATEMENT

None declared

5 Chapter 5

SYNTHESIS

Remote sensing lags far behind its potential for large-scale analyses of vegetation, mainly for two reasons: **(1)** suitable methods for harnessing the large volume of remote sensing data are missing and **(2)** a lack of ground reference data. Deep learning has emerged as one of the most promising methods to cope with large amounts of data, and its potential in remote sensing of vegetation has meanwhile been demonstrated in numerous studies. However, ground reference data is persistently lacking. As a result, deep learning in remote sensing of vegetation has not yet been fully explored. This thesis hence aims to overcome reference data scarcity and to further evaluate the potential of deep learning in vegetation remote sensing. In the first two studies, I addressed the question, whether deep learning algorithms are suited to efficiently analyse the dense information of current remote sensing data. While the first study focused on very high spatial resolution of uncrewed aerial vehicle (UAV) data (chapter 2), the second study also focused on temporally high resolved satellite image time series (chapter 3). From the results of the first study, I conclude that convolutional neural networks (CNNs) are ideally suited to harness the detailed spatial information of UAV imagery. This leads to the second research question, whether a concerted use of CNN and UAV is capable of closing the reference data gap on tree mortality. To address this question, I developed an approach to scale up UAV-based reference data to satellite level and investigated the potentials of this upscaling approach for the estimation of standing deadwood cover at landscape-level (chapter 3). In the final study, I investigated whether deep learning and the developed upscaling approach aid in identifying and understanding the environmental drivers of tree mortality at landscape-level (chapter 4)? In the following sections, I will synthesize the overarching insights from the three studies presented. I will highlight the potential of deep learning in vegetation remote sensing and how these techniques may contribute to an improved understanding of tree mortality. In conclusion, I will outline the critical challenges that must be addressed for the successful implementation of deep learning methods in vegetation remote sensing.

5.1 ADVANCING VEGETATION REMOTE SENSING WITH DEEP LEARNING ALGORITHMS

5.1.1 SPATIAL PATTERN EXTRACTION USING CONVOLUTIONAL NEURAL NETWORKS

Current remote sensing sensors provide large volumes of data with constantly increasing spatial, temporal, and spectral resolution. Handling this complexity requires efficient remote sensing methods to answer pressing ecological questions. With the use of UAVs, very high spatial resolution imagery are readily available. In the first two studies, I used CNNs to automatically segment and identify tree

species (chapter 2) and standing dead trees (chapter 3) from UAV-imagery. With an overall accuracy of 0.89 and an F1-score of 0.73 for the separation of 14 classes (i.e., nine tree species, three genera, deadwood, and forest floor) in the first study, I found CNNs to be particularly well suited to harness the dense spatial information of UAV-imagery. Supporting these findings, I found similarly good results in the second study, with an F1-score of 0.85 for the segmentation of standing deadwood. Both results were achieved using U-net CNN-architecture and on RGB-imagery only. Newer model architectures even resemble the textural representations on several hierarchical levels (i.e., atrous convolution) and may perform better than the fairly standard U-net. Both results are reported pixel-based at the original image resolution (i.e., <4 cm) and hence also comprise smaller artefacts, such as canopy gaps or crown overlap, that are also hardly semantically separable for any human interpreter. Due to their end-to-end learning capabilities and inference speed once a model is trained, CNNs are favourable over traditional machine learning methods or manual digitization for the interpretation of very high-resolution UAV-imagery.

CNNs even require the rich spatial detail provided by UAVs (chapter 2) when vegetation with only subtle features or differences thereof is being targeted. A lower spatial resolution, however, is sufficient for distinct features, such as prominent flowering, fruiting, or branching pattern. Administrative (e.g., flight permissions) and technical circumstances (e.g., battery capacity) limit the areawide coverage of UAVs and hence also the applicability for stand-alone large-scale tasks. This limitation suggests a transfer to orthoimagery acquired from aircraft, which features larger coverage and typically comes with a spatial resolution of 10 cm or above. Several studies used such aerial imagery to map (standing) deadwood (Jiang et al., 2019; Sani-Mohammed et al., 2022; Sylvain et al., 2019). Countrywide mapping of dead tree crowns over Luxembourg using aerial orthoimagery has successfully been demonstrated by Schwarz et al. (2023). As I have shown in the second study (chapter 3) CNNs are ideally suited for separating dead from live trees due to distinct visual features. If widely available, aerial imagery from aircraft is also suitable for mapping deadwood at the landscape-level (Schwarz et al., 2023). However, due to high acquisition costs and the time-consuming nature of aerial surveys, the temporal resolution is lower compared to satellite data. For other tasks, such as tree species classification, the spatial resolution of 10 cm alone would not suffice (chapter 2).

In conclusion, CNNs require a spatial resolution for some tasks that current satellite missions and aerial surveys do not provide. Undoubtedly, remote sensing data with very high spatial resolution is—regardless of the platform—currently not feasible for global applications, be it due to the limited spatial coverage or the disproportionate storage requirements. This highlights the necessity to employ and further investigate multimodal remote sensing approaches.

The end-to-end learning capabilities and flexible architectures of CNNs also ensure the extension of their application to the spectral domain. Due to high costs of data acquisition and complex data processing, hyperspectral data and studies using CNNs on hyperspectral data respectively are rare, but their results are promising (e.g., Fricker et al., 2019; Marconi et al., 2022). However, the number of trainable parameters of a CNN increases with each additional spectral band and with it the computational demand of the model and hence, its applicability. Computational demand is also an issue when tweaking a CNN for accuracy. As I have demonstrated in the first study (chapter 2), memory may be exhausted when a higher spatial resolution or larger tiles are used for CNN-training. Such technical constraints can be decisive for the successful utilization of deep learning in remote sensing analyses.

The size of the tiles that went into the CNNs was not *per se* decisive for the accuracy of the models. If there are no prominent features, smaller tiles better represent less frequent data points in the data set. Larger tiles are less prone to edge effects, resulting in smoother predictions. However, the maximum tile size is limited by the available memory. Consequently, a high computing power is required to conduct large-scale analyses and to uncover and explore ecological relationships at entire landscapes.

5.1.2 HARNESSING THE TEMPORAL DIMENSION WITH LONG SHORT-TERM MEMORY NETWORKS

This thesis demonstrates that CNNs are an ideal tool for extracting and processing spatial information from remote sensing data. CNNs are also a suitable means to exploit the spectral dimension of remote sensing data. The constant stream of high temporal resolution remote sensing data requires adequate data analysis methods. Convolutions are also employed to extract information from temporal signals (see for example Pelletier et al., 2019a), but some algorithms are specifically designed to analyse sequential data (i.e., RNN, LSTM, and transformer). In the second study (chapter 3), I therefore evaluated long short-term memory networks for harnessing the temporal dimension. I used an LSTM for predicting the fraction of standing dead trees per pixel from satellite image time series. The LSTM achieved good results, considering the subtle and dynamic nature of the tree mortality process studied. In comparison with a shallow machine learning approach (i.e., random forest), the LSTM achieved comparable Pearson's r and RMSE, but lower model bias. I tested several band input combinations from spectral information from Sentinel-2 bands, structural information from Sentinel-1 backscatter (CARD-BS) and interferometric coherence (CARD-COH6), and additional vegetation indices kNDVI and NDWI. The model with all available information performed best. The improved performance when including the vegetation indices contradicts the assumption that the end-to-end capabilities of deep learning approaches do not

require feature engineering. Nonetheless, the complexity of the data is high when several data types are incorporated. Since vegetation indices are often based on physical principle, incorporating such physical constrains facilitates the learning process. The length of the satellite image time series was restricted to two years, given that the ground truth data partly originate from the year 2018 and that Sentinel data only date back until 2016 with the operational mode of the satellites. This period may be too short for the model to learn typical vegetation dynamics and patterns, and covering more phenological cycles might improve the results.

In conclusion, LSTMs were well suited to analyse the dense temporal information from satellite image time series. LSTMs better accounted for the temporal dependencies in the data and were superior over a shallow machine learning approach. LSTMs are capable to analyse the remote sensing signal of vegetation that emerges from a complex interaction of biophysical and biochemical components and changes during the phenological cycle. With adjustments in the temporal and spatial matching of the ground reference data (see next chapter), improved models, and longer time series deep learning approaches can be expected to further improve.

5.2 LEVERAGING DEEP LEARNING FOR COMPREHENSIVE LANDSCAPE-LEVEL ANALYSES

In the previous section, I highlighted the possibilities of deep learning for extracting data representations for vegetation analyses from the spatial, spectral, and temporal dimensions of remote sensing data. CNNs are a powerful tool to extract spatial pattern from image data and LSTMs to extract sequential information from satellite image time series. Very high-resolution imagery from UAVs alone is sufficient for studies with a local focus, but not suited for large-scale tasks due to the limited spatial coverage. Deep learning-based *downscaling* approaches, may incorporate the temporal information from satellite imagery available over large areas. An example of such a downscaling approach are multi-branch architectures, where one branch is trained with high-resolution image data while another branch processes temporal information from satellite data time series. The learned features from both branches are jointly interpreted in the decision layer, thereby enhancing predictions compared to singular models (see, for example, Labenski et al., 2023). However, the limited coverage of the high-resolution imagery still constrains downscaling models for area-wide inference. Repeatedly acquired multispectral aerial orthoimagery is more extensively available, but I showed that the spatial resolution provided restricts its application only to tasks with clearly discernible features of vegetation (chapter 2). Depending on the platform, satellite data has a high temporal resolution but an insufficient spatial resolution for CNN-applications (i.e., 10 m of Sentinel-2 or 30 m of Landsat). Other satellite

platforms offer higher spatial resolutions (i.e., Dove constellation with 3 m) but the same limitations as for aerial orthoimagery apply.

Integrating the various data sources and harnessing the different resolutions in an holistic approach remains an open challenge in remote sensing of vegetation. Large-scale remote sensing of vegetation is deemed to stay behind its potential when only one of the data sources is utilized—even for deep learning methods. This is merely an issue of deep learning itself and not restricted to global but also regional scales. Rather, it all boils down to the lack of the necessary reference data. At the global scale, we are not yet there in terms of reference data availability to fully exploit the potential of deep learning.

5.2.1 INTEGRATING MULTIDIMENSIONAL REMOTE SENSING DATA

One of the most promising avenues in this regard is the integration of different dimensions and data sources of Earth observation data, enabled by the flexible architecture of deep learning models. The various specialized deep learning layers can be linked together and enable simultaneous analysis of several dimensions. For instance, convolutional long short-term memory networks (ConvLSTM) as proposed by Shi et al. (2015). A ConvLSTM replaces the internal matrix multiplications in an LSTM with convolutions, thereby propagating spatial data representations through the temporal dimension. ConvLSTMs can hence learn spatio-temporal data representations. They were first introduced by Shi et al. (2015) for short-term prediction of future precipitation from spatio-temporal radar intensity maps. Not only did this approach accelerate model prediction over large areas due to the patch-based inference, but also outperformed a standard, pixel-based LSTM. ConvLSTMs have been adapted for remote sensing of vegetation: Ahmad et al. (2023) used a ConvLSTM for predicting NDVI from MODIS satellite data to estimate crop growth and yield. Li et al. (2023) tested different levels of integration of spatial and temporal information for classifying crops from Sentinel-2 images. Rußwurm and Körner (2018) and Shen et al. (2021) mapped land cover types from Sentinel-2 and Landsat 8 time series respectively. Results of the studies indicated that spectral-spatial image data were more important than temporal information (Li et al., 2023; Shen et al., 2021) and through the end-to-end learning capabilities cloud coverage could be learnt jointly with the classification task (Rußwurm & Körner, 2018; Shen et al., 2021). Regarding the length of the time series, longer series were conducive for model accuracy (Shen et al., 2021). The unanimous result of the studies was a better model performance the more dimensions were integrated. However, field crops are typically grown in clearly defined, homogeneous entities and an application of ConvLSTM for vegetation assessment in more heterogeneous and dynamic environments, such as tree mortality, is yet to be tested.

Convolutional neural networks (CNNs) are mostly used on RGB images but are not restricted in their number of input bands. The number of input layers can be extended to match the number of bands from hyperspectral images to extract spatial pattern along single bands in the electromagnetic spectrum. In a transposed form, CNN interpret the hyperspectral signal pixel-based in a sequential manner (e.g., see Cherif et al., 2023, who simultaneously derived 20 plant traits from hyperspectral canopy spectra). Both applications only learn data representations from one of the dimensions. Harnessing both the spatial and spectral domain simultaneously can be accomplished in a spatio-spectral approach also using ConvLSTM (e.g., Hu et al., 2020; Wang et al., 2021, for land use land cover classification of hyperspectral images). The developed models with spatio-spectral feature extraction show the highest accuracies on benchmark datasets. Such benchmark datasets often deal with the classification of settlement areas or field crops that feature clear boundaries and little to no class transitions. They provide a valuable contribution to the development of new model architectures, but studies often do not go beyond pure laboratory studies. The transition from the spatially, temporally and spectrally relatively static tasks on benchmark datasets to dynamic vegetation processes has yet to be done.

5.2.2 CLOSING THE REFERENCE DATA GAP ON TREE MORTALITY

In this thesis, I presented an *upscaling*-approach from the UAV to the satellite scale. The approach was successful in closing the reference data gap on tree mortality. The foundation of the approach is the automated CNN-based segmentation of very high resolution UAV-imagery, which I explored in the first two studies (chapter 2 and 3). The actual upscaling happens in the subsequent step, where the CNN-predictions serve as reference data for an LSTM to predict the pixelwise fraction of standing dead trees from satellite image time series. Advantages of this upscaling approach are manifold. So were the data representations learned by the CNN good enough for rapid generation of ample reference data over wide areas. With heterogeneous input data, the degree of generalization of CNNs is high and the model can be applied to unseen data once it is trained. The use of UAVs facilitates the acquisition of reference data even in previously inaccessible terrain. Moreover, this reference data is collected from a shared perspective with satellite data, and hence, gives it matching geometric properties. These data are spatially explicit and directly applicable as ground reference.

Several criteria must be met for successful upscaling. The geolocation errors of both UAV and satellite data as well as the structure from motion processing step for UAV-data may cause relative positional inaccuracies that exceed the spatial resolution of satellite data. The positional accuracy is usually known, and the spatial matching must be subsequently optimized if necessary. Automated co-registration methods, such as scale-invariant features transform (SIFT), are not feasible in that

case due to the very different spatial resolutions. A simple optimization method may suffice that resamples the UAV-imagery to the satellite data and iteratively shifts and rotates the UAV data to find the maximum correlation of the spectral bands available in both datasets. I tested such an optimization in the second study, but results were inconclusive (chapter 3). Potential reasons for this were a mismatch between UAV acquisition time and satellite overpass and the resulting differences in lighting situation, such as cast shadows. This already illustrates the second premise for the upscaling approach, namely temporal alignment. As described above, the temporal alignment in the diurnal cycle rather affects the spatial match (because of shadowing effects), while a temporal alignment in the annual cycle is critical for phenology-related vegetation status. When the raw image data (e.g., spectral reflectance) and not derivatives thereof (e.g., segmented tree crowns) shall be used, also a spectral registration needs to be considered, but these applications are seldom.

Finally, the spatial and temporal transferability of the CNN used for creating the reference data is important and can ultimately be attributed to two factors: deep learning capabilities itself (see section 5.1) and a large and heterogeneous data set. The data set in this thesis comprises UAV imagery from 176 individual sites with at least 1 ha coverage distributed over six study regions in Germany and Finland. It includes several forest types under different managements with varying species mixtures. UAV data were acquired in the years 2017–2021 using two different sensors and a ground sampling distance of 0.65–3.39 cm. With this data set, spatial and temporal transferability of the deep learning models could be shown in this thesis. In conclusion, the concerted use of UAV-based RGB-imagery and CNNs was capable of ending reference data scarcity on tree mortality in Germany. Its application is not limited to tree mortality, but is generally suitable for scaling local observations to landscapes. For the integration of UAV and satellite data, spatial and temporal consistency of the data sources is key. Focus should be on the collection of a large and heterogeneous data set with a diversity of vegetation structure, vegetation types, backgrounds, focal views, and resolutions, thereby ensuring model transferability.

5.3 ENHANCED UNDERSTANDING OF TREE MORTALITY BY LANDSCAPE-LEVEL ANALYSES

Information on tree mortality at the landscape level is crucial as it forms the basis for estimating biomass and contributes to climate modelling. Nationwide statistics on tree mortality are collected annually in Germany through the national forest condition survey, and an increase in standing deadwood has been observed since 2019. Since the survey is based on the sampling of approximately 10 000 individual trees from 402 systematically distributed field plots, landscape-level

interpretations of the statistics may be flawed. Landscape-level assessment of tree mortality using remote sensing methods is no novelty and has been demonstrated in numerous studies (e.g., Brodrick & Asner, 2017; Byer & Jin, 2017; Hansen et al., 2013; Thonfeld et al., 2022). Due to the coarser spatial resolution (i.e., 30 m or above) and the lack of explicit reference data on dead trees, it is difficult to make accurate estimates of small-scale and scattered occurrences of deadwood, and therefore mortality is likely underestimated (Cheng et al., 2024). Hence, it is not surprising that with the approach presented here, which utilizes spatially explicit reference data and a higher spatial resolution (10 m), I found twice the amount of deadwood in Germany during 2018–2021 compared to the forest condition survey and other remote sensing methods. The spatial and temporal patterns found were consistent with other surveys. Overall, the results do not contradict each other; rather, they demonstrate that the method presented here can provide complementary and more detailed insights, but also that tree mortality in Germany is more severe than previously thought.

Several mechanisms that have been identified as causal for tree mortality at the individual tree level from field-based studies have not been investigated or confirmed at the landscape-level (McDowell et al., 2022). While, for example, small and young trees are subject to increased competition for resources (Kulha et al., 2023; Stephenson & Das, 2020), large and old trees have an elevated mortality risk due to accumulated damage (Bennett et al., 2015; Stovall et al., 2019, 2020). For comprehensive accounting of tree mortality at the landscape level, the impact of both processes is crucial, and my analyses revealed that there was an increase in mortality among smaller (younger) stands. The influence of tree species richness is also not generically understood. While many studies have found a generally positive effect of tree species richness on reducing mortality (cf. Anderegg et al., 2018; Schnabel et al., 2021), analyses of extensive forest inventory data in North America revealed increased mortality with rising tree diversity (Searle et al., 2022). Results from this thesis support the latter, and increased tree mortality was observed in more species-rich stands. But, monocultures were particularly prone when specialised pests interacted with drought. Even though the results of this purely observational approach should not be overinterpreted, they clearly show that the mechanisms identified at the local level may manifest differently at the landscape level. While forest management towards heterospecific stands might foster productivity (Anderegg et al., 2018; Schnabel et al., 2021) and thus higher carbon sequestration, this effect might be inverted when tree mortality increased during drought.

5.4 OUTLOOK

With the recent technological advancements and the development of appropriate hardware, deep learning has become a valuable tool in remote sensing. It holds great potential for detecting vegetation patterns and changes from Earth observation data and outperforms shallow machine learning through a range of features, such as flexible model architectures, end-to-end learning, convolutions for extracting spatial patterns, and recurrence for extracting temporal patterns. This thesis showed some great potentials of deep learning in remote sensing of vegetation, either in stand-alone local-level studies, as a tool for reference data generation or for satellite image time series interpretation. I further presented an upscaling approach capable of landscape-level applications. There are still several challenges to fully realize the potential of deep learning in vegetation remote sensing, including, for example, integration of data and dimensions, processing environment, and data sharing. In the following, I will address some key points in that regard.

CLOUD COMPUTING AND EO FRAMEWORKS

The surge in publications on the subject of deep learning in remote sensing of vegetation highlights the relevance of the topic and the necessity to fully utilize the available *big* data. Deep learning offers fundamental features that improve the extraction of vegetation patterns from remote sensing data (see section 5.1) but the integration of the individual components has yet to be refined.

As I could show in this thesis, deep learning provides the appropriate tools to extract the spatial, temporal, and spectral information from remote sensing data to provide insights into vegetation and its condition. In the era of big data, the availability of remote sensing data is no longer a limitation and deep learning methods can be used to provide reference data for large-scale analyses. Access to the large amounts of data is provided by cloud platforms. This has laid the groundwork, but the challenge is to bring together deep learning and big data for vegetation monitoring. To concentrate on ecological questions, several challenges need to be solved. The handling of large volumes of remote sensing data should become more user-friendly. Satellite data is available in various processing levels, generated by different processors, and is available on different platforms with varying degrees of timeliness. Depending on the platform, access from raw data to analysis-ready data can be provided. The pre-processing steps are not always sufficiently documented or cannot be controlled, which is a basic requirement for reproducible research. While such data cubes are sufficient for some applications, the process chain must be controllable and reproducible for research purposes. In this work, *ForceEO* (Frantz, 2019) was used for this purpose. There are several alternative applications, but no general standards, and focus should therefore be

on simplification and the development of community standards (e.g., *openEO* API, <https://openeo.org>).

In the present thesis, remote sensing based upscaling and ecological modelling using environmental predictors were separated into two models. By the flexible architecture of neural networks, different data types and sources can also be intertwined in one model. The increased information content may improve the models, but requires the processing of the corresponding data within the same framework. This integration of additional explanatory, non-remote sensing data must therefore also be ensured. To adhere to the principle of “bringing users to the data, rather than data to the user”, the deep learning models must also be able to run on a remote machine or a cloud environment. In addition to the corresponding software, the high computing power requirements of the more complex architectures must be met.

TOWARDS OPEN DATA, CODE, AND MODELS

To answer urgent ecological questions with the methods of remote sensing, four criteria must be met: **(1)** availability of suitable remote sensing data, **(2)** comprehensive and meaningful environmental data with high temporal and spatial resolution, **(3)** suitable methods for evaluating the data and **(4)** suitable reference data. In the era of big data, remote sensing data with different spatial, temporal and spectral resolutions is available. The general suitability of deep learning for the analysis and interpretation of multidimensional remote sensing data could be demonstrated in this thesis. Furthermore, this thesis presented an upscaling method capable of generating sufficient reference data. Two initiatives that have already adopted or pursue this upscaling idea are *MillionTrees* (<https://milliontrees.idtrees.org>) that attempts to collect one million annotations of trees in RGB imagery and *deadtrees.earth* (<https://deadtrees.earth>) that curates an open database for remote sensing tree mortality data. Such data sharing initiatives are an identified necessity (Hammond et al., 2022) for the collection of the large amounts of data needed for global tasks. They also enable the collection of very heterogeneous data from different sensors, with different resolutions, focal views, vegetation types and structure, backgrounds, etc., which are important for the generalisation and transferability of models (Weinstein et al., 2020). Without these real-world data sets, gaining insights from remote sensing data for large-scale ecological questions will stagnate. In contrast to ecological theory, progress in the development of deep learning methods thrives on trial and error. By curating and providing such datasets, new deep learning architectures can be tailored directly to the needs of ecology in a way that would not be possible with the existing and rather technical benchmark datasets. Due to this need, I have published my data including tree annotations in the two data sets *FORTRESS* (Schiefer et al., 2022a) and *FORTRESSdead* (Schiefer & Kattenborn, 2024). For ease of reproducibility,

the developed code from the three studies is also published at <https://github.com/FelixSchiefer/TreeSeg>, <https://github.com/FelixSchiefer/TreeMortality>, and <https://github.com/FelixSchiefer/TreeMortalityPattern>.

Data sharing also creates opportunities to develop new approaches that would not be possible with solitary data sets and without cooperation. For example, linking citizen science plant photographs from the *iNaturalist* database with trait information from the *TRY* database for trait mapping at global scale (Schiller et al., 2021; Wolf et al., 2022). Or transfer learning from *iNaturalist* plant photographs to UAV-imagery for comprehensive mapping of (invasive) plant species (Soltani et al., 2022). These experimental studies highlight the potential that shared datasets can offer and showcase the strengths of combining big data and deep learning for insights on global patterns of vegetation.

A new form of sharing that is particularly effective for deep learning approaches is the sharing of pre-trained networks or weights. Unlike machine learning approaches, it may be useful to pre-train the networks on generic data. In this way, basic features such as corners, edges, or abstract shapes are already learned, and the models perform better when applied to a particular task. Transfer learning, i.e., the transfer of pre-trained networks, improves model accuracies and is already common practice. The collection of data, as the initiatives described above do, again increases the volume of remote sensing data by copying the data. A promising approach to minimize this data stream and volume is federated learning, where the data remains decentralized, and the network is also trained decentralized in different nodes on multiple machines. As the data remains local, licensing and data privacy issues can be avoided. Such a decentralized approach is an ideal complement to the existing cloud platforms on which the satellite data is stored.

Future efforts should therefore focus on building a framework that brings together the important components of remote sensing: the framework should cover the access and processing of satellite data time series, the integration of explanatory environmental variables, the provision of reference data or the methods to generate suitable reference data, and methods for the integrated interpretation of spatially, temporally and spectrally multidimensional remote sensing data. Emphasis should also be given to user-friendliness and access under the *FAIR* principles (i.e., findability, accessibility, interoperability, and reusability, Wilkinson et al., 2016) to make remote sensing of vegetation accessible to a wide audience. Cloud computing platforms and resources, as well as federated learning, could be an integral part.

APPENDIX

APPENDIX A1

Table A1: CNN model results using three different cost functions: (1) categorical cross-entropy (CCE), (2) weighted CCE with inversely proportional weights according to the area-related share of the species, and (3) squared weighted CCE with squared inversely proportional weights. All results are based on a CNN with 128×128 pixel RGB + nDSM input tiles at 2 cm spatial resolution.

F1-Score	CCE	weighted CCE	squared weighted CCE
<i>Picea abies</i>	0.93	0.93	0.91
<i>Fagus sylvatica</i>	0.90	0.90	0.89
<i>Abies alba</i>	0.86	0.86	0.84
<i>Pseudotsuga menziesii</i>	0.90	0.89	0.89
<i>Pinus sylvestris</i>	0.89	0.91	0.90
<i>Acer spp.</i>	0.65	0.80	0.65
<i>Fraxinus excelsior</i>	0.86	0.87	0.32
<i>Larix decidua</i>	0.88	0.83	0.83
<i>Quercus spp.</i>	0.66	0.58	0.61
<i>Carpinus betulus</i>	0.38	0.38	0.53
<i>Tilia spp.</i>	0.37	0.50	0.17
<i>Betula pendula</i>	0.35	0.27	-
Forest floor	0.84	0.83	0.82
Deadwood	0.77	0.72	0.73
Mean F1-Score	0.73	0.73	0.65
Overall Accuracy	0.89	0.89	0.87

APPENDIX A2

Table A2: Site-specific F₁-Scores for the study regions Southern Black Forest (SBF), Northern Black Forest (NBF), Dresden Heath (DDH), Karlsruhe-Bretten (KAB), Hainich National Park (HAI), and Helsinki (FIN)

plotID	AOI	year	Tile size [pixel]						Spatial resolution [cm]				
			RGB			RGB + nDSM			RGB + nDSM				
			128	256	512	128	256	512	2	4	8	16	32
CFB003	SBF	2019	0.77	0.81	0.83	0.82	0.83	0.74	0.83	0.78	0.73	0.53	0.53
CFB008	SBF	2017	0.74	0.76	0.80	0.83	0.79	0.82	0.79	0.74	0.76	0.71	0.48
CFB014	SBF	2017	0.82	0.83	0.76	0.91	0.91	0.87	0.91	0.84	0.82	0.63	0.52
CFB019	SBF	2017	0.70	0.74	0.69	0.75	0.74	0.70	0.74	0.72	0.63	0.78	0.67
CFB021	SBF	2019	0.81	0.68	0.68	0.78	0.69	0.72	0.69	0.78	0.74	0.69	0.61
CFB030	SBF	2017	0.63	0.73	0.66	0.59	0.76	0.75	0.76	0.76	0.64	0.52	0.40
CFB031	SBF	2017	0.83	0.81	0.81	0.81	0.81	0.82	0.81	0.79	0.75	0.73	0.72
CFB035	SBF	2017	0.84	0.85	0.69	0.88	0.87	0.87	0.87	0.81	0.72	0.72	0.62
CFB037	SBF	2017	0.99	1.00	1.00	0.99	0.99	1.00	0.99	0.97	1.00	0.96	0.95
CFB044	SBF	2017	0.84	0.88	0.91	0.91	0.83	0.91	0.83	0.89	0.83	0.76	0.60
CFB045	SBF	2017	0.75	0.60	0.73	0.77	0.62	0.74	0.62	0.62	0.60	0.37	0.39
CFB050	SBF	2017	0.80	0.83	0.77	0.87	0.84	0.75	0.84	0.78	0.54	0.65	0.50
CFB053	SBF	2017	0.68	0.76	0.74	0.69	0.77	0.71	0.77	0.69	0.62	0.59	0.60
CFB056	SBF	2017	0.73	0.72	0.68	0.76	0.74	0.62	0.74	0.66	0.56	0.55	0.54
CFB057	SBF	2017	0.62	0.70	0.60	0.75	0.61	0.71	0.61	0.59	0.51	0.54	0.53
CFB061	SBF	2017	0.66	0.66	0.60	0.68	0.72	0.76	0.72	0.71	0.37	0.42	0.46
CFB071	SBF	2017	0.90	0.93	0.92	0.93	0.94	0.92	0.94	0.93	0.84	0.75	0.66
CFB073	SBF	2019	0.77	0.70	0.70	0.70	0.75	0.72	0.75	0.77	0.68	0.59	0.34
CFB084	SBF	2017	0.61	0.66	0.68	0.79	0.86	0.66	0.86	0.60	0.71	0.52	0.69
CFB085	SBF	2017	0.87	0.92	0.85	0.90	0.91	0.88	0.91	0.88	0.73	0.74	0.51
CFB089	SBF	2017	0.78	0.86	0.83	0.85	0.85	0.78	0.85	0.77	0.56	0.61	0.47
CFB091	SBF	2017	0.64	0.74	0.69	0.68	0.71	0.69	0.71	0.54	0.48	0.45	0.38
CFB096	SBF	2017	0.78	0.78	0.63	0.84	0.79	0.68	0.79	0.83	0.55	0.59	0.53
CFB106	SBF	2017	0.79	0.83	0.80	0.88	0.86	0.76	0.86	0.65	0.57	0.69	0.65
CFB110	SBF	2017	0.66	0.86	0.72	0.72	0.71	0.74	0.71	0.72	0.48	0.51	0.83
CFB111	SBF	2017	0.82	0.85	0.58	0.72	0.82	0.63	0.82	0.60	0.58	0.69	0.49
CFB114	SBF	2019	0.68	0.70	0.59	0.76	0.69	0.64	0.69	0.64	0.53	0.64	0.36
CFB117	SBF	2017	0.71	0.60	0.57	0.61	0.61	0.75	0.61	0.53	0.43	0.37	0.31
CFB121	SBF	2017	0.67	0.69	0.54	0.83	0.72	0.52	0.72	0.56	0.60	0.56	0.41
CFB122	SBF	2017	0.91	0.86	0.87	0.86	0.89	0.85	0.89	0.81	0.58	0.54	0.86
CFB124	SBF	2017	0.76	0.77	0.75	0.76	0.76	0.54	0.76	0.77	0.51	0.53	0.54
CFB125	SBF	2017	0.61	0.78	0.56	0.75	0.78	0.50	0.78	0.55	0.56	0.51	0.49
CFB128	SBF	2019	0.62	0.70	0.68	0.67	0.74	0.73	0.74	-	-	-	-
CFB129	SBF	2017	0.58	0.63	0.56	0.60	0.56	0.49	0.56	0.53	0.60	0.56	0.44
CFB130	SBF	2019	0.74	0.86	0.76	0.85	0.87	0.86	0.87	0.81	0.78	0.67	0.53
CFB133	SBF	2017	0.85	0.89	0.87	0.90	0.90	0.89	0.90	0.86	0.75	0.76	0.62
CFB134	SBF	2017	0.83	0.71	0.89	0.73	0.88	0.89	0.88	0.87	0.71	0.76	0.56
CFB140	SBF	2017	0.59	0.70	0.68	0.67	0.79	0.73	0.79	0.70	0.47	0.47	0.49
CFB151	SBF	2017	0.81	0.84	0.84	0.77	0.87	0.85	0.87	0.73	0.59	0.48	0.40

Table A2 continued from previous page

plotID	AOI	year	Tile size [pixel]						Spatial resolution [cm]				
			RGB			RGB + nDSM			RGB + nDSM				
			128	256	512	128	256	512	2	4	8	16	32
CFB153	SBF	2019	0.67	0.92	0.74	0.71	0.70	0.70	0.70	0.93	0.59	0.71	0.75
CFB156	SBF	2017	0.85	0.86	0.80	0.88	0.88	0.85	0.88	0.85	0.84	0.76	0.62
CFB162	SBF	2017	0.77	0.83	0.70	0.74	0.87	0.82	0.87	0.81	0.70	0.61	0.66
CFB163	SBF	2017	0.74	0.82	0.78	0.73	0.67	0.69	0.67	0.62	0.68	0.55	0.48
CFB167	SBF	2017	0.86	0.88	0.81	0.83	0.88	0.82	0.88	0.89	0.82	0.83	0.74
CFB171	SBF	2017	0.87	0.88	0.89	0.89	0.88	0.91	0.88	0.88	0.86	0.77	0.61
CFB173	SBF	2017	0.73	0.80	0.81	0.81	0.86	0.83	0.86	0.81	0.79	0.70	0.68
CFB184	SBF	2017	0.78	0.81	0.86	0.83	0.83	0.87	0.83	0.77	0.64	0.62	0.52
HA1038	NPH	2019	0.90	0.75	1.00	0.79	0.77	0.82	0.77	0.72	0.61	0.67	0.57
HA1039	NPH	2019	0.73	0.56	0.52	0.61	0.71	0.30	0.71	0.49	0.25	0.51	0.49
HA1040	NPH	2019	0.62	0.46	0.45	0.79	0.46	0.70	0.46	0.49	0.35	0.26	0.63
HA1050	NPH	2019	0.61	0.47	0.95	0.59	0.54	0.95	0.54	0.34	0.47	0.26	0.46
	Minimum		0.58	0.46	0.45	0.59	0.46	0.30	0.46	0.34	0.25	0.26	0.31
	1st Quartile		0.67	0.70	0.68	0.72	0.72	0.70	0.72	0.63	0.55	0.52	0.48
	Median		0.76	0.78	0.74	0.78	0.79	0.75	0.79	0.76	0.62	0.61	0.53
	Mean		0.75	0.77	0.74	0.78	0.78	0.75	0.78	0.73	0.63	0.61	0.56
	3rd Quartile		0.83	0.86	0.83	0.85	0.87	0.85	0.87	0.81	0.73	0.71	0.62
	Maximum		0.99	1.00	1.00	0.99	0.99	1.00	0.99	0.97	1.00	0.96	0.95

APPENDIX A3

For a qualitative inspection and to obtain a causal explanation for our results in terms of spatial resolution we visualized the filters learned by the CNN. This can be done by creating input images that maximize the activation of a specific CNN layer and thus contain the visual patterns that the respective filter is maximally responsive to. To obtain the filter visualizations we started from an all gray image with some random noise and calculated the mean activation of the selected filter in our target layer. Subsequently, we computed the gradients of this activation with regard to the input image and updated the image in a way that it would activate the selected filter more strongly. By multiplying the gradients with a learning rate of 10, we accelerated the generation of distinct visual patterns. We repeatedly applied this gradient ascent step for 60 times, which eventually resulted in the visualizations of the filters that maximize the CNN layer activations. (Figure 2.6)

APPENDIX A4

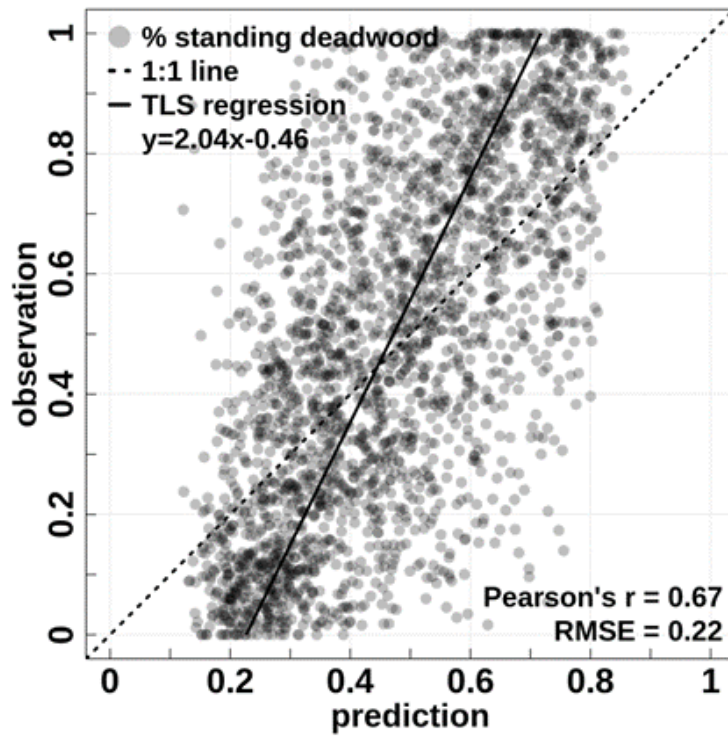


Figure A1: Scatterplot of observed fractional cover values of standing deadwood [%] and random forest model predictions (S_1+S_2+VI , 12 Sentinel-2 bands) from 5-fold cross-validation. Each dot represents a 10 m Sentinel-2 pixel with reference data available from the UAV scale. Pearson's r of 0.67 and RMSE of 0.22 are similar to the LSTM results. However, values close to 0 and 1 were poorly predicted, reflecting in a relatively high model bias with a slope value of 2.04 from the TLS regression.

APPENDIX A5

Table A3: Summary statistics for the sites from the six study regions Southern Black Forest (SBF), Northern Black Forest (NBF), Dresden Heath (DDH), Karlsruhe-Bretten (KAB), Hainich National Park (HAI), and Helsinki (FIN)

site	year	region	total area [ha]	dead-wood [ha]	dead-wood [%]	CNN precision	CNN recall	CNN F1	LSTM RMSE
CFB005	2017	SBF	1.98	0.018	0.009	0.979	0.885	0.929	0.151
CFB008	2017	SBF	2.06	0.078	0.038	0.871	0.632	0.732	0.186
CFB014	2017	SBF	1.81	0.006	0.003	0.971	0.595	0.737	0.165
CFB017	2017	SBF	0.96	0.004	0.004	0.980	0.927	0.953	-
CFB019	2017	SBF	1.86	0.010	0.005	0.984	0.707	0.823	0.112
CFB020	2017	SBF	1.10	0.020	0.018	0.934	0.758	0.837	0.155
CFB030	2017	SBF	2.09	0.000	0.000	0.000	0.000	-	-
CFB031	2017	SBF	1.23	0.000	0.000	-	-	-	0.019
CFB035	2017	SBF	1.85	0.001	0.001	-	-	-	-
CFB036	2017	SBF	1.53	0.001	0.001	0.969	0.834	0.896	-
CFB044	2017	SBF	1.15	0.010	0.009	0.973	0.832	0.897	0.348
CFB045	2017	SBF	1.13	0.033	0.029	0.905	0.849	0.876	0.190
CFB046	2017	SBF	2.03	0.047	0.023	0.899	0.656	0.759	0.214
CFB050	2017	SBF	1.41	0.024	0.017	0.841	0.814	0.827	0.221
CFB053	2017	SBF	1.32	0.022	0.017	0.975	0.748	0.846	0.157
CFB055	2017	SBF	1.32	0.007	0.006	0.693	0.176	0.281	0.046
CFB056	2017	SBF	2.06	0.002	0.001	0.871	0.120	0.211	-
CFB057	2017	SBF	1.68	0.006	0.003	0.912	0.728	0.809	0.020
CFB060	2017	SBF	1.02	0.006	0.006	0.896	0.695	0.782	0.254
CFB065	2017	SBF	1.43	0.005	0.003	0.940	0.889	0.914	0.207
CFB071	2017	SBF	1.79	0.013	0.007	0.544	0.240	0.333	0.045
CFB084	2017	SBF	1.59	0.002	0.002	0.955	0.438	0.600	-
CFB085	2017	SBF	1.32	0.003	0.002	0.975	0.575	0.724	-
CFB089	2017	SBF	1.47	0.001	0.000	-	0.000	-	-
CFB091	2017	SBF	1.18	0.004	0.003	0.964	0.784	0.864	0.122
CFB094	2017	SBF	1.77	0.011	0.006	0.853	0.695	0.766	0.097
CFB096	2017	SBF	1.55	0.015	0.010	0.930	0.721	0.812	0.119
CFB098	2017	SBF	1.26	0.009	0.007	0.788	0.928	0.852	-
CFB103	2017	SBF	1.53	0.008	0.005	0.741	0.804	0.771	0.078
CFB106	2017	SBF	1.33	0.002	0.001	0.993	0.501	0.666	-
CFB108	2017	SBF	0.72	0.003	0.005	0.109	0.803	0.192	-
CFB111	2017	SBF	2.47	0.007	0.003	0.991	0.432	0.602	0.201
CFB117	2017	SBF	1.23	0.015	0.012	0.264	0.501	0.346	0.030

Table A3 continued from previous page

site	year	region	total area [ha]	dead- wood [ha]	dead- wood [%]	CNN precision	CNN recall	CNN F1	LSTM RMSE
CFB119	2017	SBF	1.84	0.036	0.020	0.842	0.942	0.889	0.228
CFB121	2017	SBF	1.59	0.000	0.000	-	0.000	-	-
CFB122	2017	SBF	1.16	0.002	0.001	0.928	0.903	0.915	-
CFB124	2017	SBF	0.96	0.004	0.004	0.196	0.439	0.271	-
CFB125	2017	SBF	1.90	0.001	0.000	-	-	-	-
CFB129	2017	SBF	1.31	0.007	0.005	0.839	0.642	0.728	0.175
CFB133	2017	SBF	1.62	0.002	0.001	0.000	0.000	-	0.501
CFB134	2017	SBF	1.23	0.002	0.002	0.000	0.000	-	0.073
CFB136	2017	SBF	1.33	0.002	0.002	0.797	0.711	0.752	0.222
CFB137	2017	SBF	1.17	0.011	0.010	0.858	0.892	0.875	0.386
CFB140	2017	SBF	1.19	0.002	0.001	0.949	0.686	0.796	-
CFB141	2017	SBF	1.10	0.004	0.004	0.504	0.951	0.659	-
CFB156	2017	SBF	1.55	0.002	0.001	1.000	0.067	0.125	0.128
CFB162	2017	SBF	1.20	0.003	0.003	0.725	0.167	0.271	-
CFB163	2017	SBF	1.17	0.001	0.001	-	0.000	-	-
CFB164	2017	SBF	1.33	0.009	0.007	0.877	0.771	0.821	-
CFB167	2017	SBF	1.47	0.002	0.002	0.995	0.660	0.794	-
CFB171	2017	SBF	1.16	0.000	0.000	-	-	-	-
CFB172	2017	SBF	1.33	0.020	0.015	0.950	0.953	0.952	0.175
CFB173	2017	SBF	1.17	0.015	0.012	0.955	0.619	0.751	0.010
CFB182	2017	SBF	1.18	0.001	0.001	-	0.000	-	-
CFB184	2017	SBF	1.67	0.021	0.012	0.937	0.766	0.843	0.185
CFB188	2017	SBF	1.19	0.003	0.003	0.778	0.969	0.863	0.197
CFB037	2018	SBF	0.94	0.000	0.000	-	-	-	-
CFB039	2018	SBF	1.42	0.002	0.001	-	-	-	0.265
CFB061	2018	SBF	1.63	0.010	0.006	0.983	0.734	0.841	0.086
CFB110	2018	SBF	1.55	0.004	0.002	0.992	0.496	0.661	-
CFB151	2018	SBF	1.81	0.001	0.001	0.982	0.142	0.248	0.124
CFB002	2019	SBF	1.32	0.066	0.050	0.828	0.751	0.787	0.243
CFB003	2019	SBF	1.28	0.041	0.032	0.932	0.863	0.896	0.088
CFB005	2019	SBF	1.50	0.025	0.017	0.950	0.881	0.914	0.151
CFB008	2019	SBF	1.38	0.079	0.057	0.857	0.751	0.800	0.186
CFB010	2019	SBF	1.43	0.225	0.157	0.976	0.713	0.824	0.248
CFB014	2019	SBF	1.81	0.014	0.008	0.930	0.596	0.726	0.165
CFB015	2019	SBF	1.83	0.072	0.039	0.947	0.927	0.937	0.255
CFB018	2019	SBF	1.13	0.002	0.002	0.939	0.760	0.840	-
CFB021	2019	SBF	1.02	0.013	0.013	0.988	0.537	0.696	0.044
CFB028	2019	SBF	1.75	0.033	0.019	0.731	0.933	0.820	0.090
CFB039	2019	SBF	1.60	0.010	0.006	0.944	0.569	0.710	0.265

Table A3 continued from previous page

site	year	region	total area [ha]	dead- wood [ha]	dead- wood [%]	CNN precision	CNN recall	CNN F1	LSTM RMSE
CFB045	2019	SBF	1.26	0.023	0.018	0.809	0.850	0.829	0.190
CFB046	2019	SBF	1.33	0.071	0.054	0.971	0.748	0.845	0.214
CFB047	2019	SBF	1.52	0.074	0.048	0.964	0.841	0.898	0.302
CFB048	2019	SBF	1.40	0.015	0.011	0.926	0.779	0.846	0.186
CFB059	2019	SBF	1.29	0.097	0.075	0.938	0.900	0.919	0.183
CFB060	2019	SBF	1.34	0.043	0.032	0.930	0.626	0.749	0.254
CFB061	2019	SBF	1.19	0.016	0.013	0.935	0.814	0.870	0.086
CFB065	2019	SBF	1.33	0.013	0.010	0.563	0.735	0.638	0.207
CFB066	2019	SBF	1.12	0.009	0.008	0.570	0.885	0.693	0.028
CFB069	2019	SBF	1.34	0.014	0.010	0.771	0.869	0.817	0.427
CFB073	2019	SBF	1.34	0.004	0.003	0.222	0.611	0.326	-
CFB077	2019	SBF	1.01	0.015	0.015	0.939	0.694	0.798	0.099
CFB079	2019	SBF	1.63	0.005	0.003	0.878	0.384	0.534	0.140
CFB083	2019	SBF	1.18	0.001	0.001	-	-	-	-
CFB113	2019	SBF	1.32	0.024	0.018	0.839	0.781	0.809	0.142
CFB114	2019	SBF	1.36	0.005	0.004	0.992	0.511	0.674	0.079
CFB118	2019	SBF	1.35	0.012	0.009	0.815	0.873	0.843	0.135
CFB128	2019	SBF	1.40	0.025	0.018	0.957	0.575	0.719	0.002
CFB129	2019	SBF	1.34	0.018	0.014	0.950	0.801	0.869	0.175
CFB130	2019	SBF	1.66	0.003	0.002	0.984	0.659	0.789	-
CFB133	2019	SBF	1.56	0.002	0.002	0.874	0.934	0.903	0.501
CFB153	2019	SBF	1.53	0.000	0.000	0.000	0.000	-	-
CFB156	2019	SBF	1.60	0.015	0.010	0.932	0.900	0.916	0.128
CFB161	2019	SBF	1.04	0.111	0.107	0.957	0.931	0.944	0.248
CFB165	2019	SBF	1.41	0.007	0.005	0.955	0.833	0.890	0.226
CFB176	2019	SBF	1.12	0.008	0.007	0.945	0.726	0.821	-
CFB188	2019	SBF	1.10	0.010	0.009	0.946	0.917	0.931	0.197
HAI038	2019	HAI	2.08	0.069	0.033	-	-	-	0.232
HAI039	2019	HAI	1.53	0.001	0.001	-	-	-	-
HAI040	2019	HAI	1.86	0.017	0.009	0.079	0.194	0.112	0.137
HAI050	2019	HAI	1.52	0.003	0.002	-	0.000	-	-
KAB001	2019	KAB	3.03	0.046	0.015	0.891	0.460	0.607	0.115
KAB003	2019	KAB	3.57	0.005	0.001	0.863	0.697	0.771	0.187
KAB005	2019	KAB	13.00	0.069	0.005	0.874	0.217	0.348	0.295
KAB009	2019	KAB	3.91	0.195	0.050	0.888	0.328	0.479	0.182
KAB010	2019	KAB	3.71	0.018	0.005	0.809	0.605	0.692	0.250
KAB011	2019	KAB	2.88	0.043	0.015	0.757	0.526	0.621	0.185
NBF003	2019	NBF	14.50	1.433	0.099	0.939	0.908	0.923	0.232
NBF004	2019	NBF	15.23	3.076	0.202	0.872	0.906	0.889	0.211

Table A3 continued from previous page

site	year	region	total area [ha]	dead- wood [ha]	dead- wood [%]	CNN precision	CNN recall	CNN F1	LSTM RMSE
NBF005	2019	NBF	13.83	0.515	0.037	0.900	0.839	0.868	0.296
NBF006	2019	NBF	16.01	0.659	0.041	0.907	0.749	0.820	0.227
NBF007	2019	NBF	16.32	0.136	0.008	0.756	0.773	0.764	0.221
NBF008	2019	NBF	12.80	0.150	0.012	0.783	0.898	0.836	0.163
NBF009	2019	NBF	10.91	0.121	0.011	0.886	0.930	0.907	0.191
NBF010	2019	NBF	10.39	1.110	0.107	0.948	0.830	0.885	0.298
NBF011	2019	NBF	7.14	0.061	0.009	0.925	0.877	0.901	0.121
NBF012	2019	NBF	9.28	0.015	0.002	0.759	0.824	0.790	0.295
NBF013	2019	NBF	12.31	0.318	0.026	0.864	0.891	0.877	0.266
NBF014	2019	NBF	8.71	0.053	0.006	0.942	0.728	0.821	0.215
CFB001	2020	SBF	1.29	0.031	0.024	0.892	0.506	0.645	0.178
CFB009	2020	SBF	1.53	0.025	0.016	0.891	0.789	0.837	0.074
CFB019	2020	SBF	1.75	0.009	0.005	0.918	0.924	0.921	0.112
CFB031	2020	SBF	1.55	0.006	0.004	0.973	0.966	0.969	0.019
CFB034	2020	SBF	1.28	0.004	0.003	0.848	0.690	0.761	0.187
CFB044	2020	SBF	1.44	0.008	0.005	0.911	0.714	0.800	0.348
CFB050	2020	SBF	1.41	0.046	0.033	0.956	0.756	0.844	0.221
CFB057	2020	SBF	1.70	0.012	0.007	0.991	0.737	0.845	0.020
CFB058	2020	SBF	1.43	0.022	0.015	0.916	0.843	0.878	0.123
CFB068	2020	SBF	1.81	0.014	0.008	0.945	0.383	0.545	-
CFB072	2020	SBF	1.33	0.010	0.008	0.970	0.696	0.811	-
CFB091	2020	SBF	1.16	0.052	0.045	0.984	0.904	0.942	0.122
CFB096	2020	SBF	1.75	0.041	0.024	0.884	0.727	0.798	0.119
CFB101	2020	SBF	1.27	0.027	0.022	0.757	0.548	0.635	0.284
CFB104	2020	SBF	1.76	0.180	0.102	0.976	0.546	0.700	0.255
CFB107	2020	SBF	1.90	0.182	0.096	0.892	0.931	0.911	0.201
CFB111	2020	SBF	2.15	0.061	0.028	0.973	0.840	0.902	0.201
CFB119	2020	SBF	2.00	0.032	0.016	0.928	0.890	0.908	0.228
CFB131	2020	SBF	1.15	0.003	0.003	0.889	0.651	0.752	0.288
CFB135	2020	SBF	1.77	0.008	0.005	0.940	0.522	0.671	0.087
CFB138	2020	SBF	1.75	0.014	0.008	0.972	0.841	0.902	0.016
CFB140	2020	SBF	1.24	0.003	0.002	0.970	0.782	0.866	-
CFB148	2020	SBF	1.54	0.006	0.004	0.924	0.807	0.862	0.205
CFB151	2020	SBF	1.08	0.020	0.018	0.947	0.520	0.672	0.124
CFB171	2020	SBF	1.71	0.001	0.000	-	-	-	-
CFB172	2020	SBF	1.43	0.009	0.006	0.600	0.903	0.721	0.175
CFB177	2020	SBF	1.34	0.007	0.005	0.964	0.881	0.921	0.040
CFB178	2020	SBF	1.64	0.017	0.010	0.564	0.802	0.662	0.367
CFB180	2020	SBF	1.38	0.017	0.013	0.965	0.817	0.885	0.378

Table A3 continued from previous page

site	year	region	total area [ha]	dead- wood [ha]	dead- wood [%]	CNN precision	CNN recall	CNN F1	LSTM RMSE
CFB183	2020	SBF	1.85	0.025	0.013	0.057	0.816	0.107	0.377
CFB184	2020	SBF	1.43	0.019	0.013	0.933	0.721	0.813	0.185
CFB900	2020	SBF	5.80	0.072	0.012	0.910	0.688	0.784	0.150
FIN001	2020	FIN	22.76	0.304	0.013	0.921	0.775	0.841	0.168
FIN002	2020	FIN	19.09	0.266	0.014	0.894	0.652	0.754	0.245
FIN003	2020	FIN	20.19	0.135	0.007	0.888	0.699	0.782	0.219
CFB900	2021	SBF	5.62	0.060	0.011	0.818	0.864	0.841	0.150
CFB910	2021	SBF	6.58	0.380	0.058	0.942	0.891	0.916	0.244
CFB921	2021	SBF	10.52	0.248	0.024	0.965	0.743	0.840	0.192
CFB922	2021	SBF	2.88	0.029	0.010	0.956	0.789	0.864	0.195
CFB923	2021	SBF	3.00	0.051	0.017	0.935	0.908	0.921	0.196
CFB931	2021	SBF	8.58	1.299	0.151	0.937	0.875	0.905	0.242
CFB932	2021	SBF	4.70	0.179	0.038	0.951	0.772	0.852	0.189
CFB933	2021	SBF	4.84	0.040	0.008	0.867	0.795	0.830	0.121
CFB941	2021	SBF	9.62	0.749	0.078	0.928	0.781	0.848	0.184
CFB942	2021	SBF	12.19	0.600	0.049	0.926	0.867	0.896	0.197
DDH001	2021	DDH	4.02	1.009	0.251	0.952	0.889	0.919	0.203
DDH002	2021	DDH	2.14	0.134	0.062	0.924	0.898	0.911	0.273
DDH003	2021	DDH	6.24	1.248	0.200	0.968	0.924	0.945	0.223
DDH004	2021	DDH	1.52	0.071	0.046	0.888	0.810	0.847	0.183
DDH005	2021	DDH	20.48	2.057	0.100	0.868	0.865	0.866	0.212
DDH006	2021	DDH	1.77	0.110	0.062	0.853	0.902	0.877	0.232
DDH007	2021	DDH	1.11	0.056	0.051	0.858	0.745	0.797	0.109
DDH008	2021	DDH	3.47	0.075	0.022	0.668	0.817	0.735	0.107
NBF001	2021	NBF	1.71	1.113	0.651	-	-	-	0.175
NBF002	2021	NBF	0.36	0.245	0.681	-	-	-	0.195

APPENDIX A6

Table A4: Environmental predictor variables

Variable	GSD	Unit	Rationale (include/exclude)	Data source
Slope		°		
Eastness	10 m	rad	Topographic site conditions	Slope and eastness (sinus) and northness (cosine) of terrain aspect derived Copernicus DEM (2021)
Northness		rad		
Sand content	30 m	%	Soil type	Hengl, T. and Parente, L. (2022)
Stand age	100 m	years	Hypothesis that older trees more susceptible to mortality	Besnard et al. (2021)
Canopy height	10 m	m	Hypothesis that taller trees more susceptible to mortality	Lang et al., 2023
Tree species richness	10 m	no.	Hypothesis that tree species richness mitigates mortality	Calculated from Blickensdörfer et al. (2024) tree species map as number of tree species in a 100 m buffer
Mean diurnal temperature range (BIO2)		°C	<i>Correlated with BIO7 that better reflects the average site conditions</i>	
Temperature annual range (BIO7)	30 sec	°C		Derived from Fick and Hijmans (2017)
Mean temperature of warmest quarter (BIO10)		°C	<i>Correlated with vapor pressure deficit</i>	
Annual precipitation (BIO12)		mm	<i>Correlated with BIO18 which is more meaningful for vegetation growth</i>	
Precipitation seasonality (BIO15)		mm		
Precipitation of warmest quarter (BIO18)		mm		
Late frosts*	1 km	days	Frost damage after bud burst	Calculated from vegetation onset (DWD, 2023b) and CERRA reanalysis (Schimanke et al., 2021)
Soil drought intensity*	4 km	-		During vegetation period (Zink et al., 2016)
Total precipitation*	1 km	mm	<i>Correlated with vapor pressure deficit that incorporates both</i>	Sum over growing period (March-October) (DWD, 2023d)
Mean Temperature*	1 km	°C	<i>Correlated with vapor pressure deficit that incorporates both</i>	DWD (2023c)
Vapor pressure deficit	5.5 km	Pa	Driving hydraulic failure	Calculated as 75%-quartile of daily maximum during growing period (March-October) from CERRA reanalysis (Schimanke et al., 2021)
Climatic water balance*	1 km	mm		Calculated from DWD (2023d, 2023e) as anomaly from DWD (2023f)
Hot days*	1 km	days		DWD (2023a)
Biomass	100 m	Mg/ha		ESA Biomass CCI (Santoro & Cartus, 2023)
Net Primary Productivity	500 m	kgC/m ² /year		Running, S. and Zhao, M. (2021)

*Variable also for the year prior to first occurrence of standing deadwood

APPENDIX A7

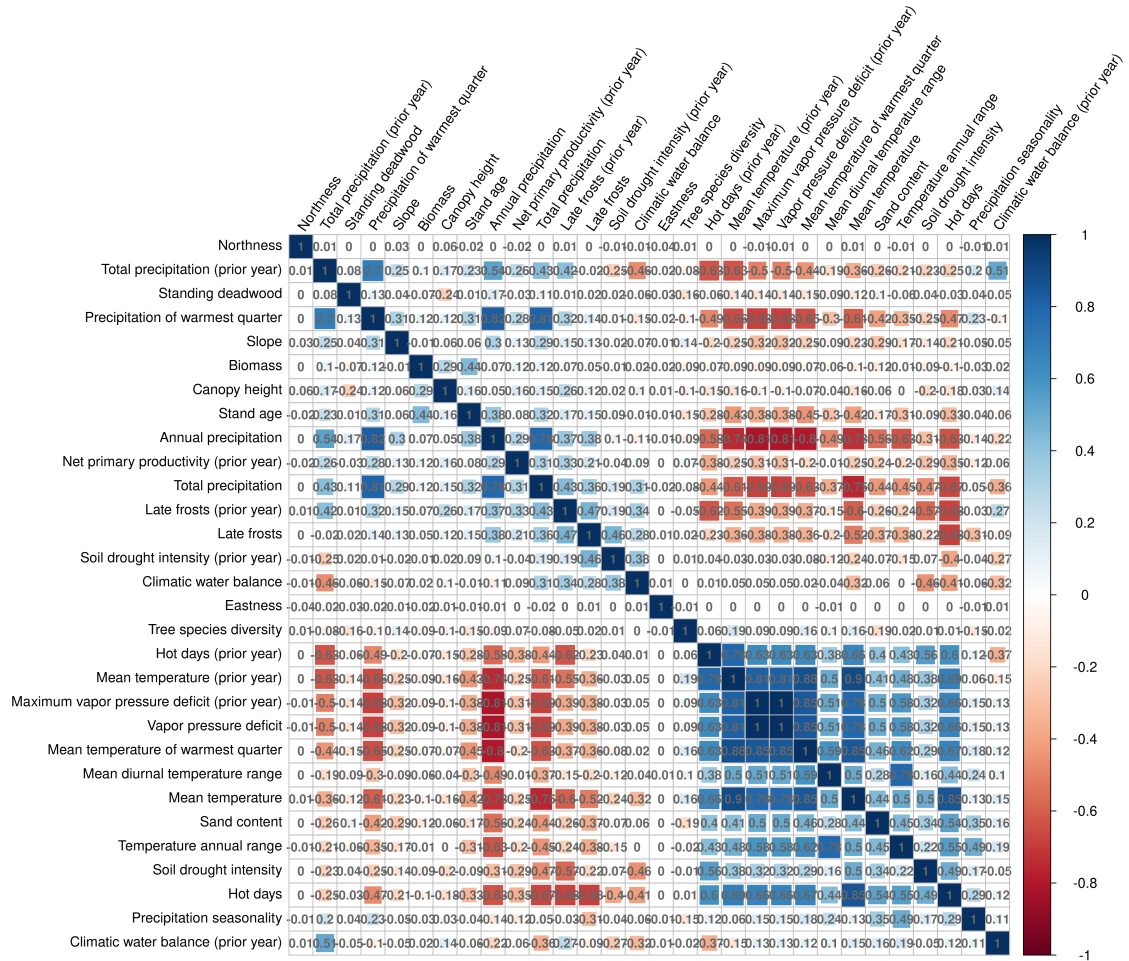


Figure A2: Correlation plot for all environmental predictor variables and standing deadwood. Variables with correlations higher than 0.7 were dropped for the analysis.

APPENDIX A8

Table A5: Standing deadwood for the seven dominant tree species in Germany over the years 2018–2021

Species	Year	Area [kha] (mean)	Area [kha] (sd)	Percent [%] (mean)	Percent [%] (sd)
all	2018	178.67	126.26	1.44	1.01
	2019	333.68	188.89	2.58	1.45
	2020	307.24	151.05	2.62	1.31
	2021	158.27	63.14	1.33	0.64
	acc.	977.87	529.35	7.97	4.41
<i>Abies</i>	2018	4.48	4.32	0.27	0.23
	2019	4.34	3.92	0.32	0.29
	2020	5.71	4.81	0.26	0.21
	2021	3.04	2.15	0.18	0.12
	acc.	17.57	15.20	1.03	0.86
<i>Fagus</i>	2018	2.11	1.75	0.63	0.39
	2019	7.49	4.36	2.05	1.03
	2020	17.09	8.27	3.51	1.56
	2021	10.16	4.17	1.96	0.80
	acc.	36.85	18.55	8.15	3.78
<i>Larix</i>	2018	7.50	6.10	0.63	0.49
	2019	10.10	7.81	0.84	0.62
	2020	5.61	4.41	0.43	0.33
	2021	2.60	1.93	0.21	0.16
	acc.	25.81	20.25	2.11	1.60
<i>Picea</i>	2018	38.16	22.38	1.75	0.92
	2019	88.03	38.63	6.28	2.09
	2020	146.09	44.27	8.36	2.55
	2021	105.79	28.65	5.10	1.51
	acc.	378.07	133.93	21.49	7.06
<i>Pinus</i>	2018	113.30	81.60	4.44	2.95
	2019	201.88	118.79	6.75	3.85
	2020	115.95	78.18	6.59	3.77
	2021	29.58	21.77	2.22	1.41
	acc.	460.71	300.35	20.00	11.98
<i>Pseudotsuga</i>	2018	3.10	2.32	1.05	0.76
	2019	6.54	4.43	2.09	1.34
	2020	6.75	4.22	2.03	1.23
	2021	2.94	1.80	0.88	0.53
	acc.	19.33	12.77	6.04	3.87
<i>Quercus</i>	2018	0.37	0.34	0.21	0.14

Table A5 continued from previous page

Species	Year	Area [kha] (mean)	Area [kha] (sd)	Percent [%] (mean)	Percent [%] (sd)
	2019	1.00	0.61	0.84	0.26
	2020	2.19	1.28	2.11	0.87
	2021	0.71	0.33	1.38	0.46
	acc.	4.26	2.56	4.54	1.73
other	2018	9.65	7.51	1.56	1.20
	2019	14.31	10.50	2.05	1.47
	2020	7.86	5.78	1.31	0.95
	2021	3.45	2.64	0.66	0.49
	acc.	35.27	26.43	5.57	4.12

APPENDIX A9

Table A6: Accumulated standing deadwood during 2018-2021 for the major natural regions of Germany

ID	Major natural regions of Germany		Forested area [kha]	Standing deadwood	
	Name (eng.)	Name (ger.)		Area [kha]	Percent [%]
D01	Mecklenburg-Western Pomeranian Littoral	Mecklenburgisch-Vorpommersches Küstengebiet	50.58	0.48	0.95
D02	Northeast Mecklenburg Plain and Szczecin Lagoon	Nordostmecklenburgisches Tiefland mit Oderhafengebiet	96.15	1.09	1.14
D03	Hinterland of the Mecklenburg Lake Plateau	Rückland der Mecklenburg-Brandenburgischen Seenplatte	155.76	2.16	1.39
D04	Mecklenburg Lake Plateau	Mecklenburgische Seenplatte	265.71	3.3	1.24
D05	Mecklenburg-Brandenburg Plateau and Upland	Mecklenburg-Brandenburgisches Platten- und Hügelland	264.2	18.19	6.88
D06	East Brandenburg Plateau	Ostbrandenburgische Platte	84.32	1.3	1.54
D07	Oder Valley	Odertal	14.02	0.48	3.43
D08	Lusatian Basin and Spreewald	Spreewald und Lausitzer Becken- und Heideland	143.36	18.08	12.61
D09	Middle Elbe Plain	Elbtalniederung	91.39	19.31	21.13
D10	Elbe-Mulde Plain	Elbe-Mulde-Tiefland	121.82	26.06	21.4
D11	Fläming Heath	Fläming	161.75	26.51	16.39
D12	Brandenburg Heath and Lake District	Brandenburgisches Heide- und Seengebiet	322.12	25.08	7.79
D13	Upper Lusatian Plateau	Oberlausitzer Heideland	119.34	8.3	6.95
D14	Upper Lusatian	Oberlausitz	44.92	4.37	9.72
D15	Saxon-Bohemian Chalk Sandstone Region	Sächsisch-Böhmisches Kreidesandsteingebiet	24.68	4.54	18.39
D16	Ore Mountains	Erzgebirge	156.22	7.56	4.84
D17	Vogtland	Vogtland	94.89	4.86	5.12

Table A6 continued from previous page

ID	Major natural regions of Germany		Forested area [kha]	Standing deadwood	
	Name (eng.)	Name (ger.)		Area [kha]	Percent [%]
D18	Thuringian Basin and Peripheral Uplands	Thüringer Becken und Randplatten	220.28	9.79	4.45
D19	Saxon Lowland and Saxon Uplands	Erzgebirgsvorland und Sächsisches Hügelland	96.06	5.4	5.62
D20	Eastern Harz Foreland	Mitteldeutsches Schwarzerdegebiet	11.77	1.37	11.67
D21	Schleswig-Holstein Marsh	Schleswig-Holsteinische Marschen und Nordseeinseln	1.17	0.01	0.45
D22	Schleswig-Holstein Geest	Schleswig-Holsteinische Geest	73.75	0.4	0.54
D23	Schleswig-Holstein Uplands	Schleswig-Holsteinisches Hügelland	68.95	0.3	0.44
D24	Lower Elbe Marsh	Untere Elbeniederung (Elbmarsch)	3.92	0.07	1.9
D25	Lower Ems and Weser Marshes	Ems-Weser-Marsch	3.44	0.03	0.8
D26	East Frisian Geest	Ostfriesisch-Oldenburgische Geest	28.77	0.17	0.58
D27	Stade Geest	Stader Geest	84.11	0.66	0.79
D28	Lüneburg Heath	Lüneburger Heide	283.3	15.34	5.41
D29	Wendland and Altmark	Wendland und Altmark	112.82	18.99	16.83
D30	Dümmer and Ems-Hunte Geest	Dümmer Geestniederung und Ems-Hunte-Geest	148.26	2.22	1.5
D31	Weser-Aller Plains and Geest	Weser-Aller-Tiefland	135.45	5.75	4.25
D32	Lower Saxony Börde	Niedersächsische Börden	9.81	0.13	1.3
D33	North Harz Foreland	Nördliches Harzvorland	33.54	2.04	6.07
D34	Westphalian Lowland	Westfälische Tieflandsbucht	122.38	2.99	2.44
D35	Lower Rhine Plain and Cologne Lowland	Kölner Bucht und Niederrheinisches Tiefland	95.53	2.7	2.83
D36	Lower Saxon Hills	Niedersächsisches Bergland	361.5	19.98	5.53

Table A6 continued from previous page

ID	Major natural regions of Germany		Forested area [kha]	Standing deadwood	
	Name (eng.)	Name (ger.)		Area [kha]	Percent [%]
D37	Harz	Harz	156.42	47.16	30.15
D38	Süder Uplands	Sauerland	433.56	74.2	17.11
D39	Westerwald	Westerwald	152.71	12.87	8.43
D40	Lahn Valley	Lahntal und Limburger Becken	9.17	0.3	3.25
D41	Taunus	Taunus	129.13	7.04	5.45
D42	Hunsrück	Hunsrück	153.37	4.58	2.99
D43	Moselle Valley	Moseltal	25.73	0.33	1.28
D44	Middle Rhine Valley	Mittelrheingebiet	35.89	1.24	3.46
D45	Eifel and Venn Foreland	Eifel und Vennvorland	239.97	9.95	4.15
D46	West Hesse Uplands	Westhessisches Berg- und Beckenland	143.98	6.02	4.18
D47	East Hesse Upland	Osthessisches Bergland	326.82	13.01	3.98
D48	Thuringian-Franconian Highlands	Thüringisch-Fränkisches Mittelgebirge	296.6	16.4	5.53
D49	Gutland (Bitburg Land)	Gutland (Bitburger Land)	24.34	0.32	1.3
D50	Palatine-Saarland Muschelkalk Region	Pfälzisch-Saarländisches Muschelkalkgebiet	33.58	0.31	0.93
D51	Palatine Forest (the Haardt)	Pfälzer Wald (Haardtgebirge)	133.11	2.12	1.59
D52	Saar-Nahe Hills	Saar-Nahe-Berg- und Hügelland	157.89	1.81	1.15
D53	Upper Rhine Plain	Oberrheinisches Tiefland	186.11	3.04	1.63
D54	Black Forest	Schwarzwald	397.68	5	1.26
D55	Odenwald-Spessart-Rhön	Odenwald, Spessart und Südrhön	339.89	2.99	0.88
D56	Main Franconia Plateau	Mainfränkische Platten	120.47	1.65	1.37
D57	Neckar and Tauber Gäu Plateaus	Neckar- und Tauberland, Gäuplatten	218.15	0.98	0.45
D58	Swabian Keuper-Lias Lands	Schwäbisches Keuper-Liasland	199.92	0.44	0.22
D59	Franconian Keuper-Lias Lands	Fränkisches Keuper-Liasland	325.97	4.91	1.5
D60	Swabian Jura	Schwäbische Alb	233.82	0.36	0.16
D61	Franconian Jura	Fränkische Alb	281.11	1.79	0.64

Table A6 continued from previous page

ID	Major natural regions of Germany		Forested area [kha]	Standing deadwood	
	Name (eng.)	Name (ger.)		Area [kha]	Percent [%]
D62	Upper Palatine-Upper Main Hills	Oberpfälzisch-Obermainisches Hügelland	117.88	1.3	1.1
D63	Upper Palatine-Bavarian Forest	Oberpfälzer und Bayerischer Wald	346.9	5.05	1.46
D64	Iller-Lech Plateau	Donau-Iller-Lech-Platten	202.97	0.7	0.34
D65	Lower Bavarian Upland and Isar-Inn Gravel Plateau	Unterbayerisches Hügelland und Isar-Inn-Schotterplatten	288.55	2.26	0.78
D66	Pre-Alpine Hills and Moorland	Voralpines Hügel- und Moorland	280.51	0.92	0.33
D67	Swabian-Bavarian Pre-alps	Schwäbisch-Oberbayerische Voralpen	158.84	4.4	2.77
D68	Northern Limestone Alps	Nördliche Kalkalpen	50.82	4.95	9.75
D69	Dinkelberg and Upper Rhine Valley	Hochrheingebiet und Dinkelberg	8.62	0.06	0.67
D70	German Bight	Deutsche Bucht	-	-	-
D71	Dogger Bank	Doggerbank und angrenzende zentrale Nordsee	-	-	-
D72	Western Baltic	Westliche Ostsee	0.14	0	0.73
D73	Eastern Baltic	Östliche Ostsee	0.68	0.01	1.47

REFERENCES

- Abadi, M., Agarwal, A., Barham, P., Brevdo, E., Chen, Z., Citro, C., Corrado, G. S., Davis, A., Dean, J., Devin, M., Ghemawat, S., Goodfellow, I., Harp, A., Irving, G., Isard, M., Jia, Y., Jozefowicz, R., Kaiser, L., Kudlur, M., . . . Zheng, X. (2016). *TensorFlow: Large-Scale Machine Learning on Heterogeneous Distributed Systems [preprint]*. <http://arxiv.org/abs/1603.04467>
- Ahmad, R., Yang, B., Ettlin, G., Berger, A., & Rodríguez-Bocca, P. (2023). A machine-learning based ConvLSTM architecture for NDVI forecasting. *International Transactions in Operational Research*, 30(4), 2025–2048. <https://doi.org/10.1111/itor.12887>
- Ali, A. M., Abdullah, H., Darvishzadeh, R., Skidmore, A. K., Heurich, M., Roeoesli, C., Paganini, M., Heiden, U., & Marshall, D. (2021). Canopy chlorophyll content retrieved from time series remote sensing data as a proxy for detecting bark beetle infestation. *Remote Sensing Applications: Society and Environment*, 22, 100524. <https://doi.org/10.1016/j.rsase.2021.100524>
- Allaire, J. J., Chollet, F., Tang, Y., Falbel, D., Bijl, W. V. D., Studer, M., & Keydana, S. (2019a). *keras: R Interface to 'Keras'* (Version 2.2.5.0). <https://cran.r-project.org/web/packages/keras/index.html>
- Allaire, J. J., Kalinowski, T., Falbel, D., Eddelbuettel, D., Tang, Y., & Golding, N. (2019b). *tensorflow: R Interface to 'TensorFlow'* (Version 2.0.0). <https://cran.r-project.org/web/packages/tensorflow/index.html>
- Allaire, J. J., Tang, Y., & Ushey, K. (2019c). *tfdatasets: Interface to 'TensorFlow' Datasets* (Version 2.0.0). <https://cran.r-project.org/web/packages/tfdatasets/index.html>
- Allen, C. D., Breshears, D. D., & McDowell, N. G. (2015). On underestimation of global vulnerability to tree mortality and forest die-off from hotter drought in the Anthropocene. *Ecosphere*, 6(8), art129. <https://doi.org/10.1890/ES15-00203.1>
- Allen, C. D., Macalady, A. K., Chenchouni, H., Bachelet, D., McDowell, N., Venetier, M., Kitzberger, T., Rigling, A., Breshears, D. D., Hogg, E. H. (, Gonzalez, P., Fensham, R., Zhang, Z., Castro, J., Demidova, N., Lim, J.-H., Allard, G., Running, S. W., Semerci, A., & Cobb, N. (2010). A global overview of drought and heat-induced tree mortality reveals emerging climate change risks for forests. *Forest Ecology and Management*, 259(4), 660–684. <https://doi.org/10.1016/j.foreco.2009.09.001>

- Alvarez-Vanhard, E., Corpetti, T., & Houet, T. (2021). UAV & satellite synergies for optical remote sensing applications: A literature review. *Science of Remote Sensing*, 3, 100019. <https://doi.org/10.1016/j.srs.2021.100019>
- Alvarez-Vanhard, E., Houet, T., Mony, C., Lecoq, L., & Corpetti, T. (2020). Can UAVs fill the gap between in situ surveys and satellites for habitat mapping? *Remote Sensing of Environment*, 243, 111780. <https://doi.org/10.1016/j.rse.2020.111780>
- Anderegg, W. R. L., Konings, A. G., Trugman, A. T., Yu, K., Bowling, D. R., Gabbitas, R., Karp, D. S., Pacala, S., Sperry, J. S., Sulman, B. N., & Zenes, N. (2018). Hydraulic diversity of forests regulates ecosystem resilience during drought. *Nature*, 561(7724), 538–541. <https://doi.org/10.1038/s41586-018-0539-7>
- Anderson, C. B. (2018). Biodiversity monitoring, earth observations and the ecology of scale. *Ecology Letters*, 21(10), 1572–1585. <https://doi.org/10/gdwhdb>
- Anderson, K., & Gaston, K. J. (2013). Lightweight unmanned aerial vehicles will revolutionize spatial ecology. *Frontiers in Ecology and the Environment*, 11(3), 138–146. <https://doi.org/10.1890/120150>
- Apley, D. W., & Zhu, J. (2020). Visualizing the Effects of Predictor Variables in Black Box Supervised Learning Models. *Journal of the Royal Statistical Society Series B: Statistical Methodology*, 82(4), 1059–1086. <https://doi.org/10.1111/rssb.12377>
- Asner, G. P. (1998). Biophysical and Biochemical Sources of Variability in Canopy Reflectance. *Remote Sensing of Environment*, 64(3), 234–253. [https://doi.org/10.1016/S0034-4257\(98\)00014-5](https://doi.org/10.1016/S0034-4257(98)00014-5)
- Asner, G. P., Martin, R. E., Anderson, C. B., & Knapp, D. E. (2015). Quantifying forest canopy traits: Imaging spectroscopy versus field survey. *Remote Sensing of Environment*, 158, 15–27. <https://doi.org/10/f6zd6r>
- Audebert, N., Le Saux, B., & Lefevre, S. (2019). Deep Learning for Classification of Hyperspectral Data: A Comparative Review. *IEEE Geoscience and Remote Sensing Magazine*, 7(2), 159–173. <https://doi.org/10/ghj5th>
- Badrinarayanan, V., Kendall, A., & Cipolla, R. (2017). SegNet: A Deep Convolutional Encoder-Decoder Architecture for Image Segmentation. *IEEE Transactions on Pattern Analysis and Machine Intelligence*, 39(12), 2481–2495. <https://doi.org/10/gcj4jr>
- Baeten, L., Verheyen, K., Wirth, C., Bruelheide, H., Bussotti, F., Finér, L., Jaroszewicz, B., Selvi, F., Valladares, F., Allan, E., Ampoorter, E., Auge, H., Avăcăriei, D., Barbaro, L., Bărnoaiea, I., Bastias, C. C., Bauhus, J., Beinhoff, C., Benavides, R., ... Scherer-Lorenzen, M. (2013). A novel comparative research platform designed to determine the functional significance of tree species diversity in European forests. *Perspectives in Plant Ecology, Evolution and Systematics*, 15(5), 281–291. <https://doi.org/10.1016/j.ppees.2013.07.002>

-
- Bárta, V., Lukeš, P., & Homolová, L. (2021). Early detection of bark beetle infestation in Norway spruce forests of Central Europe using Sentinel-2. *International Journal of Applied Earth Observation and Geoinformation*, *100*, 102335. <https://doi.org/10.1016/j.jag.2021.102335>
- Bastos, A., Orth, R., Reichstein, M., Ciais, P., Viovy, N., Zaehle, S., Anthoni, P., Arneth, A., Gentine, P., Joetzer, E., Lienert, S., Loughran, T., McGuire, P. C., O, S., Pongratz, J., & Sitch, S. (2021). Vulnerability of European ecosystems to two compound dry and hot summers in 2018 and 2019. *Earth System Dynamics*, *12*(4), 1015–1035. <https://doi.org/10.5194/esd-12-1015-2021>
- Bauhus, J., Forrester, D. I., Gardiner, B., Jactel, H., Vallejo, R., & Pretzsch, H. (2017). Ecological Stability of Mixed-Species Forests. In H. Pretzsch, D. I. Forrester, & J. Bauhus (Eds.), *Mixed-Species Forests: Ecology and Management* (pp. 337–382). Springer. https://doi.org/10.1007/978-3-662-54553-9_7
- Beloiu, M., Heinzmann, L., Rehus, N., Gessler, A., & Griess, V. C. (2023). Individual Tree-Crown Detection and Species Identification in Heterogeneous Forests Using Aerial RGB Imagery and Deep Learning. *Remote Sensing*, *15*(5), 1463. <https://doi.org/10.3390/rs15051463>
- Bennett, A. C., McDowell, N. G., Allen, C. D., & Anderson-Teixeira, K. J. (2015). Larger trees suffer most during drought in forests worldwide. *Nature Plants*, *1*(10), 1–5. <https://doi.org/10.1038/nplants.2015.139>
- Besnard, S., Koirala, S., Santoro, M., Weber, U., Nelson, J., Gütter, J., Herault, B., Kassi, J., N'Guessan, A., Neigh, C., Poulter, B., Zhang, T., & Carvalhais, N. (2021). Mapping global forest age from forest inventories, biomass and climate data. *Earth System Science Data*, *13*(10), 4881–4896. <https://doi.org/10.5194/essd-13-4881-2021>
- Blickensdörfer, L., Oehmichen, K., Pflugmacher, D., Kleinschmit, B., & Hostert, P. (2024). National tree species mapping using Sentinel-1/2 time series and German National Forest Inventory data. *Remote Sensing of Environment*, *304*, 114069. <https://doi.org/10.1016/j.rse.2024.114069>
- Blondeel, H., Guillemot, J., Martin-StPaul, N., Druel, A., Bilodeau-Gauthier, S., Bauhus, J., Grossiord, C., Hector, A., Jactel, H., Jensen, J., Messier, C., Muys, B., Serrano-León, H., Auge, H., Barsoum, N., Birhane, E., Bruelheide, H., Cavender-Bares, J., Chu, C., ... Baeten, L. (2024). Tree diversity reduces variability in sapling survival under drought. *Journal of Ecology*, *112*(5), 1164–1180. <https://doi.org/10.1111/1365-2745.14294>
- Braga, J. R. G., Peripato, V., Dalagnol, R., Ferreira, M. P., Tarabalka, Y., O. C. Aragão, L. E., F. de Campos Velho, H., Shiguemori, E. H., & Wagner, F. H. (2020). Tree Crown Delineation Algorithm Based on a Convolutional Neural Network. *Remote Sensing*, *12*(8), 1288. <https://doi.org/10/gh3dk6>
- Breiman, L. (2001). Random Forests. *Machine Learning*, *45*(1), 5–32. <https://doi.org/10/d8zjwq>

- Briechle, S., Krzystek, P., & Vosselman, G. (2021). Silvi-Net – A dual-CNN approach for combined classification of tree species and standing dead trees from remote sensing data. *International Journal of Applied Earth Observation and Geoinformation*, 98, 102292. <https://doi.org/10.1016/j.jag.2020.102292>
- Brodrick, P. G., & Asner, G. P. (2017). Remotely sensed predictors of conifer tree mortality during severe drought. *Environmental Research Letters*, 12(11), 115013. <https://doi.org/10.1088/1748-9326/aa8f55>
- Brodrick, P. G., Davies, A. B., & Asner, G. P. (2019). Uncovering Ecological Patterns with Convolutional Neural Networks. *Trends in Ecology & Evolution*, 34(8), 734–745. <https://doi.org/10/gf559b>
- Bundesministerium für Ernährung und Landwirtschaft (BMEL). (2023). Ergebnisse der Waldzustandserhebung 2022. <https://doi.org/https://www.bmel.de/DE/themen/wald/wald-in-deutschland/waldzustandserhebung.html>
- Buras, A., Rammig, A., & Zang, C. S. (2020). Quantifying impacts of the 2018 drought on European ecosystems in comparison to 2003. *Biogeosciences*, 17(6), 1655–1672. <https://doi.org/10/ggqkkm>
- Burman, P., Chow, E., & Nolan, D. (1994). A Cross-Validatory Method for Dependent Data. *Biometrika*, 81(2), 351–358. <https://doi.org/10.2307/2336965>
- Byer, S., & Jin, Y. (2017). Detecting Drought-Induced Tree Mortality in Sierra Nevada Forests with Time Series of Satellite Data. *Remote Sensing*, 9(9), 929. <https://doi.org/10.3390/rs9090929>
- Campbell, J. B., Wynne, R. H., & Thomas, V. A. (2023). *Introduction to remote sensing* (Sixth edition). The Guilford Press.
- Campbell, M. J., Dennison, P. E., Tune, J. W., Kannenberg, S. A., Kerr, K. L., Coddling, B. F., & Anderegg, W. R. L. (2020). A multi-sensor, multi-scale approach to mapping tree mortality in woodland ecosystems. *Remote Sensing of Environment*, 245, 111853. <https://doi.org/10.1016/j.rse.2020.111853>
- Campos-Taberner, M., García-Haro, F. J., Martínez, B., Izquierdo-Verdiguier, E., Atzberger, C., Camps-Valls, G., & Gilabert, M. A. (2020). Understanding deep learning in land use classification based on Sentinel-2 time series. *Scientific Reports*, 10(1), 17188. <https://doi.org/10/ghfwx8>
- Camps-Valls, G., Campos-Taberner, M., Moreno-Martínez, Á., Walther, S., Duveiller, G., Cescatti, A., Mahecha, M. D., Muñoz-Marí, J., García-Haro, F. J., Guanter, L., Jung, M., Gamon, J. A., Reichstein, M., & Running, S. W. (2021). A unified vegetation index for quantifying the terrestrial biosphere. *Science Advances*, 7(9), eabc7447. <https://doi.org/10.1126/sciadv.abc7447>
- Chen, L.-C., Papandreou, G., Schroff, F., & Adam, H. (2017). Rethinking Atrous Convolution for Semantic Image Segmentation [preprint]. <http://arxiv.org/abs/1706.05587>
- Chen, Y., Lee, W. S., Gan, H., Peres, N., Fraise, C., Zhang, Y., & He, Y. (2019). Strawberry Yield Prediction Based on a Deep Neural Network Using High-

-
- Resolution Aerial Orthoimages. *Remote Sensing*, 11(13), 1584. <https://doi.org/10/gh3dnh>
- Cheng, Y., Oehmcke, S., Brandt, M., Rosenthal, L., Das, A., Vrieling, A., Saatchi, S., Wagner, F., Mugabowindekwe, M., Verbruggen, W., Beier, C., & Horion, S. (2024). Scattered tree death contributes to substantial forest loss in California. *Nature Communications*, 15(1), 641. <https://doi.org/10.1038/s41467-024-44991-z>
- Cherif, E., Feilhauer, H., Berger, K., Dao, P. D., Ewald, M., Hank, T. B., He, Y., Kovach, K. R., Lu, B., Townsend, P. A., & Kattenborn, T. (2023). From spectra to plant functional traits: Transferable multi-trait models from heterogeneous and sparse data. *Remote Sensing of Environment*, 292, 113580. <https://doi.org/10.1016/j.rse.2023.113580>
- Chetlur, S., Woolley, C., Vandermersch, P., Cohen, J., Tran, J., Catanzaro, B., & Shelhamer, E. (2014). cuDNN: Efficient Primitives for Deep Learning [preprint]. <http://arxiv.org/abs/1410.0759>
- Chiang, C.-Y., Barnes, C., Angelov, P., & Jiang, R. (2020). Deep Learning-Based Automated Forest Health Diagnosis From Aerial Images. *IEEE Access*, 8, 144064–144076. <https://doi.org/10.1109/ACCESS.2020.3012417>
- Chollet, F., & Allaire, J. J. (2017). *R Interface to Keras*. Retrieved January 23, 2024, from <https://github.com/rstudio/keras>
- Chollet, F., Kalinowski, T., & Allaire, J. J. (2022). *Deep learning with R* (Second edition). Manning.
- Clark, J. S., Iverson, L., Woodall, C. W., Allen, C. D., Bell, D. M., Bragg, D. C., D'Amato, A. W., Davis, F. W., Hersh, M. H., Ibanez, I., Jackson, S. T., Matthews, S., Pederson, N., Peters, M., Schwartz, M. W., Waring, K. M., & Zimmermann, N. E. (2016). The impacts of increasing drought on forest dynamics, structure, and biodiversity in the United States. *Global Change Biology*, 22(7), 2329–2352. <https://doi.org/10.1111/gcb.13160>
- Coops, N. C., Shang, C., Wulder, M. A., White, J. C., & Hermosilla, T. (2020). Change in forest condition: Characterizing non-stand replacing disturbances using time series satellite imagery. *Forest Ecology and Management*, 474, 118370. <https://doi.org/10.1016/j.foreco.2020.118370>
- Copernicus DEM. (2021). Global and European Digital Elevation Model (COP-DEM). <https://doi.org/https://doi.org/10.5270/ESA-c5d3d65>
- Cortes, C., & Vapnik, V. (1995). Support-vector networks. *Machine Learning*, 20(3), 273–297. <https://doi.org/10.1007/BF00994018>
- Csillik, O., Cherbini, J., Johnson, R., Lyons, A., & Kelly, M. (2018). Identification of Citrus Trees from Unmanned Aerial Vehicle Imagery Using Convolutional Neural Networks. *Drones*, 2(4), 39. <https://doi.org/10/gh3dp9>
- Depauw, L., De Lombaerde, E., Dhiedt, E., Blondeel, H., Abdala-Roberts, L., Auge, H., Barsoum, N., Bauhus, J., Chu, C., Damtew, A., Eisenhauer, N., Fagundes, M. V., Ganade, G., Gendreau-Berthiaume, B., Godbold, D., Gravel,

- D., Guillemot, J., Hajek, P., Hector, A., . . . Baeten, L. (2024). Enhancing Tree Performance Through Species Mixing: Review of a Quarter-Century of TreeDivNet Experiments Reveals Research Gaps and Practical Insights. *Current Forestry Reports*, 10(1), 1–20. <https://doi.org/10.1007/s40725-023-00208-y>
- DWD. (2023a). *Annual grids of number of hot days over Germany (Version 1.0)*. Climate Data Center (CDC). Retrieved August 10, 2023, from https://opendata.dwd.de/climate_environment/CDC/grids_germany/annual/hot_days/
- DWD. (2023b). *Annual grids of the begin of the vegetation period in Germany (Version 0.x)*. Climate Data Center (CDC). Retrieved August 10, 2023, from https://opendata.dwd.de/climate_environment/CDC/grids_germany/annual/vegetation_begin/
- DWD. (2023c). *Grids of monthly averaged daily minimum air temperature (2m) over Germany (Version 1.0)*. Climate Data Center (CDC). Retrieved August 10, 2023, from https://opendata.dwd.de/climate_environment/CDC/grids_germany/monthly/air_temperature_min/
- DWD. (2023d). *Grids of monthly total precipitation over Germany (Version 1.0)*. Climate Data Center (CDC). Retrieved August 10, 2023, from https://opendata.dwd.de/climate_environment/CDC/grids_germany/monthly/precipitation/
- DWD. (2023e). *Monthly grids of the accumulated potential evapotranspiration over grass (Version 0.x)*. Climate Data Center (CDC). Retrieved August 10, 2023, from https://opendata.dwd.de/climate_environment/CDC/grids_germany/monthly/evapo_p/
- DWD. (2023f). *Multi-annual grids of water balance over Germany (Version 1.0)*. Climate Data Center (CDC). Retrieved August 10, 2023, from https://opendata.dwd.de/climate_environment/CDC/grids_germany/multi_annual/water_balance/
- Einzmann, K., Atzberger, C., Pinnel, N., Glas, C., Böck, S., Seitz, R., & Immitzer, M. (2021). Early detection of spruce vitality loss with hyperspectral data: Results of an experimental study in Bavaria, Germany. *Remote Sensing of Environment*, 266, 112676. <https://doi.org/10.1016/j.rse.2021.112676>
- FAO. (2020). *Global Forest Resources Assessment 2020: Key findings*. Retrieved February 16, 2021, from <https://doi.org/10.4060/ca8753en>
- FAO & UNEP. (2020). *The State of the World's Forests 2020. Forests, biodiversity and people*. Retrieved June 6, 2024, from <https://openknowledge.fao.org/handle/20.500.14283/ca8642en>
- Fassnacht, F. E., Latifi, H., Ghosh, A., Joshi, P. K., & Koch, B. (2014). Assessing the potential of hyperspectral imagery to map bark beetle-induced tree mortality. *Remote Sensing of Environment*, 140, 533–548. <https://doi.org/10.1016/j.rse.2013.09.014>
- Fassnacht, F. E., Latifi, H., Stereńczak, K., Modzelewska, A., Lefsky, M., Waser, L. T., Straub, C., & Ghosh, A. (2016). Review of studies on tree species

-
- classification from remotely sensed data. *Remote Sensing of Environment*, 186, 64–87. <https://doi.org/10/gddm6t>
- Fassnacht, F. E., White, J. C., Wulder, M. A., & Næsset, E. (2023). Remote sensing in forestry: current challenges, considerations and directions. *Forestry: An International Journal of Forest Research*, cpado24. <https://doi.org/10.1093/forestry/cpado24>
- Ferreira, M. P., Lotte, R. G., D’Elia, F. V., Stamatopoulos, C., Kim, D.-H., & Benjamin, A. R. (2021). Accurate mapping of Brazil nut trees (*Bertholletia excelsa*) in Amazonian forests using WorldView-3 satellite images and convolutional neural networks. *Ecological Informatics*, 63, 101302. <https://doi.org/10/gjq399>
- Fick, S. E., & Hijmans, R. J. (2017). WorldClim 2: new 1-km spatial resolution climate surfaces for global land areas. *International Journal of Climatology*, 37(12), 4302–4315. <https://doi.org/10.1002/joc.5086>
- Fischer, M., Bossdorf, O., Gockel, S., Hänsel, F., Hemp, A., Hessenmöller, D., Korte, G., Nieschulze, J., Pfeiffer, S., Prati, D., Renner, S., Schöning, I., Schumacher, U., Wells, K., Buscot, F., Kalko, E. K. V., Linsenmair, K. E., Schulze, E.-D., & Weisser, W. W. (2010). Implementing large-scale and long-term functional biodiversity research: The Biodiversity Exploratories. *Basic and Applied Ecology*, 11(6), 473–485. <https://doi.org/10/dqn5gx>
- Fischer, W. A., Hemphill, W. R., & Kover, A. (1976). Progress in remote sensing (1972–1976). *Photogrammetria*, 32(2), 33–72. [https://doi.org/10.1016/0031-8663\(76\)90013-2](https://doi.org/10.1016/0031-8663(76)90013-2)
- Fisichelli, N., Vor, T., & Ammer, C. (2014). Broadleaf seedling responses to warmer temperatures “chilled” by late frost that favors conifers. *European Journal of Forest Research*, 133(4), 587–596. <https://doi.org/10.1007/s10342-014-0786-6>
- Francini, S., McRoberts, R. E., Giannetti, F., Mencucci, M., Marchetti, M., Scarascia Mugnozza, G., & Chirici, G. (2020). Near-real time forest change detection using PlanetScope imagery. *European Journal of Remote Sensing*, 53(1), 233–244. <https://doi.org/10.1080/22797254.2020.1806734>
- Franklin, S. E., & Ahmed, O. S. (2018). Deciduous tree species classification using object-based analysis and machine learning with unmanned aerial vehicle multispectral data. *International Journal of Remote Sensing*, 39(15), 5236–5245. <https://doi.org/10/gh3dn8>
- Frantz, D. (2019). FORCE—Landsat + Sentinel-2 Analysis Ready Data and Beyond. *Remote Sensing*, 11(9), 1124. <https://doi.org/10.3390/rs11091124>
- Frantz, D., Hostert, P., Rufin, P., Ernst, S., Röder, A., & van der Linden, S. (2022). Revisiting the Past: Replicability of a Historic Long-Term Vegetation Dynamics Assessment in the Era of Big Data Analytics. *Remote Sensing*, 14(3), 597. <https://doi.org/10/gpcf37>

- Freudenberg, M., Nölke, N., Agostini, A., Urban, K., Wörgötter, F., & Kleinn, C. (2019). Large Scale Palm Tree Detection in High Resolution Satellite Images Using U-Net. *Remote Sensing*, *11*(3), 312. <https://doi.org/10/gh3dqt>
- Frey, J., Kovach, K., Stemmler, S., & Koch, B. (2018). UAV Photogrammetry of Forests as a Vulnerable Process. A Sensitivity Analysis for a Structure from Motion RGB-Image Pipeline. *Remote Sensing*, *10*(6), 912. <https://doi.org/10/gh3dkz>
- Fricker, G. A., Ventura, J. D., Wolf, J. A., North, M. P., Davis, F. W., & Franklin, J. (2019). A Convolutional Neural Network Classifier Identifies Tree Species in Mixed-Conifer Forest from Hyperspectral Imagery. *Remote Sensing*, *11*(19), 2326. <https://doi.org/10/gh3dqv>
- Friedman, J. H. (2001). Greedy function approximation: A gradient boosting machine. *The Annals of Statistics*, *29*(5), 1189–1232. <https://doi.org/10.1214/aos/1013203451>
- Frolking, S., Palace, M. W., Clark, D. B., Chambers, J. Q., Shugart, H. H., & Hurtt, G. C. (2009). Forest disturbance and recovery: A general review in the context of spaceborne remote sensing of impacts on aboveground biomass and canopy structure. *Journal of Geophysical Research: Biogeosciences*, *114*. <https://doi.org/10.1029/2008JG000911>
- Fromm, M., Schubert, M., Castilla, G., Linke, J., & McDermid, G. (2019). Automated Detection of Conifer Seedlings in Drone Imagery Using Convolutional Neural Networks. *Remote Sensing*, *11*(21), 2585. <https://doi.org/10/gh3dqw>
- Galiatsatos, N., Donoghue, D. N. M., Watt, P., Bholanath, P., Pickering, J., Hansen, M. C., & Mahmood, A. R. J. (2020). An Assessment of Global Forest Change Datasets for National Forest Monitoring and Reporting. *Remote Sensing*, *12*(11), 1790. <https://doi.org/10.3390/rs12111790>
- Gao, B.-c. (1996). NDWI—A normalized difference water index for remote sensing of vegetation liquid water from space. *Remote Sensing of Environment*, *58*(3), 257–266. [https://doi.org/10.1016/S0034-4257\(96\)00067-3](https://doi.org/10.1016/S0034-4257(96)00067-3)
- Garrity, S. R., Allen, C. D., Brumby, S. P., Gangodagamage, C., McDowell, N. G., & Cai, D. M. (2013). Quantifying tree mortality in a mixed species woodland using multitemporal high spatial resolution satellite imagery. *Remote Sensing of Environment*, *129*, 54–65. <https://doi.org/10.1016/j.rse.2012.10.029>
- Gascon, F., Bouzinac, C., Thépaut, O., Jung, M., Francesconi, B., Louis, J., Lonjou, V., Lafrance, B., Massera, S., Gaudel-Vacaresse, A., Languille, F., Alhammoud, B., Viallefont, F., Pflug, B., Bieniarz, J., Clerc, S., Pessiot, L., Trémas, T., Cadau, E., ... Fernandez, V. (2017). Copernicus Sentinel-2A Calibration and Products Validation Status. *Remote Sensing*, *9*(6), 584. <https://doi.org/10.3390/rs9060584>
- GFW. (2023, January 21). Global Forest Watch: Tree cover loss in Germany. www.globalforestwatch.org

-
- Gini, R., Passoni, D., Pinto, L., & Sona, G. (2014). Use of Unmanned Aerial Systems for multispectral survey and tree classification: a test in a park area of northern Italy. *European Journal of Remote Sensing*, 47(1), 251–269. <https://doi.org/10/gh3c7c>
- Glenn, E. P., Huete, A. R., Nagler, P. L., & Nelson, S. G. (2008). Relationship Between Remotely-sensed Vegetation Indices, Canopy Attributes and Plant Physiological Processes: What Vegetation Indices Can and Cannot Tell Us About the Landscape. *Sensors*, 8(4), 2136–2160. <https://doi.org/10.3390/s8042136>
- Gora, E. M., & Esquivel-Muelbert, A. (2021). Implications of size-dependent tree mortality for tropical forest carbon dynamics. *Nature Plants*, 7(4), 384–391. <https://doi.org/10.1038/s41477-021-00879-0>
- Gorelick, N., Hancher, M., Dixon, M., Ilyushchenko, S., Thau, D., & Moore, R. (2017). Google Earth Engine: Planetary-scale geospatial analysis for everyone. *Remote Sensing of Environment*, 202, 18–27. <https://doi.org/10.1016/j.rse.2017.06.031>
- Gränzig, T., Fassnacht, F. E., Kleinschmit, B., & Förster, M. (2021). Mapping the fractional coverage of the invasive shrub *Ulex europaeus* with multi-temporal Sentinel-2 imagery utilizing UAV orthoimages and a new spatial optimization approach. *International Journal of Applied Earth Observation and Geoinformation*, 96, 102281. <https://doi.org/10/gh3ctq>
- Grossiord, C., Buckley, T. N., Cernusak, L. A., Novick, K. A., Poulter, B., Siegwolf, R. T. W., Sperry, J. S., & McDowell, N. G. (2020). Plant responses to rising vapor pressure deficit. *New Phytologist*, 226(6), 1550–1566. <https://doi.org/10.1111/nph.16485>
- Grossiord, C., Granier, A., Ratcliffe, S., Bouriaud, O., Bruelheide, H., Čečko, E., Forrester, D. I., Dawud, S. M., Finér, L., Pollastrini, M., Scherer-Lorenzen, M., Valladares, F., Bonal, D., & Gessler, A. (2014). Tree diversity does not always improve resistance of forest ecosystems to drought. *Proceedings of the National Academy of Sciences*, 111(41), 14812–14815. <https://doi.org/10.1073/pnas.1411970111>
- Hajek, P., Mörsdorf, M., Kovach, K. R., Greinwald, K., Rose, L., Nock, C. A., & Scherer-Lorenzen, M. (2023). Quantifying the influence of tree species richness on community drought resistance using drone-derived NDVI and ground-based measures of Plant Area Index and leaf chlorophyll in a young tree diversity experiment. *European Journal of Forest Research*. <https://doi.org/10.1007/s10342-023-01615-3>
- Hamdi, Z. M., Brandmeier, M., & Straub, C. (2019). Forest Damage Assessment Using Deep Learning on High Resolution Remote Sensing Data. *Remote Sensing*, 11(17), 1976. <https://doi.org/10/gh3dqj>
- Hammond, W. M., Williams, A. P., Abatzoglou, J. T., Adams, H. D., Klein, T., López, R., Sáenz-Romero, C., Hartmann, H., Breshears, D. D., & Allen,

- C. D. (2022). Global field observations of tree die-off reveal hotter-drought fingerprint for Earth's forests. *Nature Communications*, 13(1), 1761. <https://doi.org/10.1038/s41467-022-29289-2>
- Hansen, M. C., Potapov, P. V., Moore, R., Hancher, M., Turubanova, S. A., Tyukavina, A., Thau, D., Stehman, S. V., Goetz, S. J., Loveland, T. R., Kommareddy, A., Egorov, A., Chini, L., Justice, C. O., & Townshend, J. R. G. (2013). High-Resolution Global Maps of 21st-Century Forest Cover Change. *Science*, 342(6160), 850–853. <https://doi.org/10/f5h5c2>
- Hari, V., Rakovec, O., Markonis, Y., Hanel, M., & Kumar, R. (2020). Increased future occurrences of the exceptional 2018–2019 Central European drought under global warming. *Scientific Reports*, 10(1), 12207. <https://doi.org/10.1038/s41598-020-68872-9>
- Hart, S. J., & Veblen, T. T. (2015). Detection of spruce beetle-induced tree mortality using high- and medium-resolution remotely sensed imagery. *Remote Sensing of Environment*, 168, 134–145. <https://doi.org/10.1016/j.rse.2015.06.015>
- Hartling, S., Sagan, V., Sidike, P., Maimaitjiang, M., & Carron, J. (2019). Urban Tree Species Classification Using a WorldView-2/3 and LiDAR Data Fusion Approach and Deep Learning. *Sensors*, 19(6), 1284. <https://doi.org/10/g3dmn>
- Hartmann, H., Bastos, A., Das, A. J., Esquivel-Muelbert, A., Hammond, W. M., Martínez-Vilalta, J., McDowell, N. G., Powers, J. S., Pugh, T. A., Ruthrof, K. X., & Allen, C. D. (2022). Climate Change Risks to Global Forest Health: Emergence of Unexpected Events of Elevated Tree Mortality Worldwide. *Annual Review of Plant Biology*, 73(1), 673–702. <https://doi.org/10.1146/annurev-arplant-102820-012804>
- Hartmann, H., Moura, C. F., Anderegg, W. R. L., Ruehr, N. K., Salmon, Y., Allen, C. D., Arndt, S. K., Breshears, D. D., Davi, H., Galbraith, D., Ruthrof, K. X., Wunder, J., Adams, H. D., Bloemen, J., Cailleret, M., Cobb, R., Gessler, A., Grams, T. E. E., Jansen, S., ... O'Brien, M. (2018a). Research frontiers for improving our understanding of drought-induced tree and forest mortality. *New Phytologist*, 218(1), 15–28. <https://doi.org/10.1111/nph.15048>
- Hartmann, H., Schuldt, B., Sanders, T. G. M., Macinnis-Ng, C., Boehmer, H. J., Allen, C. D., Bolte, A., Crowther, T. W., Hansen, M. C., Medlyn, B. E., Ruehr, N. K., & Anderegg, W. R. L. (2018b). Monitoring global tree mortality patterns and trends. Report from the VW symposium 'Crossing scales and disciplines to identify global trends of tree mortality as indicators of forest health'. *New Phytologist*, 217(3), 984–987. <https://doi.org/10/gn93j8>
- Haynes, K. J., Allstadt, A. J., & Klimetzek, D. (2014). Forest defoliator outbreaks under climate change: effects on the frequency and severity of outbreaks of five pine insect pests. *Global Change Biology*, 20(6), 2004–2018. <https://doi.org/10.1111/gcb.12506>

-
- Hell, M., Brandmeier, M., Briechle, S., & Krzystek, P. (2022). Classification of Tree Species and Standing Dead Trees with Lidar Point Clouds Using Two Deep Neural Networks: PointCNN and 3DmFV-Net. *PGF – Journal of Photogrammetry, Remote Sensing and Geoinformation Science*, 90(2), 103–121. <https://doi.org/10.1007/s41064-022-00200-4>
- Hengl, T. & Parente, L. (2022). Soil sand content [%] for continental Europe at 30 m spatial resolution for period 2000-2020: Open Soil Data Cube for Europe. <https://doi.org/10.5281/zenodo.6574856>
- Hochreiter, S., & Schmidhuber, J. (1997). Long Short-Term Memory. *Neural Computation*, 9(8), 1735–1780. <https://doi.org/10.1162/neco.1997.9.8.1735>
- Hoeser, T., & Kuenzer, C. (2020). Object Detection and Image Segmentation with Deep Learning on Earth Observation Data: A Review-Part I: Evolution and Recent Trends. *Remote Sensing*, 12(10), 1667. <https://doi.org/10.3390/rs12101667>
- Hu, W.-S., Li, H.-C., Pan, L., Li, W., Tao, R., & Du, Q. (2020). Spatial-Spectral Feature Extraction via Deep ConvLSTM Neural Networks for Hyperspectral Image Classification. *IEEE Transactions on Geoscience and Remote Sensing*, 58(6), 4237–4250. <https://doi.org/10.1109/TGRS.2019.2961947>
- Huang, J., Kautz, M., Trowbridge, A. M., Hammerbacher, A., Raffa, K. F., Adams, H. D., Goodsman, D. W., Xu, C., Meddens, A. J. H., Kandasamy, D., Gershenson, J., Seidl, R., & Hartmann, H. (2020). Tree defence and bark beetles in a drying world: carbon partitioning, functioning and modelling. *New Phytologist*, 225(1), 26–36. <https://doi.org/10.1111/nph.16173>
- Hufkens, K., Friedl, M., Sonnentag, O., Braswell, B. H., Milliman, T., & Richardson, A. D. (2012). Linking near-surface and satellite remote sensing measurements of deciduous broadleaf forest phenology. *Remote Sensing of Environment*, 117, 307–321. <https://doi.org/10.1016/j.rse.2011.10.006>
- Jactel, H., Moreira, X., & Castagnyrol, B. (2021). Tree Diversity and Forest Resistance to Insect Pests: Patterns, Mechanisms, and Prospects. *Annual Review of Entomology*, 66, 277–296. <https://doi.org/10.1146/annurev-ento-041720-075234>
- Jégou, S., Drozdal, M., Vazquez, D., Romero, A., & Bengio, Y. (2017). The One Hundred Layers Tiramisu: Fully Convolutional DenseNets for Semantic Segmentation. *2017 IEEE Conference on Computer Vision and Pattern Recognition Workshops (CVPRW)*, 1175–1183. <https://doi.org/10/ghm4tr>
- Jiang, S., Yao, W., & Heurich, M. (2019). Dead wood detection based on semantic segmentation of VHR aerial CIR imagery using optimized FCN-Densenet. *The International Archives of the Photogrammetry, Remote Sensing and Spatial Information Sciences*, XLII-2-W16, 127–133. <https://doi.org/10.5194/isprs-archives-XLII-2-W16-127-2019>
- Jones, H. G., & Vaughan, R. A. (2010). *Remote Sensing of Vegetation: Principles, Techniques, and Applications*. Oxford University Press.

- Joyce, K. E., Anderson, K., & Bartolo, R. E. (2021). Of Course We Fly Unmanned—We're Women! *Drones*, 5(1), 21. <https://doi.org/10.3390/drones5010021>
- Jump, A. S., Ruiz-Benito, P., Greenwood, S., Allen, C. D., Kitzberger, T., Fensham, R., Martínez-Vilalta, J., & Lloret, F. (2017). Structural overshoot of tree growth with climate variability and the global spectrum of drought-induced forest dieback. *Global Change Biology*, 23(9), 3742–3757. <https://doi.org/10.1111/gcb.13636>
- Kaartinen, H., Hyyppä, J., Vastaranta, M., Kukko, A., Jaakkola, A., Yu, X., Pyörälä, J., Liang, X., Liu, J., Wang, Y., Kajaluoto, R., Melkas, T., Holopainen, M., & Hyyppä, H. (2015). Accuracy of Kinematic Positioning Using Global Satellite Navigation Systems under Forest Canopies. *Forests*, 6(9), 3218–3236. <https://doi.org/10/f7v2tp>
- Kändler, G., & Cullmann, D. (2015). *Regionale Auswertung der Bundeswaldinventur 3. Wuchsgebiet Schwarzwald*. Forstliche Versuchs- und Forschungsanstalt Baden-Württemberg (FVA). Freiburg, Germany. Retrieved January 23, 2024, from https://www.fva-bw.de/fileadmin/user_upload/Daten_und_Tools/Monitoring/BWI/Ergebnisse_BWI3/Wuchsgebiet_Schwarzwald.pdf
- Kattenborn, T., Eichel, J., & Fassnacht, F. E. (2019a). Convolutional Neural Networks enable efficient, accurate and fine-grained segmentation of plant species and communities from high-resolution UAV imagery. *Scientific Reports*, 9(1), 17656. <https://doi.org/10/gh3dqn>
- Kattenborn, T., Eichel, J., Wisser, S., Burrows, L., Fassnacht, F. E., & Schmidlein, S. (2020). Convolutional Neural Networks accurately predict cover fractions of plant species and communities in Unmanned Aerial Vehicle imagery. *Remote Sensing in Ecology and Conservation*, 6(4), 472–486. <https://doi.org/10/gh3dqv>
- Kattenborn, T., Leitloff, J., Schiefer, F., & Hinz, S. (2021). Review on Convolutional Neural Networks (CNN) in vegetation remote sensing. *ISPRS Journal of Photogrammetry and Remote Sensing*, 173, 24–49. <https://doi.org/10/ghtrws>
- Kattenborn, T., Lopatin, J., Förster, M., Braun, A. C., & Fassnacht, F. E. (2019b). UAV data as alternative to field sampling to map woody invasive species based on combined Sentinel-1 and Sentinel-2 data. *Remote Sensing of Environment*, 227, 61–73. <https://doi.org/10/ghrvsr>
- Kattenborn, T., Schiefer, F., Frey, J., Feilhauer, H., Mahecha, M. D., & Dormann, C. F. (2022). Spatially autocorrelated training and validation samples inflate performance assessment of convolutional neural networks. *ISPRS Open Journal of Photogrammetry and Remote Sensing*, 5, 100018. <https://doi.org/10.1016/j.ophoto.2022.100018>
- Kattge, J., Bönsch, G., Díaz, S., Lavorel, S., Prentice, I. C., Leadley, P., Tautenhahn, S., Werner, G. D. A., Aakala, T., Abedi, M., Acosta, A. T. R., Adamidis, G. C., Adamson, K., Aiba, M., Albert, C. H., Alcántara, J. M., Alcázar C, C., Aleixo, I., Ali, H., ... Wirth, C. (2020). TRY plant trait database –

-
- enhanced coverage and open access. *Global Change Biology*, 26(1), 119–188. <https://doi.org/10.1111/gcb.14904>
- Khatri-Chhetri, P., van Wagtenonk, L., Hendryx, S. M., & Kane, V. R. (2024). Enhancing individual tree mortality mapping: The impact of models, data modalities, and classification taxonomy. *Remote Sensing of Environment*, 300, 113914. <https://doi.org/10.1016/j.rse.2023.113914>
- Killough, B. (2018). Overview of the Open Data Cube Initiative. *IGARSS 2018 - 2018 IEEE International Geoscience and Remote Sensing Symposium*, 8629–8632. <https://doi.org/10.1109/IGARSS.2018.8517694>
- Kislov, D. E., & Korznikov, K. A. (2020). Automatic Windthrow Detection Using Very-High-Resolution Satellite Imagery and Deep Learning. *Remote Sensing*, 12(7), 1145. <https://doi.org/10/gh3dns>
- Komárek, J. (2020). The perspective of unmanned aerial systems in forest management: Do we really need such details? *Applied Vegetation Science*, 23(4), 718–721. <https://doi.org/10/gh3c6x>
- Kong, Y.-L., Huang, Q., Wang, C., Chen, J., Chen, J., & He, D. (2018). Long Short-Term Memory Neural Networks for Online Disturbance Detection in Satellite Image Time Series. *Remote Sensing*, 10(3), 452. <https://doi.org/10.3390/rs10030452>
- Kulha, N., Honkaniemi, J., Barrere, J., Brandl, S., Cordonnier, T., Korhonen, K. T., Kunstler, G., Paul, C., Reineking, B., & Peltoniemi, M. (2023). Competition-induced tree mortality across Europe is driven by shade tolerance, proportion of conspecifics and drought. *Journal of Ecology*, 111(10), 2310–2323. <https://doi.org/10.1111/1365-2745.14184>
- Labenski, P., Ewald, M., Schmidlein, S., & Fassnacht, F. E. (2022). Classifying surface fuel types based on forest stand photographs and satellite time series using deep learning. *International Journal of Applied Earth Observation and Geoinformation*, 109, 102799. <https://doi.org/10.1016/j.jag.2022.102799>
- Labenski, P., Ewald, M., Schmidlein, S., Heinsch, F. A., & Fassnacht, F. E. (2023). Quantifying surface fuels for fire modelling in temperate forests using airborne lidar and Sentinel-2: potential and limitations. *Remote Sensing of Environment*, 295, 113711. <https://doi.org/10.1016/j.rse.2023.113711>
- Lang, N., Jetz, W., Schindler, K., & Wegner, J. D. (2023). A high-resolution canopy height model of the Earth. *Nature Ecology & Evolution*, 7(11), 1778–1789. <https://doi.org/10.1038/s41559-023-02206-6>
- Lefèvre, S., Tuia, D., Wegner, J. D., Produit, T., & Nassar, A. S. (2017). Toward Seamless Multiview Scene Analysis From Satellite to Street Level. *Proceedings of the IEEE*, 105(10), 1884–1899. <https://doi.org/10.1109/JPROC.2017.2684300>
- Leitão, P. J., Schwieder, M., Pötzschner, F., Pinto, J. R. R., Teixeira, A. M. C., Pedroni, F., Sanchez, M., Rogass, C., Linden, S. v. d., Bustamante, M. M. C., & Hostert, P. (2018). From sample to pixel: multi-scale remote sensing

- data for upscaling aboveground carbon data in heterogeneous landscapes. *Ecosphere*, 9(8), e02298. <https://doi.org/10/gfmb5q>
- Lepš, J., & Hadincová, V. (1992). How reliable are our vegetation analyses? *Journal of Vegetation Science*, 3(1), 119–124. <https://doi.org/10.2307/3236006>
- Li, Q., Tian, J., & Tian, Q. (2023). Deep Learning Application for Crop Classification via Multi-Temporal Remote Sensing Images. *Agriculture*, 13(4), 906. <https://doi.org/10.3390/agriculture13040906>
- Li, W., Fu, H., Yu, L., & Cracknell, A. (2017). Deep Learning Based Oil Palm Tree Detection and Counting for High-Resolution Remote Sensing Images. *Remote Sensing*, 9(1), 22. <https://doi.org/10/gh3dp3>
- Lillesand, T. M., Kiefer, R. W., & Chipman, J. W. (2015). *Remote sensing and image interpretation* (Seventh edition). John Wiley & Sons, Inc.
- Lindner, M., Fitzgerald, J. B., Zimmermann, N. E., Reyer, C., Delzon, S., van der Maaten, E., Schelhaas, M.-J., Lasch, P., Eggers, J., van der Maaten-Theunissen, M., Suckow, F., Psomas, A., Poulter, B., & Hanewinkel, M. (2014). Climate change and European forests: What do we know, what are the uncertainties, and what are the implications for forest management? *Journal of Environmental Management*, 146, 69–83. <https://doi.org/10.1016/j.jenvman.2014.07.030>
- Liu, X., Frey, J., Denter, M., Zielewska-Büttner, K., Still, N., & Koch, B. (2021). Mapping standing dead trees in temperate montane forests using a pixel- and object-based image fusion method and stereo WorldView-3 imagery. *Ecological Indicators*, 133, 108438. <https://doi.org/10.1016/j.ecolind.2021.108438>
- Liu, X., Huang, Y., Chen, L., Li, S., Bongers, F. J., Castro-Izaguirre, N., Liang, Y., Yang, B., Chen, Y., Schnabel, F., Tang, T., Xue, Y., Trogisch, S., Staab, M., Bruelheide, H., Schmid, B., & Ma, K. (2022). Species richness, functional traits and climate interactively affect tree survival in a large forest biodiversity experiment. *Journal of Ecology*, 110(10), 2522–2531. <https://doi.org/10.1111/1365-2745.13970>
- Lobo Torres, D., Queiroz Feitosa, R., Nigri Happ, P., Elena Cué La Rosa, L., Marcato Junior, J., Martins, J., Olã Bressan, P., Gonçalves, W. N., & Liesenberg, V. (2020). Applying Fully Convolutional Architectures for Semantic Segmentation of a Single Tree Species in Urban Environment on High Resolution UAV Optical Imagery. *Sensors*, 20(2), 563. <https://doi.org/10/ghm4s6>
- López-Jiménez, E., Vasquez-Gomez, J. I., Sanchez-Acevedo, M. A., Herrera-Lozada, J. C., & Uriarte-Arcia, A. V. (2019). Columnar cactus recognition in aerial images using a deep learning approach. *Ecological Informatics*, 52, 131–138. <https://doi.org/10/gh3dms>
- Lowe, D. G. (2004). Distinctive Image Features from Scale-Invariant Keypoints. *International Journal of Computer Vision*, 60(2), 91–110. <https://doi.org/10.1023/B:VISI.0000029664.99615.94>

-
- Ma, L., Liu, Y., Zhang, X., Ye, Y., Yin, G., & Johnson, B. A. (2019). Deep learning in remote sensing applications: A meta-analysis and review. *ISPRS Journal of Photogrammetry and Remote Sensing*, 152, 166–177. <https://doi.org/10/gf3s65>
- Main-Knorn, M., Pflug, B., Louis, J., Debaecker, V., Müller-Wilm, U., & Gascon, F. (2017). Sen2Cor for Sentinel-2. *Image and Signal Processing for Remote Sensing XXIII*, 10427, 37–48. <https://doi.org/10/gm2trw>
- Marconi, S., Weinstein, B. G., Zou, S., Bohlman, S. A., Zare, A., Singh, A., Stewart, D., Harmon, I., Steinkraus, A., & White, E. P. (2022). Continental-scale hyperspectral tree species classification in the United States National Ecological Observatory Network. *Remote Sensing of Environment*, 282, 113264. <https://doi.org/10.1016/j.rse.2022.113264>
- McDowell, N. G., Allen, C. D., Anderson-Teixeira, K., Aukema, B. H., Bond-Lamberty, B., Chini, L., Clark, J. S., Dietze, M., Grossiord, C., Hanbury-Brown, A., Hurtt, G. C., Jackson, R. B., Johnson, D. J., Kueppers, L., Lichstein, J. W., Ogle, K., Poulter, B., Pugh, T. A. M., Seidl, R., ... Xu, C. (2020). Pervasive shifts in forest dynamics in a changing world. *Science*, 368(6494), eaaz9463. <https://doi.org/10.1126/science.aaz9463>
- McDowell, N. G., Coops, N. C., Beck, P. S. A., Chambers, J. Q., Gangodagamage, C., Hicke, J. A., Huang, C.-y., Kennedy, R., Krofcheck, D. J., Litvak, M., Meddens, A. J. H., Muss, J., Negrón-Juarez, R., Peng, C., Schwantes, A. M., Swenson, J. J., Vernon, L. J., Williams, A. P., Xu, C., ... Allen, C. D. (2015). Global satellite monitoring of climate-induced vegetation disturbances. *Trends in Plant Science*, 20(2), 114–123. <https://doi.org/10/f62b9j>
- McDowell, N. G., Sapes, G., Pivovarov, A., Adams, H. D., Allen, C. D., Anderegg, W. R. L., Arend, M., Breshears, D. D., Brodribb, T., Choat, B., Cochard, H., De Cáceres, M., De Kauwe, M. G., Grossiord, C., Hammond, W. M., Hartmann, H., Hoch, G., Kahmen, A., Klein, T., ... Xu, C. (2022). Mechanisms of woody-plant mortality under rising drought, CO₂ and vapour pressure deficit. *Nature Reviews Earth & Environment*, 3(5), 294–308. <https://doi.org/10.1038/s43017-022-00272-1>
- Meddens, A. J. H., Hicke, J. A., & Vierling, L. A. (2011). Evaluating the potential of multispectral imagery to map multiple stages of tree mortality. *Remote Sensing of Environment*, 115(7), 1632–1642. <https://doi.org/10.1016/j.rse.2011.02.018>
- Meddens, A. J. H., Hicke, J. A., Vierling, L. A., & Hudak, A. T. (2013). Evaluating methods to detect bark beetle-caused tree mortality using single-date and multi-date Landsat imagery. *Remote Sensing of Environment*, 132, 49–58. <https://doi.org/10.1016/j.rse.2013.01.002>
- Meng, R., Wu, J., Zhao, F., Cook, B. D., Hanavan, R. P., & Serbin, S. P. (2018). Measuring short-term post-fire forest recovery across a burn severity gradient in a mixed pine-oak forest using multi-sensor remote sensing techniques.

- Remote Sensing of Environment*, 210, 282–296. <https://doi.org/10.1016/j.rse.2018.03.019>
- Meraner, A., Ebel, P., Zhu, X. X., & Schmitt, M. (2020). Cloud removal in Sentinel-2 imagery using a deep residual neural network and SAR-optical data fusion. *ISPRS Journal of Photogrammetry and Remote Sensing*, 166, 333–346. <https://doi.org/10.1016/j.isprsjprs.2020.05.013>
- Messier, C., Bauhus, J., Sousa-Silva, R., Auge, H., Baeten, L., Barsoum, N., Brulheide, H., Caldwell, B., Cavender-Bares, J., Dhiedt, E., Eisenhauer, N., Ganade, G., Gravel, D., Guillemot, J., Hall, J. S., Hector, A., Hérault, B., Jactel, H., Koricheva, J., . . . Zemp, D. C. (2022). For the sake of resilience and multifunctionality, let's diversify planted forests! *Conservation Letters*, 15(1), e12829. <https://doi.org/10.1111/conl.12829>
- Meynen, E., & Schmithüsen, J. (Eds.). (1953). *Handbuch der naturräumlichen Gliederung Deutschlands* (Vol. 1-9). Selbstverl. der Bundesanst. für Landeskunde, Selbstverl. der Bundesanst. für Landeskunde und Raumforschung.
- Michez, A., Piégay, H., Lisein, J., Claessens, H., & Lejeune, P. (2016). Classification of riparian forest species and health condition using multi-temporal and hyperspatial imagery from unmanned aerial system. *Environmental Monitoring and Assessment*, 188(3), 146. <https://doi.org/10/f8q9wp>
- Milodowski, D. T., Mitchard, E. T. A., & Williams, M. (2017). Forest loss maps from regional satellite monitoring systematically underestimate deforestation in two rapidly changing parts of the Amazon. *Environmental Research Letters*, 12(9), 094003. <https://doi.org/10.1088/1748-9326/aa7e1e>
- Molnar, C., Casalicchio, G., & Bischl, B. (2018). iml: An R package for Interpretable Machine Learning. *Journal of Open Source Software*, 3(26), 786. <https://doi.org/10.21105/joss.00786>
- Monahan, W. B., Arnspiger, C. E., Bhatt, P., An, Z., Krist, F. J., Liu, T., Richard, R. P., Edson, C., Froese, R. E., Steffenson, J., Lammers, T. C., & Frosh, R. (2022). A spectral three-dimensional color space model of tree crown health. *PLOS ONE*, 17(10), e0272360. <https://doi.org/10.1371/journal.pone.0272360>
- Morales, G., Kemper, G., Sevillano, G., Arteaga, D., Ortega, I., & Telles, J. (2018). Automatic Segmentation of *Mauritia flexuosa* in Unmanned Aerial Vehicle (UAV) Imagery Using Deep Learning. *Forests*, 9(12), 736. <https://doi.org/10/gh3c6w>
- Müller, K., & Wickham, H. (2019, June 6). *tibble: Simple Data Frames* (Version 2.1.3). Retrieved January 23, 2024, from <https://cran.r-project.org/web/packages/tibble/index.html>
- Natesan, S., Armenakis, C., & Vepakomma, U. (2019). ResNet-based tree species classification using UAV images. *ISPRS - International Archives of the Photogrammetry, Remote Sensing and Spatial Information Sciences*, XLII-2-W13, 475–481. <https://doi.org/10/gh3dn7>

-
- Nevalainen, O., Honkavaara, E., Tuominen, S., Viljanen, N., Hakala, T., Yu, X., Hyyppä, J., Saari, H., Pölönen, I., Imai, N. N., & Tommaselli, A. M. G. (2017). Individual Tree Detection and Classification with UAV-Based Photogrammetric Point Clouds and Hyperspectral Imaging. *Remote Sensing*, 9(3), 185. <https://doi.org/10/f93bgd>
- Nezami, S., Khoramshahi, E., Nevalainen, O., Pölönen, I., & Honkavaara, E. (2020). Tree Species Classification of Drone Hyperspectral and RGB Imagery with Deep Learning Convolutional Neural Networks. *Remote Sensing*, 12(7), 1070. <https://doi.org/10/gh3dpx>
- Obladen, N., Dechering, P., Skiadaresis, G., Tegel, W., Keßler, J., Höllerl, S., Kaps, S., Hertel, M., Dulamsuren, C., Seifert, T., Hirsch, M., & Seim, A. (2021). Tree mortality of European beech and Norway spruce induced by 2018-2019 hot droughts in central Germany. *Agricultural and Forest Meteorology*, 307, 108482. <https://doi.org/10.1016/j.agrformet.2021.108482>
- Ollinger, S. V. (2011). Sources of variability in canopy reflectance and the convergent properties of plants. *New Phytologist*, 189(2), 375–394. <https://doi.org/10.1111/j.1469-8137.2010.03536.x>
- Oscó, L. P., Arruda, M. d. S. d., Marcato Junior, J., da Silva, N. B., Ramos, A. P. M., Moryia, É. A. S., Imai, N. N., Pereira, D. R., Creste, J. E., Matsubara, E. T., Li, J., & Gonçalves, W. N. (2020). A convolutional neural network approach for counting and geolocating citrus-trees in UAV multispectral imagery. *ISPRS Journal of Photogrammetry and Remote Sensing*, 160, 97–106. <https://doi.org/10/ghmdt9>
- Oscó, L. P., Marcato Junior, J., Marques Ramos, A. P., de Castro Jorge, L. A., Fatholahi, S. N., de Andrade Silva, J., Matsubara, E. T., Pistori, H., Gonçalves, W. N., & Li, J. (2021). A review on deep learning in UAV remote sensing. *International Journal of Applied Earth Observation and Geoinformation*, 102, 102456. <https://doi.org/10.1016/j.jag.2021.102456>
- Pause, M., Schweitzer, C., Rosenthal, M., Keuck, V., Bumberger, J., Dietrich, P., Heurich, M., Jung, A., & Lausch, A. (2016). In Situ/Remote Sensing Integration to Assess Forest Health—A Review. *Remote Sensing*, 8(6), 471. <https://doi.org/10.3390/rs8060471>
- Pelletier, C., Webb, G. I., & Petitjean, F. (2019a). Temporal Convolutional Neural Network for the Classification of Satellite Image Time Series. *Remote Sensing*, 11(5), 523. <https://doi.org/10.3390/rs11050523>
- Pelletier, C., Webb, G. I., & Petitjean, F. (2019b). Deep Learning for the Classification of Sentinel-2 Image Time Series. *IGARSS 2019 - 2019 IEEE International Geoscience and Remote Sensing Symposium*, 461–464. <https://doi.org/10/gkqvmm>
- Ploton, P., Mortier, F., Réjou-Méchain, M., Barbier, N., Picard, N., Rossi, V., Dormann, C., Cornu, G., Viennois, G., Bayol, N., Lyapustin, A., Gourlet-Fleury, S., & Péliissier, R. (2020). Spatial validation reveals poor predictive perfor-

- mance of large-scale ecological mapping models. *Nature Communications*, 11(1), 4540. <https://doi.org/10/ghbcv5>
- Pohl, F., Werban, U., Kumar, R., Hildebrandt, A., & Rebmann, C. (2023). Observational evidence of legacy effects of the 2018 drought on a mixed deciduous forest in Germany. *Scientific Reports*, 13(1), 10863. <https://doi.org/10.1038/s41598-023-38087-9>
- Popp, M. R., & Kalwij, J. M. (2023). Consumer-grade UAV imagery facilitates semantic segmentation of species-rich savanna tree layers. *Scientific Reports*, 13(1), 13892. <https://doi.org/10.1038/s41598-023-40989-7>
- Pretzsch, H., Biber, P., Schütze, G., Kemmerer, J., & Uhl, E. (2018). Wood density reduced while wood volume growth accelerated in Central European forests since 1870. *Forest Ecology and Management*, 429, 589–616. <https://doi.org/10.1016/j.foreco.2018.07.045>
- Qian, W., Huang, Y., Liu, Q., Fan, W., Sun, Z., Dong, H., Wan, F., & Qiao, X. (2020). UAV and a deep convolutional neural network for monitoring invasive alien plants in the wild. *Computers and Electronics in Agriculture*, 174, 105519. <https://doi.org/10/gh3dk2>
- R Core Team. (2020). *R: A language and environment for statistical computing*. R Foundation for Statistical Computing (Version 3.6.3). Vienna, Austria. <https://www.R-project.org/>
- R Core Team. (2022). *R: A language and environment for statistical computing*. R Foundation for Statistical Computing (Version 4.2.2). Vienna, Austria. <https://www.R-project.org/>
- Rakovec, O., Samaniego, L., Hari, V., Markonis, Y., Moravec, V., Thober, S., Hanel, M., & Kumar, R. (2022). The 2018–2020 Multi-Year Drought Sets a New Benchmark in Europe. *Earth's Future*, 10(3). <https://doi.org/10.1029/2021EF002394>
- Reeb, R. A., Aziz, N., Lapp, S. M., Kitzes, J., Heberling, J. M., & Kuebbing, S. E. (2022). Using Convolutional Neural Networks to Efficiently Extract Immense Phenological Data From Community Science Images. *Frontiers in Plant Science*, 12. <https://doi.org/10.3389/fpls.2021.787407>
- Reichstein, M., Camps-Valls, G., Stevens, B., Jung, M., Denzler, J., Carvalhais, N., & Prabhat. (2019). Deep learning and process understanding for data-driven Earth system science. *Nature*, 566(7743), 195–204. <https://doi.org/10/gfvhxx>
- Rezaee, M., Mahdianpari, M., Zhang, Y., & Salehi, B. (2018). Deep Convolutional Neural Network for Complex Wetland Classification Using Optical Remote Sensing Imagery. *IEEE Journal of Selected Topics in Applied Earth Observations and Remote Sensing*, 11(9), 3030–3039. <https://doi.org/10/gfbdd8>
- Roberts, D. R., Bahn, V., Ciuti, S., Boyce, M. S., Elith, J., Guillerá-Arroita, G., Hauenstein, S., Lahoz-Monfort, J. J., Schröder, B., Thuiller, W., Warton, D. I., Wintle, B. A., Hartig, F., & Dormann, C. F. (2017). Cross-validation

-
- strategies for data with temporal, spatial, hierarchical, or phylogenetic structure. *Ecography*, 40(8), 913–929. <https://doi.org/10.1111/ecog.02881>
- Ronneberger, O., Fischer, P., & Brox, T. (2015). U-Net: Convolutional Networks for Biomedical Image Segmentation. In N. Navab, J. Hornegger, W. M. Wells, & A. F. Frangi (Eds.), *Medical Image Computing and Computer-Assisted Intervention – MICCAI 2015* (pp. 234–241). Springer International Publishing. <https://doi.org/10/gcgk7j>
- Running, S. & Zhao, M. (2021). MODIS/Terra Net Primary Production Gap-Filled Yearly L4 Global 500m SIN Grid V061. <https://doi.org/10.5067/MODIS/MOD17A3HGF.061>
- Rußwurm, M., & Körner, M. (2017). Temporal Vegetation Modelling Using Long Short-Term Memory Networks for Crop Identification from Medium-Resolution Multispectral Satellite Images. *2017 IEEE Conference on Computer Vision and Pattern Recognition Workshops (CVPRW)*, 1496–1504. <https://doi.org/10/gkqvm2>
- Rußwurm, M., & Körner, M. (2018). Multi-Temporal Land Cover Classification with Sequential Recurrent Encoders. *ISPRS International Journal of Geo-Information*, 7(4), 129. <https://doi.org/10.3390/ijgi7040129>
- Safonova, A., Hamad, Y., Alekhina, A., & Kaplun, D. (2022). Detection of Norway Spruce Trees (*Picea abies*) Infested by Bark Beetle in UAV Images Using YOLOs Architectures. *IEEE Access*, 10, 10384–10392. <https://doi.org/10.1109/ACCESS.2022.3144433>
- Safonova, A., Tabik, S., Alcaraz-Segura, D., Rubtsov, A., Maglinets, Y., & Herrera, F. (2019). Detection of Fir Trees (*Abies sibirica*) Damaged by the Bark Beetle in Unmanned Aerial Vehicle Images with Deep Learning. *Remote Sensing*, 11(6), 643. <https://doi.org/10/gh3dnj>
- Sani-Mohammed, A., Yao, W., & Heurich, M. (2022). Instance segmentation of standing dead trees in dense forest from aerial imagery using deep learning. *ISPRS Open Journal of Photogrammetry and Remote Sensing*, 6, 100024. <https://doi.org/10.1016/j.ophoto.2022.100024>
- Santoro, M., & Cartus, O. (2023). ESA Biomass Climate Change Initiative (ESA Biomass CCI): Global datasets of forest above-ground biomass for the years 2010, 2017, 2018, 2019 and 2020. <https://doi.org/gr5z26>
- Santos, A. A. d., Marcato Junior, J., Araújo, M. S., Di Martini, D. R., Tetila, E. C., Siqueira, H. L., Aoki, C., Eltner, A., Matsubara, E. T., Pistori, H., Feitosa, R. Q., Liesenberg, V., & Gonçalves, W. N. (2019). Assessment of CNN-Based Methods for Individual Tree Detection on Images Captured by RGB Cameras Attached to UAVs. *Sensors*, 19(16), 3595. <https://doi.org/10/ghmdt4>
- Schall, P., Schulze, E.-D., Fischer, M., Ayasse, M., & Ammer, C. (2018). Relations between forest management, stand structure and productivity across differ-

- ent types of Central European forests. *Basic and Applied Ecology*, 32, 39–52. <https://doi.org/10/gfnbpj>
- Schiefer, F., Frey, J., & Kattenborn, T. (2022a). FORTRESS. <https://doi.org/https://doi.org/10.35097/538>
- Schiefer, F., Frick, A., Frey, J., Koch, B., Zielewska-Büttner, K., Junntila, S., Schmidtlein, S., & Kattenborn, T. (2022b). Predicting fractional cover of standing deadwood at landscape level based on long short-term memory networks and Sentinel time series. *Living Planet Symposium (2022), Bonn, Germany*, 23.05.2022 – 27.05.2022. <https://doi.org/10.5445/IR/1000167639>
- Schiefer, F., & Kattenborn, T. (2024). FORTRESSdead. <https://doi.org/10.35097/yARnkDzIcZIPSQhI>
- Schiefer, F., Kattenborn, T., Frick, A., Frey, J., Schall, P., Koch, B., & Schmidtlein, S. (2020). Mapping forest tree species in high resolution UAV-based RGB-imagery by means of convolutional neural networks. *ISPRS Journal of Photogrammetry and Remote Sensing*, 170, 205–215. <https://doi.org/10/ghrrhs>
- Schiefer, F., Kattenborn, T., Frick, A., Frey, J., Schall, P., Koch, B., & Schmidtlein, S. (2021). Mapping forest tree species in high resolution UAV-based RGB-imagery by means of convolutional neural networks. *European Geosciences Union General Assembly (EGU 2021), Online*, 19.04.2021 – 30.04.2021. <https://doi.org/10.5445/IR/1000167640>
- Schiefer, F., Schmidtlein, S., Frick, A., Frey, J., Klinke, R., Zielewska-Büttner, K., Junntila, S., Uhl, A., & Kattenborn, T. (2023a). UAV-based reference data for the prediction of fractional cover of standing deadwood from Sentinel time series. *ISPRS Open Journal of Photogrammetry and Remote Sensing*, 8, 100034. <https://doi.org/10.1016/j.ophoto.2023.100034>
- Schiefer, F., Schmidtlein, S., Frick, A., Frey, J., Klinke, R., Zielewska-Büttner, K., Uhl, A., Junntila, S., & Kattenborn, T. (2023b). Data package v2: UAV-based reference data for the prediction of fractional cover of standing deadwood from Sentinel time series. <https://doi.org/10.5445/IR/1000158765>
- Schiefer, F., Schmidtlein, S., Hartmann, H., Schnabel, F., & Kattenborn, T. (n.d.). Large-scale remote sensing reveals that tree mortality in Germany appears to be greater than previously expected. (*under review*) *Forestry: An International Journal of Forest Research*.
- Schiller, C., Schmidtlein, S., Boonman, C., Moreno-Martínez, A., & Kattenborn, T. (2021). Deep learning and citizen science enable automated plant trait predictions from photographs. *Scientific Reports*, 11(1), 16395. <https://doi.org/10.1038/s41598-021-95616-0>
- Schimanke, S., Ridal, M., Le Moigne, P., Berggren, L., Undén, P., Randriamampianina, R., Andrea, U., Bazile, E., Bertelsen, A., Brousseau, P., Dahlgren, P., Edvinsson, L., El Said, A., Glington, M., Hopsch, S., Isaksson, L., Mladek, R., Olsson, E., Verrelle, A., & Wang, Z. (2021). CERRA sub-daily regional

-
- reanalysis data for Europe on single levels from 1984 to present. <https://doi.org/https://doi.org/10.24381/cds.622a565a>
- Schnabel, F., Liu, X., Kunz, M., Barry, K. E., Bongers, F. J., Bruelheide, H., Fichtner, A., Härdtle, W., Li, S., Pfaff, C.-T., Schmid, B., Schwarz, J. A., Tang, Z., Yang, B., Bauhus, J., von Oheimb, G., Ma, K., & Wirth, C. (2021). Species richness stabilizes productivity via asynchrony and drought-tolerance diversity in a large-scale tree biodiversity experiment. *Science Advances*, 7(51), eabk1643. <https://doi.org/10.1126/sciadv.abk1643>
- Schnabel, F., Purruicker, S., Schmitt, L., Engelmann, R. A., Kahl, A., Richter, R., Seele-Dilbat, C., Skiadaresis, G., & Wirth, C. (2022). Cumulative growth and stress responses to the 2018–2019 drought in a European floodplain forest. *Global Change Biology*, 28(5), 1870–1883. <https://doi.org/10.1111/gcb.16028>
- Schuldt, B., Buras, A., Arend, M., Vitasse, Y., Beierkuhnlein, C., Damm, A., Gharun, M., Grams, T. E. E., Hauck, M., Hajek, P., Hartmann, H., Hiltbrunner, E., Hoch, G., Holloway-Phillips, M., Körner, C., Larysch, E., Lübbe, T., Nelson, D. B., Rammig, A., ... Kahmen, A. (2020). A first assessment of the impact of the extreme 2018 summer drought on Central European forests. *Basic and Applied Ecology*, 45, 86–103. <https://doi.org/10/gm7jmn>
- Schuster, M., & Paliwal, K. (1997). Bidirectional recurrent neural networks. *IEEE Transactions on Signal Processing*, 45(11), 2673–2681. <https://doi.org/10.1109/78.650093>
- Schwantes, A. M., Swenson, J. J., & Jackson, R. B. (2016). Quantifying drought-induced tree mortality in the open canopy woodlands of central Texas. *Remote Sensing of Environment*, 181, 54–64. <https://doi.org/10.1016/j.rse.2016.03.027>
- Schwarz, S., Werner, C., Fassnacht, F. E., & Ruehr, N. K. (2023). Forest canopy mortality during the 2018-2020 summer drought years in Central Europe: The application of a deep learning approach on aerial images across Luxembourg. *Forestry: An International Journal of Forest Research*, cpado49. <https://doi.org/10.1093/forestry/cpado49>
- Searle, E. B., Chen, H. Y. H., & Paquette, A. (2022). Higher tree diversity is linked to higher tree mortality. *Proceedings of the National Academy of Sciences*, 119(19), e2013171119. <https://doi.org/10.1073/pnas.2013171119>
- Senf, C., Buras, A., Zang, C. S., Rammig, A., & Seidl, R. (2020). Excess forest mortality is consistently linked to drought across Europe. *Nature Communications*, 11(1), 6200. <https://doi.org/10/gm7vhk>
- Senf, C., Pflugmacher, D., Zhiqiang, Y., Seibald, J., Knorn, J., Neumann, M., Hostert, P., & Seidl, R. (2018). Canopy mortality has doubled in Europe's temperate forests over the last three decades. *Nature Communications*, 9(1), 4978. <https://doi.org/10/gfq7h6>

- Senf, C., Sebold, J., & Seidl, R. (2021). Increasing canopy mortality affects the future demographic structure of Europe's forests. *One Earth*, 4(5), 749–755. <https://doi.org/10/gpg6ms>
- Senf, C., & Seidl, R. (2021). Mapping the forest disturbance regimes of Europe. *Nature Sustainability*, 4(1), 63–70. <https://doi.org/10/ghbmqz>
- Shen, J., Tao, C., Qi, J., & Wang, H. (2021). Semi-Supervised Convolutional Long Short-Term Memory Neural Networks for Time Series Land Cover Classification. *Remote Sensing*, 13(17), 3504. <https://doi.org/10.3390/rs13173504>
- Shi, X., Chen, Z., Wang, H., Yeung, D.-Y., Wong, W.-k., & Woo, W.-c. (2015). Convolutional LSTM Network: A Machine Learning Approach for Precipitation Nowcasting. *Advances in Neural Information Processing Systems*, 28. Retrieved April 10, 2024, from https://papers.nips.cc/paper_files/paper/2015/hash/07563a3fe3bbe7e3ba84431ad9do55af-Abstract.html
- Skrzecz, I., Ślusarski, S., & Tkaczyk, M. (2020). Integration of science and practice for *Dendrolimus pini* (L.) management – A review with special reference to Central Europe. *Forest Ecology and Management*, 455, 117697. <https://doi.org/10.1016/j.foreco.2019.117697>
- Socha, J., Hawryło, P., Tyminska-Czabańska, L., Reineking, B., Lindner, M., Netzel, P., Grabska-Szwagrzyk, E., Vallejos, R., & Reyer, C. P. O. (2023). Higher site productivity and stand age enhance forest susceptibility to drought-induced mortality. *Agricultural and Forest Meteorology*, 341, 109680. <https://doi.org/10.1016/j.agrformet.2023.109680>
- Soltani, S., Feilhauer, H., Duker, R., & Kattenborn, T. (2022). Transfer learning from citizen science photographs enables plant species identification in UAV imagery. *ISPRS Open Journal of Photogrammetry and Remote Sensing*, 5, 100016. <https://doi.org/10.1016/j.ophoto.2022.100016>
- Sothe, C., Almeida, C. M. D., Schimalski, M. B., Rosa, L. E. C. L., Castro, J. D. B., Feitosa, R. Q., Dalponte, M., Lima, C. L., Liesenberg, V., Miyoshi, G. T., & Tommaselli, A. M. G. (2020). Comparative performance of convolutional neural network, weighted and conventional support vector machine and random forest for classifying tree species using hyperspectral and photogrammetric data. *GIScience & Remote Sensing*, 57(3), 369–394. <https://doi.org/10/gh3dps>
- Stephenson, N. L., & Das, A. J. (2020). Height-related changes in forest composition explain increasing tree mortality with height during an extreme drought. *Nature Communications*, 11(1), 3402. <https://doi.org/10.1038/s41467-020-17213-5>
- Stephenson, N. L., Das, A. J., Amperssee, N. J., Bulaon, B. M., & Yee, J. L. (2019). Which trees die during drought? The key role of insect host-tree selection. *Journal of Ecology*, 107(5), 2383–2401. <https://doi.org/10.1111/1365-2745.13176>

-
- Storch, I., Penner, J., Asbeck, T., Basile, M., Bauhus, J., Braunisch, V., Dormann, C. F., Frey, J., Gärtner, S., Hanewinkel, M., Koch, B., Klein, A.-M., Kuss, T., Pregernig, M., Pyttel, P., Reif, A., Scherer-Lorenzen, M., Segelbacher, G., Schraml, U., ... Yousefpour, R. (2020). Evaluating the effectiveness of retention forestry to enhance biodiversity in production forests of Central Europe using an interdisciplinary, multi-scale approach. *Ecology and Evolution*, *10*(3), 1489–1509. <https://doi.org/10/gh3c66>
- Stovall, A. E. L., Shugart, H., & Yang, X. (2019). Tree height explains mortality risk during an intense drought. *Nature Communications*, *10*(1), 4385. <https://doi.org/10.1038/s41467-019-12380-6>
- Stovall, A. E. L., Shugart, H. H., & Yang, X. (2020). Reply to “Height-related changes in forest composition explain increasing tree mortality with height during an extreme drought”. *Nature Communications*, *11*. <https://doi.org/10.1038/s41467-020-17214-4>
- Sylvain, J.-D., Drolet, G., & Brown, N. (2019). Mapping dead forest cover using a deep convolutional neural network and digital aerial photography. *ISPRS Journal of Photogrammetry and Remote Sensing*, *156*, 14–26. <https://doi.org/10.1016/j.isprsjprs.2019.07.010>
- Thonfeld, F., Gessner, U., Holzwarth, S., Kriese, J., da Ponte, E., Huth, J., & Kuenzer, C. (2022). A First Assessment of Canopy Cover Loss in Germany’s Forests after the 2018–2020 Drought Years. *Remote Sensing*, *14*(3), 562. <https://doi.org/10.3390/rs14030562>
- Torresan, C., Berton, A., Carotenuto, F., Gennaro, S. F. D., Gioli, B., Matese, A., Miglietta, F., Vagnoli, C., Zaldei, A., & Wallace, L. (2017). Forestry applications of UAVs in Europe: a review. *International Journal of Remote Sensing*, *38*(8), 2427–2447. <https://doi.org/10/gh3c6t>
- Trier, Ø. D., Salberg, A.-B., Kermit, M., Rudjord, Ø., Gobakken, T., Næsset, E., & Aarsten, D. (2018). Tree species classification in Norway from airborne hyperspectral and airborne laser scanning data. *European Journal of Remote Sensing*, *51*(1), 336–351. <https://doi.org/10/gh3dkp>
- Trumbore, S., Brando, P., & Hartmann, H. (2015). Forest health and global change. *Science*, *349*(6250), 814–818. <https://doi.org/10.1126/science.aac6759>
- Valbuena, R., Mauro, F., Suárez, R. R.-S., & Manzanera, J. A. (2010). Accuracy and precision of GPS receivers under forest canopies in a mountainous environment. *Spanish journal of agricultural research*, *8*(4), 1047–1057. <https://doi.org/10/gh3dk4>
- Vanoni, M., Bugmann, H., Nötzli, M., & Bigler, C. (2016). Drought and frost contribute to abrupt growth decreases before tree mortality in nine temperate tree species. *Forest Ecology and Management*, *382*, 51–63. <https://doi.org/10.1016/j.foreco.2016.10.001>
- Vautard, R., van Oldenborgh, G. J., Bonnet, R., Li, S., Robin, Y., Kew, S., Philip, S., Soubeyroux, J.-M., Dubuisson, B., Viovy, N., Reichstein, M., Otto, F., &

- Garcia de Cortazar-Atauri, I. (2023). Human influence on growing-period frosts like in early April 2021 in central France. *Natural Hazards and Earth System Sciences*, 23(3), 1045–1058. <https://doi.org/10.5194/nhess-23-1045-2023>
- Verbesselt, J., Hyndman, R., Newnham, G., & Culvenor, D. (2010). Detecting trend and seasonal changes in satellite image time series. *Remote Sensing of Environment*, 114(1), 106–115. <https://doi.org/10.1016/j.rse.2009.08.014>
- Vittoz, P., & Guisan, A. (2007). How reliable is the monitoring of permanent vegetation plots? A test with multiple observers. *Journal of Vegetation Science*, 18(3), 413–422. <https://doi.org/10.1111/j.1654-1103.2007.tb02553.x>
- Wagner, F. H., Sanchez, A., Aidar, M. P. M., Rochelle, A. L. C., Tarabalka, Y., Fonseca, M. G., Phillips, O. L., Gloor, E., & Aragão, L. E. O. C. (2020). Mapping Atlantic rainforest degradation and regeneration history with indicator species using convolutional network. *PLOS ONE*, 15(2), e0229448. <https://doi.org/10/gh3dng>
- Wagner, F. H., Sanchez, A., Tarabalka, Y., Lotte, R. G., Ferreira, M. P., Aidar, M. P. M., Gloor, E., Phillips, O. L., & Aragão, L. E. O. C. (2019). Using the U-net convolutional network to map forest types and disturbance in the Atlantic rainforest with very high resolution images. *Remote Sensing in Ecology and Conservation*, 5(4), 360–375. <https://doi.org/10/gh3dqx>
- Wäldchen, J., & Mäder, P. (2018). Machine learning for image based species identification. *Methods in Ecology and Evolution*, 9(11), 2216–2225. <https://doi.org/10.1111/2041-210X.13075>
- Wallace, L., Bellman, C., Hally, B., Hernandez, J., Jones, S., & Hillman, S. (2019). Assessing the Ability of Image Based Point Clouds Captured from a UAV to Measure the Terrain in the Presence of Canopy Cover. *Forests*, 10(3), 284. <https://doi.org/10/gh3c62>
- Wang, P., Bayram, B., & Sertel, E. (2022). A comprehensive review on deep learning based remote sensing image super-resolution methods. *Earth-Science Reviews*, 232, 104110. <https://doi.org/10.1016/j.earscirev.2022.104110>
- Wang, W.-Y., Li, H.-C., Deng, Y.-J., Shao, L.-Y., Lu, X.-Q., & Du, Q. (2021). Generative Adversarial Capsule Network With ConvLSTM for Hyperspectral Image Classification. *IEEE Geoscience and Remote Sensing Letters*, 18(3), 523–527. <https://doi.org/10.1109/LGRS.2020.2976482>
- Weinstein, B. G., Marconi, S., Bohlman, S. A., Zare, A., & White, E. (2019). Individual Tree-Crown Detection in RGB Imagery Using Semi-Supervised Deep Learning Neural Networks. *Remote Sensing*, 11(11), 1309. <https://doi.org/10/ghmdr5>
- Weinstein, B. G., Marconi, S., Bohlman, S. A., Zare, A., & White, E. P. (2020). Cross-site learning in deep learning RGB tree crown detection. *Ecological Informatics*, 56, 101061. <https://doi.org/10/gh3dnz>

-
- Weslien, J., Öhrn, P., Rosenberg, O., & Schroeder, M. (2024). Effects of sanitation logging in winter on the Eurasian spruce bark beetle and predatory long-legged flies. *Forest Ecology and Management*, 554, 121665. <https://doi.org/10.1016/j.foreco.2023.121665>
- White, J. C., Wulder, M. A., Hermosilla, T., Coops, N. C., & Hobart, G. W. (2017). A nationwide annual characterization of 25 years of forest disturbance and recovery for Canada using Landsat time series. *Remote Sensing of Environment*, 194, 303–321. <https://doi.org/10/gh7xmx>
- Wilkinson, M. D., Dumontier, M., Aalbersberg, I. J., Appleton, G., Axton, M., Baak, A., Blomberg, N., Boiten, J.-W., da Silva Santos, L. B., Bourne, P. E., Bouwman, J., Brookes, A. J., Clark, T., Crosas, M., Dillo, I., Dumon, O., Edmunds, S., Evelo, C. T., Finkers, R., . . . Mons, B. (2016). The FAIR Guiding Principles for scientific data management and stewardship. *Scientific Data*, 3(1), 160018. <https://doi.org/10.1038/sdata.2016.18>
- Wolf, S., Mahecha, M. D., Sabatini, F. M., Wirth, C., Bruelheide, H., Kattge, J., Moreno Martínez, Á., Mora, K., & Kattenborn, T. (2022). Citizen science plant observations encode global trait patterns. *Nature Ecology & Evolution*, 6(12), 1850–1859. <https://doi.org/10.1038/s41559-022-01904-x>
- Wright, M. N., & Ziegler, A. (2017). ranger: A Fast Implementation of Random Forests for High Dimensional Data in C++ and R. *Journal of Statistical Software*, 77, 1–17. <https://doi.org/10.18637/jss.v077.i01>
- Xi, Y., Ren, C., Tian, Q., Ren, Y., Dong, X., & Zhang, Z. (2021). Exploitation of Time Series Sentinel-2 Data and Different Machine Learning Algorithms for Detailed Tree Species Classification. *IEEE Journal of Selected Topics in Applied Earth Observations and Remote Sensing*, 14, 7589–7603. <https://doi.org/10.1109/JSTARS.2021.3098817>
- Xue, J., & Su, B. (2017). Significant Remote Sensing Vegetation Indices: A Review of Developments and Applications. *Journal of Sensors*, 2017, 1–17. <https://doi.org/10.1155/2017/1353691>
- Younis, S., Weiland, C., Hoehndorf, R., Dressler, S., Hickler, T., Seeger, B., & Schmidt, M. (2018). Taxon and trait recognition from digitized herbarium specimens using deep convolutional neural networks. *Botany Letters*, 165(3), 377–383. <https://doi.org/10.1080/23818107.2018.1446357>
- Yuan, Y., & Lin, L. (2021). Self-Supervised Pretraining of Transformers for Satellite Image Time Series Classification. *IEEE Journal of Selected Topics in Applied Earth Observations and Remote Sensing*, 14, 474–487. <https://doi.org/10.1109/JSTARS.2020.3036602>
- Zhang, L., Zhang, L., & Du, B. (2016). Deep Learning for Remote Sensing Data: A Technical Tutorial on the State of the Art. *IEEE Geoscience and Remote Sensing Magazine*, 4(2), 22–40. <https://doi.org/10/gfpgjn>

- Zhang, Z., & Zhu, L. (2023). A Review on Unmanned Aerial Vehicle Remote Sensing: Platforms, Sensors, Data Processing Methods, and Applications. *Drones*, 7(6), 398. <https://doi.org/10.3390/drones7060398>
- Zhong, L., Hu, L., & Zhou, H. (2019). Deep learning based multi-temporal crop classification. *Remote Sensing of Environment*, 221, 430–443. <https://doi.org/10.1016/j.rse.2018.11.032>
- Zhu, X. X., Tuia, D., Mou, L., Xia, G.-S., Zhang, L., Xu, F., & Fraundorfer, F. (2017). Deep Learning in Remote Sensing: A Comprehensive Review and List of Resources. *IEEE Geoscience and Remote Sensing Magazine*, 5(4), 8–36. <https://doi.org/10.1109/MGRS.2017.2762307>
- Zielewska-Büttner, K., Adler, P., Kolbe, S., Beck, R., Ganter, L. M., Koch, B., & Braunisch, V. (2020). Detection of Standing Deadwood from Aerial Imagery Products: Two Methods for Addressing the Bare Ground Misclassification Issue. *Forests*, 11(8), 801. <https://doi.org/10/gmncnf>
- Zink, M., Samaniego, L., Kumar, R., Thober, S., Mai, J., Schäfer, D., & Marx, A. (2016). The German drought monitor. *Environmental Research Letters*, 11(7), 074002. <https://doi.org/10.1088/1748-9326/11/7/074002>
- Zscheischler, J., Martius, O., Westra, S., Bevacqua, E., Raymond, C., Horton, R. M., van den Hurk, B., AghaKouchak, A., Jézéquel, A., Mahecha, M. D., Maraun, D., Ramos, A. M., Ridder, N. N., Thiery, W., & Vignotto, E. (2020). A typology of compound weather and climate events. *Nature Reviews Earth & Environment*, 1(7), 333–347. <https://doi.org/10.1038/s43017-020-0060-z>
- Zscheischler, J., Westra, S., van den Hurk, B. J. J. M., Seneviratne, S. I., Ward, P. J., Pitman, A., AghaKouchak, A., Bresch, D. N., Leonard, M., Wahl, T., & Zhang, X. (2018). Future climate risk from compound events. *Nature Climate Change*, 8(6), 469–477. <https://doi.org/10.1038/s41558-018-0156-3>